EFFECT OF GRAIN SIZE ON OPTICAL TRANSMITTANCE OF BIREFRINGENT POLYCRYSTALLINE CERAMICS

by

Tzu-Chien Wen

A dissertation submitted to the faculty of
The University of Utah
in partial fulfillment of the requirements for the degree of

Doctor of Philosophy

Department of Materials Science and Engineering

The University of Utah

December 2016

The University of Utah Graduate School

STATEMENT OF DISSERTATION APPROVAL

The dissertation of **Tzu-Chien Wen**

has been approved by the following supervisory committee members:

Dinesh K. Shetty	, Chair	**4/15/2016** Date Approved
Agnes Ostafin	, Member	**4/15/2016** Date Approved
Michael Scarpulla	, Member	**4/18/2016** Date Approved
Taylor Sparks	, Member	**4/15/2016** Date Approved
Ling Zang	, Member	**4/18/2016** Date Approved

and by **Feng Liu** , Chair/Dean of

the Department/College/School of **Materials Science and Engineering**

and by David B. Kieda, Dean of The Graduate School.

ABSTRACT

Polycrystalline ceramics are increasingly used for fabricating windows and domes for the mid infra-red regime (3-5 μm) due to their superior durability as compared to glass and the lower cost of their fabrication and finishing relative to single crystals without significant compromise in optical properties. Due to the noncubic structure, MgF_2 and Al_2O_3 are birefringent ceramics. Birefringence causes scatter of light at the grain boundaries and diminishes in-line transmittance and optical performance. This dissertation presents experimental results and analyses of the grain-size and wavelength dependence of the in-line transmittance of polycrystalline MgF_2 and Al_2O_3.

Chapter 2 presents experimental results and analyses of light transmission in polycrystalline MgF_2 as a function of the mean grain size at different wavelengths. The scattering coefficient of polycrystalline MgF_2 increased linearly with the mean grain size and inversely with the square of the wavelength of light. These trends are consistent with theoretical models based on both a limiting form of the Raleigh-Gans-Debye theory of particle scattering and light retardation theories that take refractive-index variations along the light path.

Chapter 3 investigates the applicability of particle light scattering theories to light attenuation in birefringent polycrystalline ceramics by measuring light transmittance in a model two-phase system. The system consisted of microspheres of silica dispersed in a solution of glycerol in water. It was found that RGD theory showed the systematic deviation for higher particle volume fraction ($\phi > 0.2$) and larger particle size ($d_p > 1$ μm).

This result suggested that light scattering models based on single particle scattering are unlikely to provide viable physical explanation for the effect of grain size on light transmittance in birefringent polycrystalline ceramics due to the high volume fraction in dense polycrystalline ceramics.

Chapter 4 analyses light transmission properties of polycrystalline Al_2O_3 using theories of wave propagation in random media. Fully dense polycrystalline Al_2O_3 was fabricated using a pressure filtration method. By obtaining the $\overline{\Delta n^2}$ measured from EBSD, the wave retardation theories of Raman and Viswanathan and Kahan *et al.* provided upper and lower bounds for the theoretical predictions of light transmittance as a function of mean intercept length.

TABLE OF CONTENTS

LIST OF FIGURES

LIST OF TABLES

LIST OF NOMENCLATURE

A:	Absorptance
d_p:	Particle size
d_{pore}:	Pore diameter
$\overline{d_N}$:	Number fraction average diameter
$\overline{d_\phi}$:	Volume fraction average diameter
E:	Young's modulus
$F(\theta)$:	Cumulative fraction of grains
$f(\theta)$:	Density distribution of the orientations
$\bar{G}$:	Number average grain size
$\overline{G_\phi}$:	Volume fraction weighted average grain size
I_0:	Intensity of the incident light
I:	Intensity of the transmitted light
I/I_0:	In-line transmittance
K:	Scattering efficiency
k:	Thermal conductivity
L:	Distance from the specimen surface to the aperture in front of the detector
$\bar{L}$:	Mean intercept length
l:	Radius of the aperture in front of the detector
N:	Number of particles per unit volume
n_e:	Refractive index in ordinary direction:
n_o:	Refractive index in extraordinary direction
$\bar{n}$:	Mean refractive index
$\overline{\Delta n^2}$:	Mean square deviation of refractive index
P_i:	Power measured by a detector of the incident beam
P_s:	Power measured by a detector at a scattering angle

P_x: Number of pixels in each row

R: Single surface reflectance

R': Thermal-shock resistance

R_T: Total surface reflectance

R_x: Number of rows scanned in the *x* direction

S_B: Backward scatter

S_F: Forward scatter

S_T: Total Scatter

T: Transmittance

t: Thickness (path length)

x: Normalized particle size

α: Material-characteristic parameter

α_L: Coefficient of linear thermal expansion

Υ: Scattering coefficient

γ_{pore}: Scattering coefficient of pore scattering

Δ: Edge length

δ: Scan step distance

ε: Emissivity

θ: Grain orientation angle

$\bar{\theta}$: Mean grain orientation angle

θ_s: Scattering angle

λ_0: Wavelength of light in vacuum

σ_f: Bending Strength

ν: Poisson's ratio

ϕ: Volume fraction of particles or grains

ϕ_{pore}: Porosity

Ω_S: Solid angle subtended by the detector

ACKNOWLEDGEMENTS

This dissertation would not be possible without the help and support of many people. First, I would like to express my sincere appreciation to Prof. Dinesh K. Shetty for valuable advice and guidance, constant support, patience and encouragement. I would like to thank my committee members Dr. Agnes Ostafin, Dr. Mike Scarpulla, Dr. Taylor Sparks and Dr. Ling Zang for their time and effort. I would like to thank Dr. Stuart I. Wright and Mr. Ron Witt of EDAX, Inc., for their assistance in collecting the EBSD data on MgF_2 and Al_2O_3 specimens. I would like to thank Dr. Whai-Yuh Lin and Dr. Chen-Shen Chang for proving the magnesium fluoride specimens. I would like to thank Dr. Daniel C. Harris for his support for this work. I have been lucky to work with Dr. Niladri Dasgupta, Dr. Joon-Ho Koh and Mr. Erinn Sorge on other projects.

Lastly, I would like to thank my wife (Joo), my lovely children (Rosa, Issa and Bellsa) and our families in Taiwan (Chien-Hsiung Wen, Yuen-Ming Lin and Tzu-Yu Wen) and Korea, for their constant support and encouragement. A special acknowledgement to my friend Dr. Issue Ho for his support.

CHAPTER 1

BIREFRINGENCE AND LIGHT TRANSMISSION IN POLYCRYSTALLINE CERAMICS – GENERAL BACKGROUND

1.1 Introduction

Transparent materials for windows and domes are classified in three categories: (1) glasses, (2) single crystals, and (3) polycrystalline materials [1, 2]. Glasses and single-crystals offer good optical properties. However, poor mechanical properties and lack of durability limit the use of glass in high-performance windows and domes of high-speed missiles. Single crystals are expensive to process and finish to aerodynamic shapes. Therefore, there has been an increasing focus on developing transparent polycrystalline materials with improved durability without sacrificing optical properties and performance. Specifically, material properties required for mid infrared (3~5 micron) windows and domes include high transmittance, low emissivity, and high durability. Durability is enhanced by increasing hardness, fracture strength, fracture toughness, and thermal conductivity, while decreasing thermal expansion [1-3].

The intensity of light transmitted through a window of thickness t, that partially scatters light in the bulk and reflects at the two surfaces is given by the following equation[1]

[1] See Appendix A for derivations of this equation.

[2]:

$$I(t) = I_0\left[\frac{(1-R)^2 e^{-\gamma t}}{1-R^2 e^{-2\gamma t}}\right] \tag{1.1}$$

where I_0 is the intensity of the incident light, R is the single-surface reflectance, and γ is the scattering coefficient that accounts for the light scattered and/or absorbed in the material.

Smooth surfaces, low surface reflection, and low scattering are the keys to obtaining high transmittance. In the case where the surface is smooth and the surrounding medium is air, the single surface reflection is defined as [2]

$$R = \left(\frac{1-n}{1+n}\right)^2 \tag{1.2}$$

where n is the refractive index of the window material. The total reflection, R_T, describes the reflection loss at the two sample surfaces and includes contributions from multiple internal reflections. The total reflection can be expressed as

$$R_T = \frac{2R}{1+R} \tag{1.3}$$

It should be noted that both R and R_T decrease as n approaches the value 1. In the case where there is no absorption or scatter, the transmittance is given by [2]

$$T = 1 - R_T = \frac{2n}{n^2+1} \tag{1.4}$$

The scattering coefficient,γ, depends on different light scattering mechanisms. Optical transmittance of polycrystalline ceramics may be compromised by a number of light scattering inhomogeneities, for example, surface roughness, second-phase inclusions, pores and grain boundaries as shown in Figure 1.1 [4]. Clearly, light scattering at rough surface can be minimized by fine polishing. Second-phase inclusions and pores can be

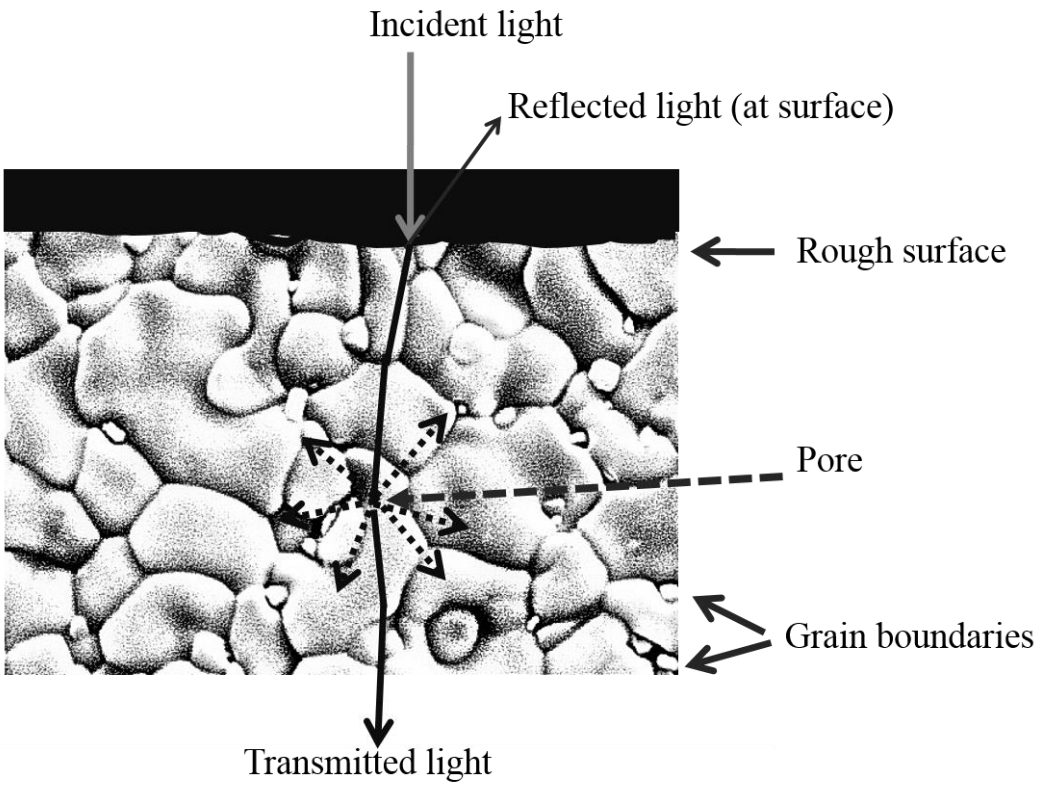

Figure 1.1 An illustration of light scattering mechanisms in polycrystalline materials [4].

reduced by using high-purity powders and advanced processing and densification methods. Therefore, grain boundaries remain the most significant source for light scattering in polycrystalline ceramics. The formulation of the scattering coefficient for grain-boundary scattering using both particle light scattering theory and theories of light propagation in random media will be discussed in a later section.

The emissivity of a material is the radiation emitted by the material relative to a blackbody. The emissivity is a number ranging between 0 and 1, and it varies with wavelength and temperature. A blackbody material with zero reflection is a perfect absorber, which has an emissivity of 1. For a window material, the emissivity normal to the surface is given by [2]

$$\varepsilon = \frac{radiant\ power\ emitted\ by\ material}{radiant\ power\ emitted\ by\ blackbody} \tag{1.5}$$

The emissivity of hot-pressed MgF_2 was reported as 0.022 averaged over the wavelength range 3 to 5 μm at a temperature of 542°C [2]. The emissivity of Al_2O_3 can vary depending on the method of manufacture as well as the composition. For sapphire, emissivity is 0.1 at a wavelength of 4.5 μm and temperature of 427°C [5].

1.1.1 Current Materials for IR Windows and Domes

Hot-pressed polycrystalline magnesium fluoride (MgF_2) and sapphire (single crystal alumina) are widely used in current IR windows and domes in the mid infra-red regime. Polycrystalline alumina (Al_2O_3) has been used in optical applications since the 1960s when Coble [6] developed the first translucent alumina for high pressure sodium vapor lamp envelope named Lucalox®. Lucalox® is a coarse-grained Al_2O_3 and it cannot be used for dome applications due to its low in-line transmittance. On the other hand, fine-

grained polycrystalline Al_2O_3 is a new candidate material for optical windows and domes. Fine-grained polycrystalline Al_2O_3 has a great potential for providing optical performance comparable to sapphire, yet offering low cost of fabrication. Figure 1.2 compares optical transmittance of polycrystalline MgF_2, sapphire (0°, *c*-axis parallel to the direction of light propagation) and polycrystalline Al_2O_3 in the wavelength range from 0.2 to 10 μm for 1 mm thick plates. It is seen that polycrystalline MgF_2 offers high transmittance and long IR cut-off wavelength. The transmittance spectrum of polycrystalline MgF_2 shows several extrinsic absorption bands from various adsorbed species on the surface. Sapphire and polycrystalline Al_2O_3 have similar cut-off wavelength around 5 μm, and the highest transmittance is ~8% lower than that of polycrystalline MgF_2 due to the higher refractive index. In the short-infrared and visible regime, in-line transmittance decreases for polycrystalline MgF_2 and Al_2O_3 because of birefringence of these materials.

Table 1.1 [7] lists some physical (Young's modulus, *E*, and Poisson's ratio, ν), mechanical (flexural strength, σ_f, and Vickers hardness, *HV*) and thermal (thermal conductivity, *k*, and thermal expansion coefficient, α_L) properties of polycrystalline MgF_2 (grain size around 0.55 μm), sapphire (0°) and polycrystalline Al_2O_3 (grain size around 0.56 μm). Polycrystalline MgF_2 has low Young's modulus, flexural strength, Vickers hardness, and thermal conductivity and high thermal expansion coefficient. On the other hand, sapphire and polycrystalline Al_2O_3 have high Young's modulus, flexural strength, Vickers hardness, and thermal conductivity and low thermal expansion coefficient. Thermal-shock resistance and erosion resistance are two important parameters that assess the durability of optical windows and domes. Thermal-shock resistance, R', is defined by the following equation [2]:

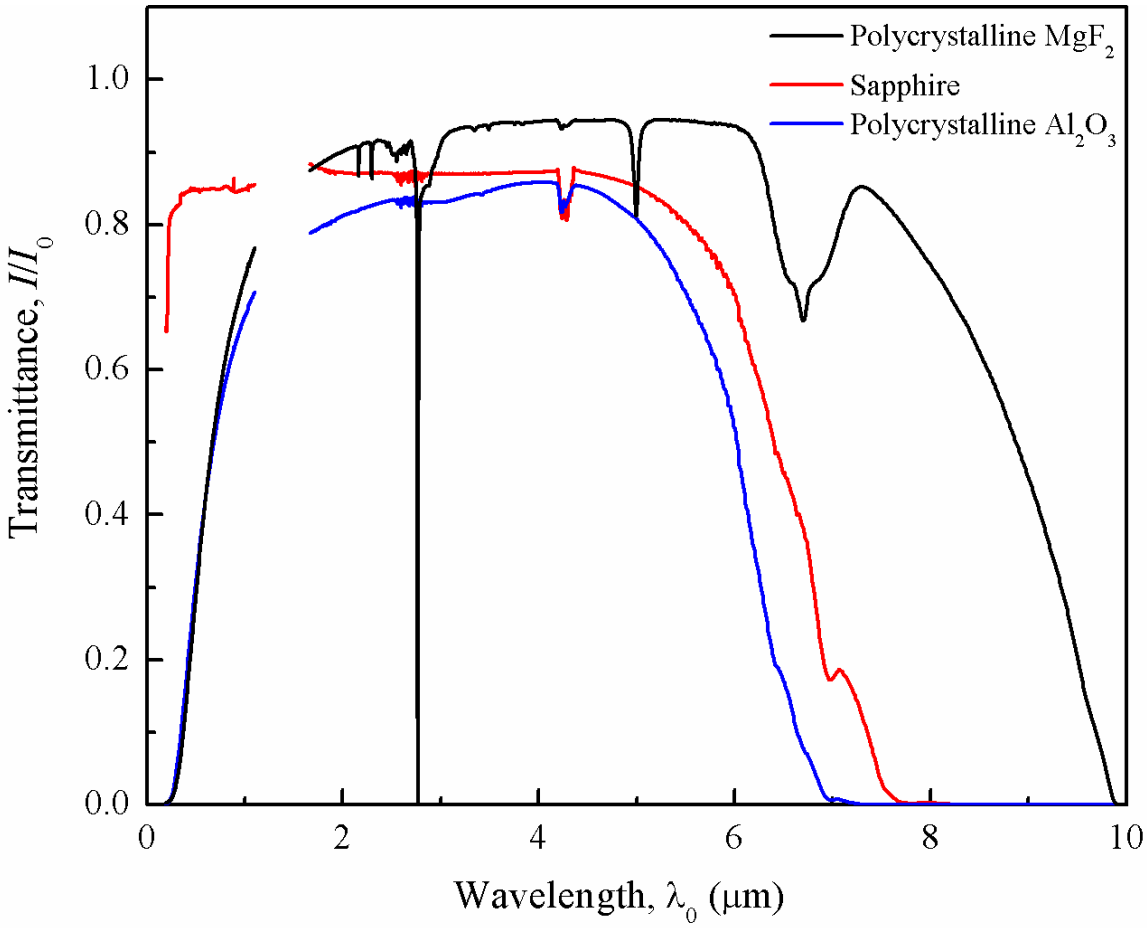

Figure 1.2 Optical transmittance of polycrystalline MgF_2, sapphire and polycrystalline Al_2O_3 and in the wavelength range from 0.2 to 10 microns.

Table 1.1 Mechanical and thermal properties of polycrystalline MgF_2, sapphire and polycrystalline Al_2O_3 [7]. (a: three-point flexural strength, and b: ring-on-ring bend test)

Material	Young's Modulus, E (GPa)	Poisson's Ratio, ν	Flexural Strength, σ_f (MPa)	Vickers Hardness, HV (GPa)	Thermal Conductivity, k (W/mK)	Thermal Expansion Coefficient, α_L (10^{-6}/K)	Thermal- Shock Resistance, R' (kW/m)
Polycrystalline MgF_2	142±10	0.27±0.02	157[a]	6.5	9.4	11.1	0.60
Sapphire	460±10	0.18±0.02	687[a]	20	38.5	5.2	8.20
Polycrystalline Al_2O_3	397±10	0.26±0.02	804[b]	23	15.1	6.7	3.20

$$R' = \frac{\sigma_f(1-\nu)k}{\alpha_L E} \tag{1.6}$$

Table 1.1 shows that polycrystalline MgF_2 has low thermal-shock resistance due to its low flexural strength, low thermal conductivity and high thermal expansion coefficient. Optical windows/domes for external use are eroded by high speed impact with rain drops and sand particles. Figure 1.3 [1] shows the damage threshold velocity for 300 impacts on the same spot by a laboratory waterjet with a 0.8 mm diameter nozzle. The damage threshold velocity for a material is the waterjet velocity below which no damage is observed after 300 impacts and above which damage is observed [1]. Figure 1.3 shows that natural diamond exhibits the highest threshold velocity, followed by sapphire, spinel and MgF_2.

1.2 Crystal Physics and Optics

In the general case, a crystal can have three principal refractive indices, n_x, n_y and n_z. The crystal is optically isotropic when all of the three principal indices are equal. In the case where two of the principal indices are equal, the crystal is said to be uniaxial, or birefringent. When all the three principal indices are different, the crystal is said to be biaxial (trirefringent). All cubic crystals are isotropic in their refractive index. Tetragonal, hexagonal, and trigonal crystals have uniaxial symmetry, while orthorhombic, monoclinic and triclinic structures have biaxial symmetry [8].

MgF_2 and Al_2O_3 are birefringent uniaxial crystals. In uniaxial crystals, *c*-axis is defined as the optical axis or ordinary direction, and any axis perpendicular to the c-axis is called the extraordinary direction [2]. The corresponding refractive indices are designated n_o and n_e, respectively. The birefringence of a uniaxial crystal is defined as $\Delta n_{max} =$

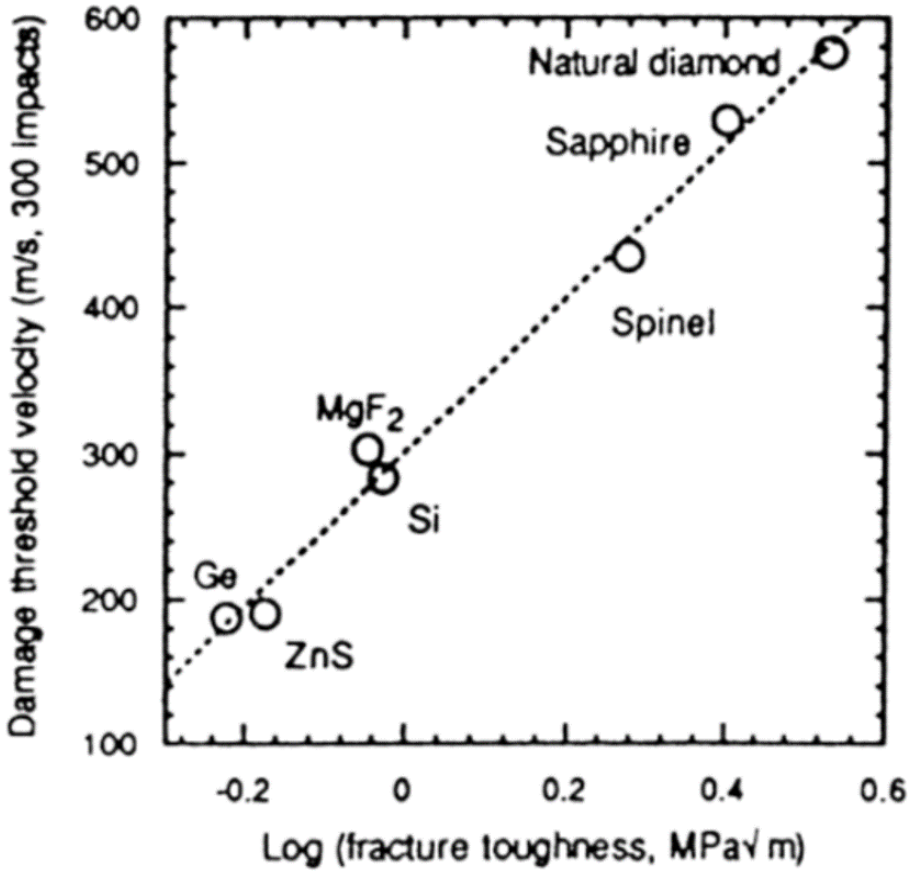

Figure 1.3 Waterjet damage threshold velocity is correlated with logarithm of fracture toughness of optical materials [1].

$(n_e - n_o)$. When $n_e > n_o$, as in the case of MgF_2, it is called a positive uniaxial crystal,and a negative uniaxial crystal has $n_e < n_o$, as in the case of Al_2O_3 [9].

MgF_2 has a tetragonal crystal structure [10]. The unit cell contains two formula units, and the lattice parameters are a = 0.4623 nm and c = 0.3052 nm at 300 K [10]. The theoretical density is 3.177g/cm^3. Dodge [11] measured refractive indices for single crystal MgF_2 in the ordinary and the extra-ordinary directions as functions of wavelength and fitted the data to the following Sellmeier dispersion equations in the wavelength range from 0.2 μm to 7.04 μm:

$$n_o^2 = 1 + \frac{0.478755108\lambda^2}{\lambda^2 - 0.04338408^2} + \frac{0.39875031\lambda^2}{\lambda^2 - 0.09461442^2} + \frac{2.3120353\lambda^2}{\lambda^2 - 23.793604^2} \tag{1.7}$$

and

$$n_e^2 = 1 + \frac{0.41344023\lambda^2}{\lambda^2 - 0.03684262^2} + \frac{0.50497499\lambda^2}{\lambda^2 - 0.09076162^2} + \frac{2.4904862\lambda^2}{\lambda^2 - 12.771995^2} \tag{1.8}$$

Aluminum oxide crystallizes in the corundum (α-Al_2O_3) rhombohedral structure. The lattice parameters of the unit cell are a = 0.4759 nm and c = 1.2991 nm at 295 K, and the ratio c/a = 2.7298 far exceeds that of a crystal with ideal hexagonal packing ($\sqrt{8/3} \sim 1.663$) [12]. The theoretical density is 3.987 g/cm^3. The refractive indices of sapphire were reported by Malitson and Dodge [13, 14] in the wavelength range 0.2 to 5.5 μm as follows:

$$n_o^2 = 1 + \frac{1.4313493\lambda^2}{\lambda^2 - 0.0726631^2} + \frac{0.65054713\lambda^2}{\lambda^2 - 0.1193242^2} + \frac{5.3414021\lambda^2}{\lambda^2 - 18.028251^2} \tag{1.9}$$

and

$$n_e^2 = 1 + \frac{1.5039759\lambda^2}{\lambda^2 - 0.0740288^2} + \frac{0.55069141\lambda^2}{\lambda^2 - 0.1216529^2} + \frac{6.5927379\lambda^2}{\lambda^2 - 20.072248^2} \tag{1.10}$$

Table 1.2 lists the refractive indices of MgF_2 and Al_2O_3 at several wavelengths, and the isotropic refractive index of $MgAl_2O_4$ at 0.645 μm. It is noted that MgF_2 has the lower refractive index but higher birefringence compared to Al_2O_3.

The average refractive index for a polycrystalline material is defined as [15]:

$$\bar{n} = \int_0^{\pi/2} n(\theta) f(\theta) d\theta \tag{1.11}$$

where θ is the grain orientation angle relative to the *c*-axis, *f*(θ) is the density distribution of the orientations ($f(\theta) = \sin\theta$, for isotropic randomly oriented grains[2]) and *n*(θ) is defined as [15]:

$$n(\theta) = \frac{n_o n_e}{\sqrt{(n_e^2 cos^2\theta + n_o^2 sin^2\theta)}} \tag{1.12}$$

Therefore, the refractive index in any crystal direction or for a polycrystal with any distribution of grain orientations can be calculated for a particular wavelength using Sellmeier equations, such as Eqs. (1.7) and (1.8) or (1.9) and (1.10).

[2] See Appendix B for derivations of this equation.

Table 1.2 The refractive indices in the ordinary (n_o) and the extraordinary (n_e) directions for Al_2O_3 and MgF_2 at different wavelengths, and the isotropic refractive index of $MgAl_2O_4$.

Materials	λ_0 (μm)	n_o	n_e	$\lvert\Delta n_{max}\rvert$
MgF_2	0.633	1.3770	1.3888	0.0118
MgF_2	1.064	1.3732	1.3848	0.0116
MgF_2	3.39	1.3560	1.3664	0.0104
Al_2O_3	0.633	1.7659	1.7579	0.0080
Al_2O_3	0.645	1.7653	1.7573	0.0080
Al_2O_3	1.064	1.7545	1.7466	0.0079
Al_2O_3	3.39	1.6993	1.6919	0.0074
$MgAl_2O_4$	0.640	1.7134	1.7134	0

1.3 Effect of Grain Size on Light Transmittance in Birefringent Polycrystalline Ceramics

Several research groups have reported on the effects of grain size on the optical transmittance of polycrystalline ceramics. Lin *et al.* [16] hot-pressed MgF_2 powder at temperatures ranging from 565 to 710°C and a pressure of 241 MPa for 50 minutes. Mean grain size ranged from 0.2 to 1.5 μm. Optical transmittance, measured at wavelengths from 0.7 to 5.5 μm, decreased with increasing mean grain size. Chang *et al.* [17] hot-pressed MgF_2 powder in air at temperatures ranging from 510 to 690°C and a pressure of 276 MPa for 30 minutes. The transmittance measured at wavelengths from 0.4 to 1.0 μm was highest for a material hot-pressed at 570°C that had a mean grain size of 0.37 μm and 99.8% of theoretical density. Transmittance deceased for materials hot-pressed at higher temperatures because of increased grain size. It was also lower for materials hot-pressed at temperatures less than 570°C due to lower densities. Both Lin *et al.* [16] and Chang *et al.* [17] showed that transmittance decreased significantly as grain size increased in the visible range, while it was less sensitive to grain size in the infra-red regime. However, there were no analyses of the data using theoretical models in either of the studies.

Apetz and van Bruggen [18] were the first to report on the processing and optical characterization of a transparent polycrystalline Al_2O_3. They reported an in-line transmittance of 70% in the visible range ($\lambda = 0.645$ μm) for a polycrystalline Al_2O_3 with a mean grain size of 0.3 μm and thickness of 0.8 mm. They achieved this significant result by starting with a pure Al_2O_3 powder with a mean particle size of 0.15 μm, consolidating the powder by slip or pressure casting deagglomerated and stabilized suspensions in water, sintering the compacts at a low temperature (1150-1250°C) for 2 hours to obtain closed

porosity, and hot-isostatic-pressing (HIPing) the sintered compacts at 1200-1400°C and 200 MPa pressure for 2 hours in argon. The in-line transmittance decreased with increasing grain size and was nearly zero for a grain size of 8 μm. Krell *et al.* [19] consolidated a high purity Al_2O_3 powder using the gel-casting method. Aqueous slurries were prepared at pH 4 or at pH 8-9 with solids loading of 76-78 wt%. After milling, degassing and drying, the cast bodies were sintered for 2 hours in air at 1240-1250°C. A final density greater than 99.9% of theoretical was achieved by HIPing with pressure of 200 MPa at various temperature between 1150 and 1400°C in argon [19]. The reported in-line transmittance was in the range, 56% to 2%, at the wavelength of 0.640 μm for polycrystalline Al_2O_3 with mean grain size ranging from 0.53 to 5 μm and thickness of 0.8 mm. Bernard-Granger and Guizard [20] studied the effect of CaO/TiO_2 co-doping on the optical transmittance of polycrystalline Al_2O_3. The Al_2O_3 slurries had 70 wt% of solid loadings and the total dopant concentration was fixed to 150 atomic ppm (75 ppm of CaO and 75 ppm of TiO_2). The Al_2O_3 slurries were slip cast in a porous plaster mold and then sintered at 1250 and 1287°C for the pure Al_2O_3 and at 1285°C for CaO/TiO2 co-doped Al_2O_3. HIPing was done at 1200°C for 15 hours with 200 MPa of pressure in argon. The results indicated that the doped specimen had higher transmittance (50% at wavelength of 0.6 μm) compared with pure Al_2O_3 specimen (35% of transmittance at wavelength of 0.6 μm). The higher transparency in the doped specimen was attributed to smaller grain size ($\overline{G^{dope}} = 0.47$ μm and $\overline{G^{pure}} = 0.56$ μm) and lower porosity ($V_p^{dope} = 0\%$ and $V_p^{pure} = 0.007\%$) [20]. Yamashita *et al.* [21] studied the effects of porosity on the optical transmittance of polycrystalline Al_2O_3. The high purity Al_2O_3 powder was pressed uniaxially at 50 MPa and then cold isostatically pressed (CIP) at 200MPa. The green compacts were sintered at

1300°C in air for 2 hours and HIPed at 1350 to 1500°C for 1 hour with an argon gas pressure of 150 MPa [21]. The results indicated that porosity had a significant effect on both in-line transmission and total forward scattering whereas grain size affected only in-line transmittance [21].

In birefringent polycrystalline ceramics, such as MgF_2 and Al_2O_3, in-line transmittance decreases with increasing grain size [16-21]. Figure 1.4 shows some representative data for three polycrystalline ceramics, spinel ($MgAl_2O_3$, cubic) [22], Al_2O_3 [18], and MgF_2 [4]. The birefringence of these ceramics are listed in Table 1.2. It is evident from Figure 1.4 and Table 1.2 that the decrease of in-line transmittance with grain size is most pronounced for MgF_2, which has the highest birefringence ($\Delta n_{max} = 0.012$), while the transmittance of $MgAl_2O_4$ is almost independent of grain size because it is cubic and non-birefringent ($\Delta n_{max} = 0$). Al_2O_3 exhibits intermediate behavior ($\Delta n_{max} = 0.008$). It is significant to note here that MgF_2 exhibits the highest amount of light attenuation due to birefringent grains even though it has the lowest value of the refractive index among the three ceramics. It is generally understood that light attenuation in birefringent polycrystalline ceramics is due to variations in the refractive index along the path of light traversing arbitrarily oriented grains. However, it cannot be explained simply by geometrical optics theory considering only light reflection and refraction at grain boundaries [18]. Apetz and van Bruggen [18] have given an excellent review of these general aspects of light transmission in birefringent ceramics.

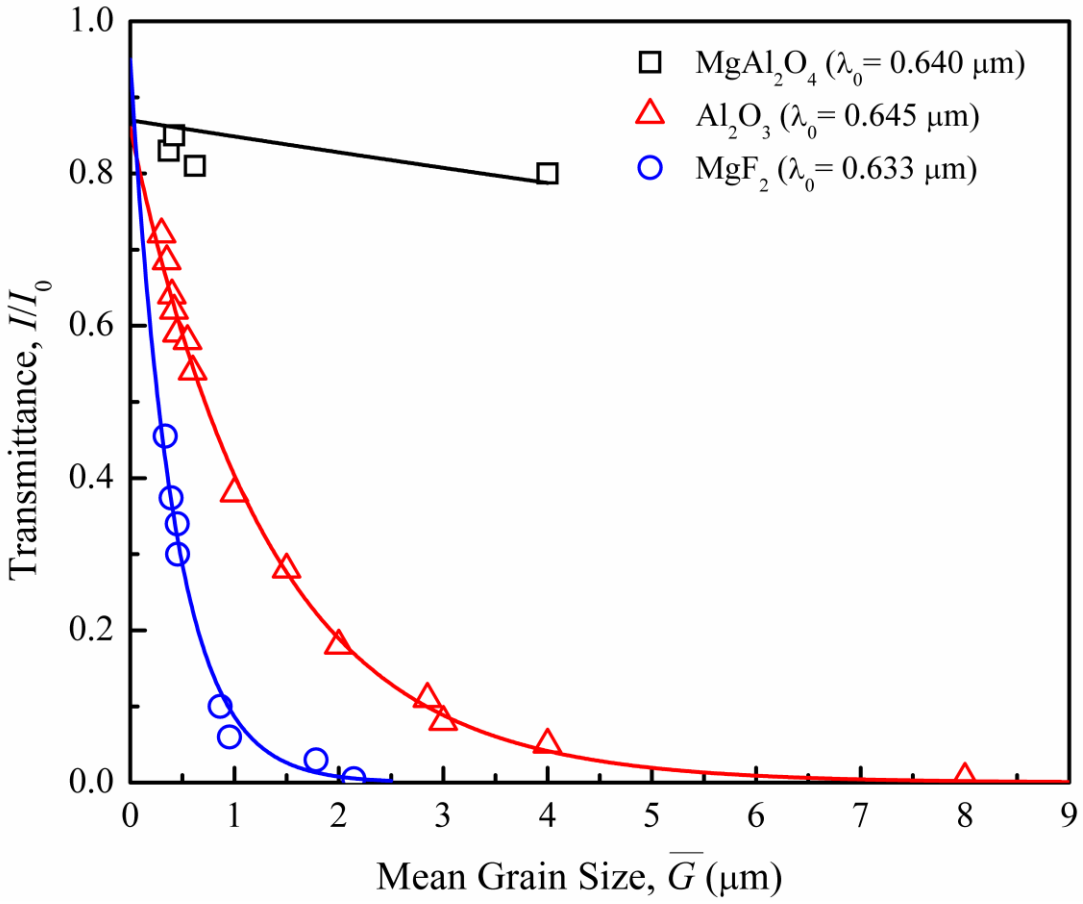

Figure 1.4 Variations of the transmittance of polycrystalline $MgAl_2O_4$, Al_2O_3, and MgF_2 as functions of the grain size at the indicated wavelengths.

1.4 Effect of Texture on Light Transmittance in Polycrystalline Ceramics

Mechanical and optical properties of polycrystalline ceramics can be enhanced by introducing texture during processing. There have been a number of studies on the processing of textured polycrystalline ceramics that result in anisotropic mechanical, thermal, electrical, and optical properties, similar to single crystals [23, 24]. Techniques available to produce texture in polycrystalline ceramics include extrusion, hot forging/deformation, and slip/tape casting with template or seeded grains.

Suzuki *et al.* [25-27] developed a method to produce texture in polycrystalline Al_2O_3 by colloidal processing in a strong magnetic field and high temperature sintering. The *c*-axis of the alumina particles align parallel to the direction of the magnetic field during slip casting and drying. The basal planes are perpendicular to the direction of the magnetic field. Mao *et al*. [28] subsequently confirmed these results. Figure 1.5 shows XRD patterns reported by Mao *et al*. [28] for sintered polycrystalline Al_2O_3 slip-cast with (Figures 1.5(a) and (b)) and without (Figure 1.5(c)) a magnetic field. Figure 1.5(a) is the XRD pattern on a surface normal to the magnetic field. The high intensity of the (006) peak in Figure 1.5(a) indicates a group of crystal planes perpendicular to the *c*-axis. Figure 1.5(b) is the XRD pattern on a surface parallel to the magnetic field. The strong (110) and (300) peaks correspond to planes parallel to the *c*-axis [28]. Figure 1.5(c) is the XRD pattern for a sintered polycrystalline Al_2O_3 that was slip-cast without the magnetic field. This pattern is typical of a polycrystalline Al_2O_3 with random grain orientations. Thus, the XRD patterns showed that grains in polycrystalline Al_2O_3 can be preferentially oriented by the magnetic field assisted slip casting method. Mao *et al.* [28] also reported that specimens

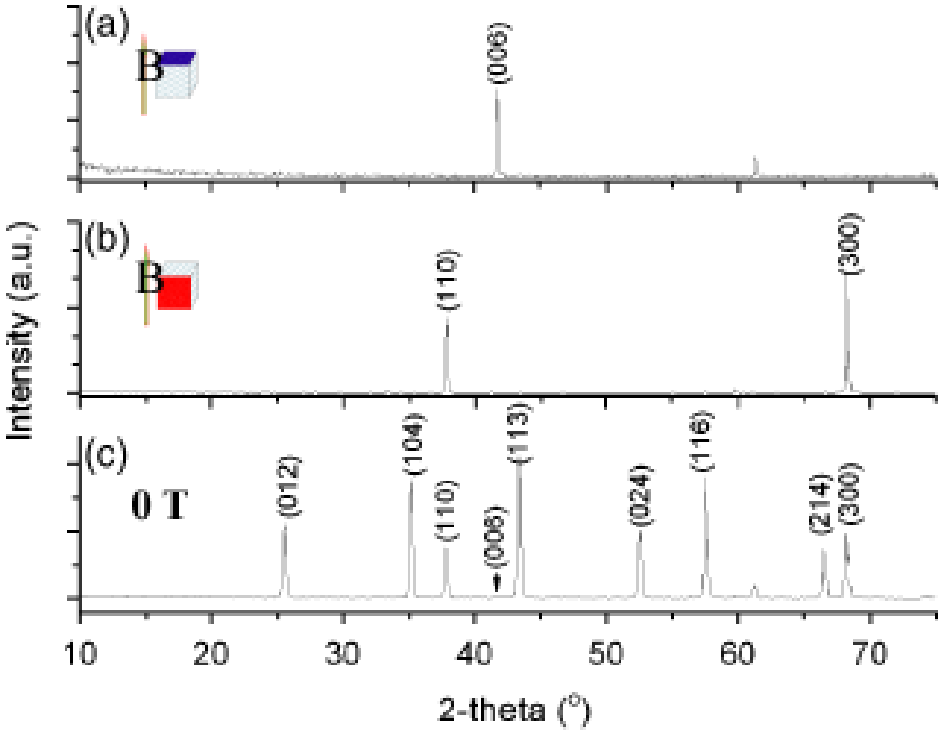

Figure 1.5 X-ray diffraction patterns of alumina slices cut (a) perpendicular to and (b) parallel to the magnetic field, and (c) slip cast without a magnetic field [28].

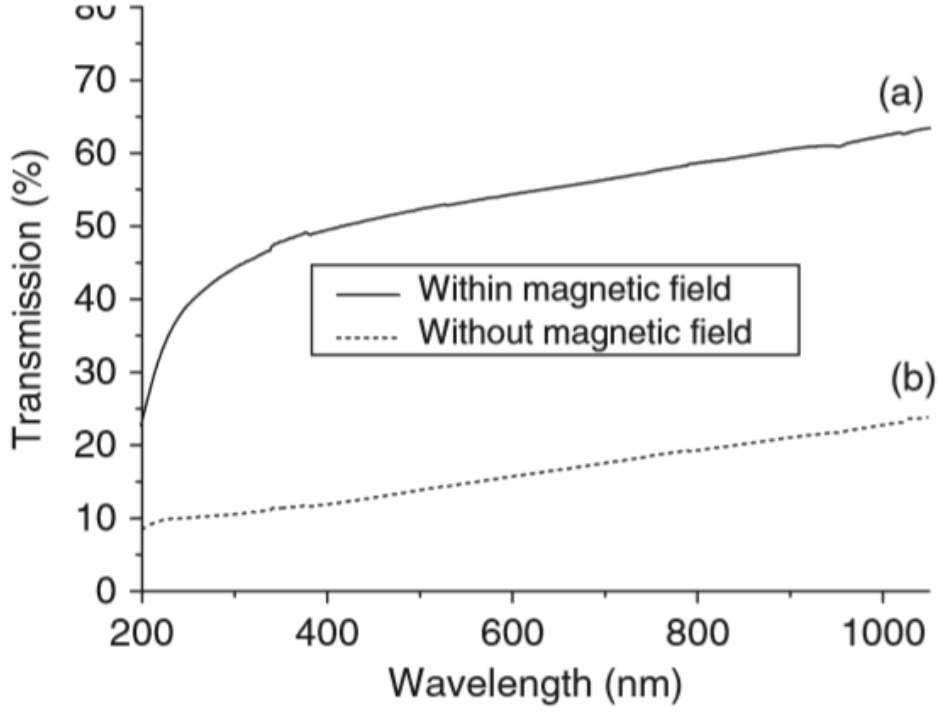

Figure 1.6 In-line transmittance of polycrystalline Al_2O_3 slip cast (a) in and (b) outside a magnetic field. Both samples are 0.8 mm thick and polished on both sides [28].

slip-cast in a strong magnetic field and followed by high temperature sintering (1850°C) exhibited a 40% higher optical transmittance than those prepared without using a magnetic field (see Figure 1.6).

1.5 Theoretical Models for Effect of Birefringence on Light Transmittance

The formulation of the scattering coefficient, γ, for grain-boundary attenuation depends on the theoretical approach used. The following sections summarize the formulations of γ for light attenuation in a birefringent polycrystalline ceramic treated as particle light scattering and light propagation in random media, respectively.

1.5.1 Grain-Boundary Attenuation as Particle Light Scattering

In this approach, suggested by Harrison [29] and Apetz and van Bruggen [18], a polycrystalline ceramic consisting of birefringent crystals is treated as a two-phase composite of isotropic spherical particles (diameter, d_p, and refractive index, n_p) dispersed in a homogeneous, isotropic matrix (refractive index, n_m). Grain-boundary attenuation is treated as the scattering of light by the spherical particles. In 1908, Mie [30] solved Maxwell's equation for the diffraction of a plane monochromatic wave by a homogeneous sphere surrounded by a medium with a different refractive index. His solution is of the form:

$$K = K(m, x) \tag{1.13}$$

In Eq. (1.13), K is the scattering efficiency of the particle, m is the relative refractive index, $m = n_p/n_m$, n_p is the refractive index of the spherical particle, n_m is the refractive index of the matrix, and x is the normalized particle size defined as follows:

$$x = \frac{\pi d_p n_m}{\lambda_0} \tag{1.14}$$

In Eq. (1.14), λ_0 is the wavelength of light in vacuum. Mie's solution for *K* as a function of the two fundamental parameters, *m* and *x*, consists of an infinite sum of terms involving spherical Bessel functions and associated Legendre polynomials, and can only be assessed using software. Figure 1.7 shows an example of the Mie solution in the form of a plot of the scattering efficiency, *K*, as a function of *x* for a fixed value of $m = 1.01$ calculated using MieCalc® [31]. A value of $m \sim 1$ was used here because the birefringence in polycrystalline ceramics of interest in optical applications, such as MgF_2 and Al_2O_3, is typically small. The scattering efficiency increases monotonically with increasing *x* in the range $x = 0$ to 100. Above this range, it reaches a peak and oscillates around an average value of ~2.

Mie's solution is rigorous and applicable for a spherical particle of arbitrary size and refractive index relative to the medium. RGD theory is a special case of Mie theory applicable under the following conditions [32]: (1) The refractive index of the particle is close to that of the medium, i.e., $|m - 1| \ll 1$. (2) The 'phase shift' is small, that is, $2x|m - 1| \ll 1$. And as a consequence of the above conditions, (3) the scattering efficiency is small, that is, $K << 1$. In the regime defined by these conditions, a large particle size approximation of the RGD theory is given by the following equation [32]:

$$K = 2(m - 1)^2 x^2 \tag{1.15}$$

The dashed line in Figure 1.7 is a plot of Eq. (1.15). It is noted that Eq. (1.15) is close to the Mie solution for values of *x* less than about 50. Apetz and van Bruggen [18] used Eq. (1.15) to model the effect of birefringence on light transmission in polycrystalline Al_2O_3.

The scattering coefficient of a two-phase system consisting of monodisperse

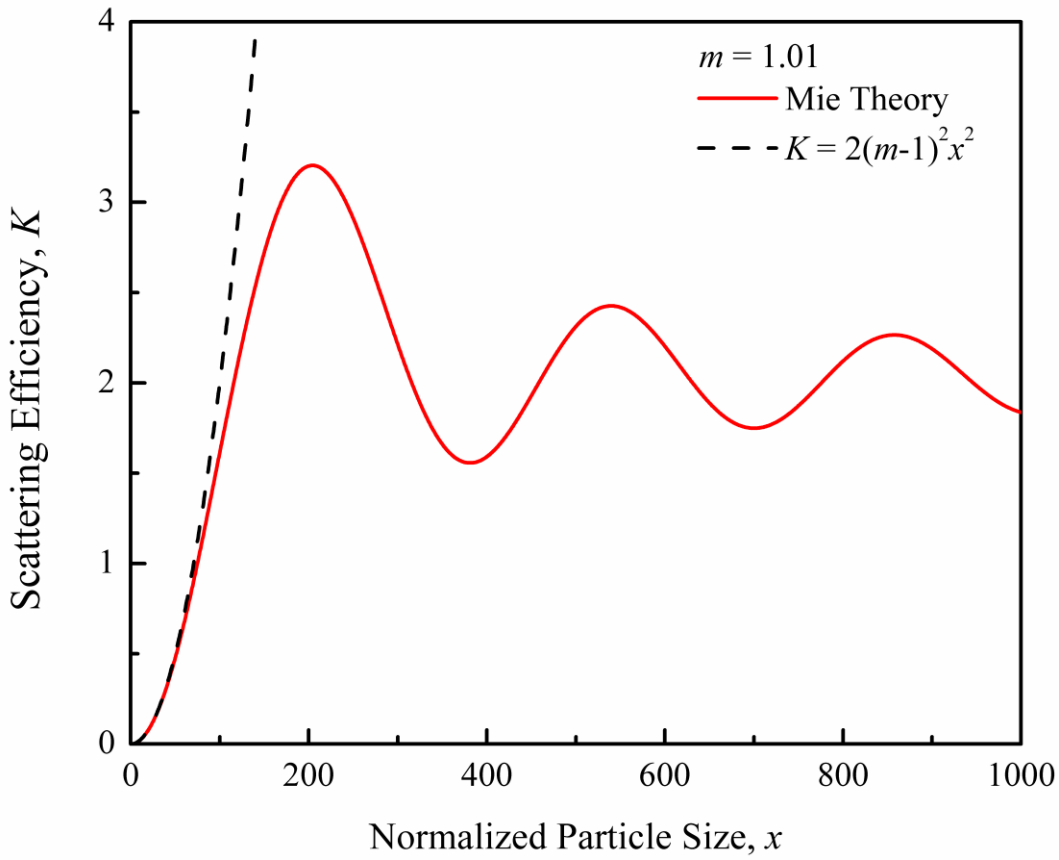

Figure 1.7 Variation of the scattering efficiency (K) as a function of normalized particle size (x) for a spherical particle in a medium with small mismatch in refractive index according to Mie theory and an approximation of the RGD theory.

spherical particles in a homogeneous medium is obtained from the single-particle scattering efficiency using the following equation [32]:

$$\gamma = \frac{N\pi d_{\mathrm{p}}^2 K}{4} \tag{1.16}$$

In Eq. (1.16), *N* is the number of particles per unit volume. Therefore, Eq. (1.16) is applicable to multiparticle systems only when there is no multiple scattering, i.e., for low concentrations of particles [32]. It is useful to express the scattering coefficient in terms of the volume fraction of the spherical particles, ϕ:

$$\gamma = \frac{3K\phi}{2d_{\mathrm{p}}} \tag{1.17}$$

If we employ the analytical approximation of Eq. (1.17) for *K* and substitute for *m* and *x*, Eq. (1.17) for the scattering coefficient takes the following form[3]

$$\gamma = \frac{3\pi^2 \phi d_{\mathrm{p}} \Delta n^2}{\lambda_0^2} \tag{1.18}$$

Apetz and van Bruggen [18] showed good agreement between experimental results and theoretical prediction using Eq. (1.18) for the assumed material parameters $\phi = 0.5$ and $\Delta n = 2/3(\Delta n_{max})$. We note here that there is uncertainty in establishing values of the two parameters, Δn and ϕ, for polycrystalline ceramics, which significantly affects the predicted values of the scattering coefficient and light transmittance.

1.5.2 Light Propagation in Random Media

The theory of wave propagation in random media was initially proposed by Debye and Bueche [33], and subsequently employed by others in various forms [34-37]. Raman

[3] See Appendix C for derivations of this equation.

and Viswanathan [34] assumed a polycrystalline material to be made of uniform, cube-shaped grains with edges of length, Δ, aligned along three optical axes with refractive indices, n_1, n_2 and n_3. An incident light ray traverses the polycrystalline material in a direction parallel to one set of edges covering a total number, N, of grains made up of k_1 grains of refractive index, n_1, k_2 grains of refractive index, n_2 and k_3 grains of refractive index, $n3$, through a window of thickness, t. The emergent wave-train was obtained by summing waves with appropriate amplitudes and phases for all possible integral values of k_1, k_2, and k_3 subject to the relation, $k_1+k_2+k_3 = N$:

$$y = P \sum_{k_1+k_2+k_3=N} \left(\frac{N!}{k_1!k_2!k_3!} \right) \left(p_1^{k_1} p_2^{k_2} p_3^{k_3} \right) e^{\frac{2\pi i}{\lambda_0}[c\tau - Z - (k_1 n_1 + k_2 n_2 + k_3 n_3)\Delta]} \tag{1.19}$$

In Eq. (1.19), y is the amplitude of the emergent wave, P is a factor that accounts for the loss in intensity of light due to reflections at the grain boundaries, and p_1, p_2, and p_3 are the fractions of grains with the three optical axes, respectively, τ is time, and Z is a reference position coordinate at $\tau = 0$. It is noted that the first two terms in parentheses in Eq. (1.19) represent the number of ways k_1, k_2, and k_3 grains can be arranged along the optical path and the probability of occurrence of each of the arrangements, respectively. The exponential term includes the change in amplitude and phase due to light retardation arising from the variation in refractive index along the light path. A number of mathematical manipulations of Eq. (1.20) lead to the following equation for the transmittance:

$$\frac{I}{I_0} = P^2 e^{-\frac{4\pi^2 \Delta \sum p_2 p_3 (n_2 - n_3)^2}{\lambda_0^2} t} \tag{1.20}$$

Or, the scattering coefficient due to the cumulative light retardation can be written as[4]

$$\gamma = \frac{4\pi^2 \Delta \sum p_2 p_3 (n_2 - n_3)^2}{\lambda_0^2} \tag{1.21}$$

It is interesting to note that Eq. (1.21) is essentially the same as Eq. (1.18) in terms of the dependence of the scattering coefficient on the parameters, particle size, d_p (or, grain size, Δ), the mismatch in the refractive index, Δn, and the wavelength of the incident light, λ_0.

The theory of Kahan *et al*. [37] is conceptually similar to that of Raman and Viswanathan [34], but their mathematical approach is quite different. They solve the scalar Helmholtz equation with a two-point correlation function and derive a general equation for the scattering coefficient for combined grain-boundary and pore scattering. They consider grains to have only two possible orientations corresponding to the highest and the lowest refractive index of the crystal. If pore scattering is negligible relative to grain-boundary scattering and the normalized mean grain intercept length is large ($x >> 1$), their equation for the scattering coefficient reduces to the following form[5]:

$$\gamma = \frac{8\pi^2 \Delta (p_1 p_2)(n_1 - n_2)^2}{\lambda_0^2} \tag{1.22}$$

It should be noted that Eq. (1.22) is similar to Eq. (1.21) in the dependence of γ on Δn, Δ, and λ_0. The absolute values of γ differ in the two expressions because of the different assumptions of the grain orientations in the two theories. Kahan *et al*. [37] assumed a more restrictive grain-orientation distribution (only two orientations), while Raman and Viswanathan [34] assumed three orientations. The comparisons of particle scattering theory

[4] See Appendix D for derivations of this equation.
[5] See Appendix E for derivations of this equation.

and wave retardation theory are discussed in Chapters 2, 3, and 4.

1.6 Research Objectives

The objectives of this research are to

(1) Examine the applicability of the particle scattering model of Apetz and van Bruggen and the theories of wave propagation in random media of (a) Raman and Viswanathan's model, and (b) Kahan's model to light transmission in noncubic polycrystalline ceramics.

(2) Employ a model system of a silica and water/glycerol mixture to test the applicability of the particle scattering theory.

(3) Fabricate high density and high transparency polycrystalline Al_2O_3 using the pressure filtration method. Alter the grain size of the hot-pressed polycrystalline MgF_2 by annealing the specimens in argon.

(4) Perform the measurements and analysis of optical transmittance and scattering coefficient as functions of grain size using birefringent polycrystalline ceramics.

(5) Study the effect of grain size on the angular scattering of polycrystalline Al_2O_3 using the measurement of scattering profile.

Chapter 2 is based on the paper entitled "On Effect of Birefringence on Light Transmittance in Polycrystalline Magnesium Fluoride," published in the *Journal of the American Ceramic Society* in 2015. Chapter 3 is based on the paper entitled "An Assessment of the Applicability of Particle Light Scattering Theories to Birefringent Polycrystalline Ceramics," published in the *Journal of the American Ceramic Society* in 2016. Chapter 4 is based on the paper entitled "Light Transmission in Polycrystalline Alumina: Effects of Birefringence and Grain Size" (to be submitted).

1.7 References

[1] D. C. Harris, "Durable 1-5 μm Transmitting Infrared Window Materials," *Infrared Phys. Techn*., 39, 185-201 (1998).

[2] D. C. Harris, *Materials for Infrared Windows and Domes: Properties and Performance*. SPIE Optical Engineering Press, Bellingham, WA, 1999.

[3] R. L. Gentilman, "Current and Emerging Materials for 3-5 Micron IR Transmission," 2-11. in *Infrared and Optical Transmitting Materials*, Vol 0683. Edited by R. W. Schwartz. Proc. SPIE. San Diego, CA, (1986).

[4] T.-C. Wen and D. K. Shetty, "Birefringence and Grain-Size Effects on Optical Transmittance of Polycrystalline Magnesium Fluoride," pp. 73020Z-1 - 20Z-6. in *Window and Dome Technologies and Materials XI*, Vol. 7302. Window and Dome Technologies and Materials. Edited by R. W. Tustison. SPIE: International Society for Optics and Photonics, Orlando, FL, 2009.

[5] T. D. McGee, *Principles and Methods of Temperature Measurement*; John Wiley & Sons, Inc., New York, 1988.

[6] R. L. Coble, *Transparent alumina and method of preparation* U.S. Patent 3026210 (1962).

[7] G. Bernard-Granger, C. Guizard and N. Monchalin, "Sintering of an Ultrapure α-Alumina Powder: II. Mechanical, Thermos-mechanical, Optical Properties, and Missile Dome Design," *Int. J. Appl. Ceram. Tech.*, **8** [2] 366-382 (2011).

[8] A. Yariv and P. Yeh, *Optical Waves in Crystals: Propagation and Control of Laser Radiation*. John Wiley & Sons, New York, NY (1984).

[9] Michael Bass, *Handbook of Optics, Volume I, Fundamentals, Techniques, and Design*. McGraw-Hill, Inc., New York, NY (1995).

[10] E. D. Palik, *Handbook of Optical Constants of Solids*, Section 3: Magnesium Fluoride (MgF_2), Page: 899-918, Edited by T. M. Cotter, M. E. Thomas and W. J. Tropf., Academic Press, 1998.

[11] M. J. Dodge, "Refractive Properties of Magnesium Fluoride," *Appl. Opt*., **23** [12] 1980-85 (1984).

[12] E. R. Dobrovinskaya, L. A. Lyvynov and V. Pishchik, *Sapphire: Material, Manufacturing, Applications.* Springer. New York, 2009.

[13] M. J. Dodge, "Refractive Index," in CRC *Handbook of Laser Science and Technology*, Edited by M. J. Weber, Vol IV, CRC Press, Boca Raton, FL, 1986.

[14] I. H. Malitson and M. J. Dodge, “Refractive Index and Birefringence of Synthetic Sapphire,” *J. Opt. Soc. Am.*, **62**, 1405, (1972).

[15] T.-C. Wen and D. K. Shetty, “On the Effect of Birefringence on Light Transmission in Polycrystalline Magnesium Fluoride,” *J. Am. Ceram. Soc.*, **98** [3] 829-837 (2015).

[16] W. Y. Lin, M. H. Hon and S. J. Yang, “Effect of Grain Growth on Hot-Pressed Optical Magnesium Fluoride Ceramics,” *J. Am. Ceram. Soc.*, **71**, C-136-C-137 (1988).

[17] C. S. Chang, M. H. Hon and S. J. Yang, “Effect of Grain Growth of Hot-Pressed Magnesium Fluoride on Optical Transmittance,” *Jpn. J. Appl. Phys.*, **30** [3] 506-510 (1991).

[18] R. Apetz and M. P. B. v. Bruggen, "Transparent Alumina: A Light-Scattering Model," *J. Am. Ceram. Soc.,* **86** [3] 480-86 (2003).

[19] A. Krell, P. Blank, H. Ma, T. Hutzler, M. P. B. v. Bruggen and R. Apetz, "Transparent Sintered Corundum with High Hardness and Strength," *J. Am. Ceram. Soc.*, **86** [1] 12-18 (2003).

[20] G. Bernard-Granger and C. Guizard, "Influence of Co-Doping on the Sintering Path and on the Optical Properties of a Submicronic Alumina Material," *J. Am. Ceram. Soc.*, **91** [5] 1703-06 (2008).

[21] I. Yamashita, H. Nagayama and K. Tsukuma, "Transmission Properties of Translucent Polycrystalline Alumina," *J. Am. Ceram. Soc.*, **91** [8] 2611-16 (2008).

[22] A. Krell, J. Klimke and T. Hutzler, "Advanced Spinel and Sub-mm Al_2O_3 for Transparent Armour Applications," *J. Eur. Ceram. Soc.*, **29** 275-91 (2009).

[23] P. W .Hall, J.S. Swinnea and D. Kovar, “Fracture Resistance of Highly Textured Alumina,” *J. Am. Ceram. Soc.*, **84** [7] 1514-1520 (2001).

[24] D. Brandon, D. Chen and H. Chan, “Control of Texture in Monolithic Alumina,” *Mater. Sci. Eng.* A **195** 189-196 (1995).

[25] T. Uchikoshi, T. S. Suzuki, H. Okuyama and Y. Sakka, “Control of Crystalline Texture in Polycrystalline Alumina Ceramic by Electrophoretic Deposition in a Strong Magnetic Field,” *J. Mater. Res.* **19** [5] 1487-1491 (2004).

[26] T. S. Suzuki, T. Uchikoshi and Y. Sakka, “Control of Textured by Colloidal Processing in a Strong Magnetic Field,” *Sci. Tech. Adv. Mater*. **7**, 356-364 (2006).

[27] T. S. Suzuki, Y. Sakka and K. Kitazawa, “Orientation Amplification of Alumina by Colloidal Filtration in a Strong Magnetic Field and Sintering,” *Adv. Eng. Mater*. **3**

No.7 490-492 (2001).

[28] X. Mao, S. Wang, S. Shimai and J. Guo, “Transparent polycrystalline alumina ceramics with orientated optical axes” *J. Am. Ceram. Soc*. **91** [10] 3431-3433 (2008).

[29] W. H. Harrison, “Optical Model”; pp. 209-19 Section 3.0 in *Advanced Optical Ceramics*, Phase II, Annual Report, General Electric Company, ONR Contract N00014-78-C-0466, August 31, 1980.

[30] G. Mie, "Contributions on the Optics of Turbid Media - Particularly Colloidal Metal Solutions," *Ann. Phys*., 330 [3] 377-445 (1908).

[31] B. Michel, MieCalc-Freely Configurable program for Light Scattering Calculations (Mie Theory), http://www.lightscattering.de/MieCalc/eindex.html, (accessed 13 May 2014)

[32] H. C. van de Hulst, *Light Scattering by Small Particles*. Dover Publications, Inc., New York, 1981.

[33] P. Debye and A. M. Bueche, “Scattering by an Inhomogeneous Solid,” *J. App. Phys*., **20**, 518-525 (1949).

[34] C. V. Raman and K. S. Viswanathan, “The Theory of the Propagation of Light in Polycrystalline Media,” *Proc. Ind. Acad. Sci*. A, **41**, 37-43 (1955).

[35] J. B. Keller, “Wave Propagation in Random Media”; pp. 227-46 *in Hydrodynamic Instability*, Proc. Symp. Appl. Math., Vol. XIII, G. Birkhoff, R. Bellman and C. C. Lin (Eds.); American Mathematical Society, 190 Hope St., Providence, RI (1962).

[36] G. S. Ranganath and S. Ramaseshan, “Optical Transmission in Polycrystals,” *Optica Acta*, **19** [9] 781-90 (1972).

[37] H. M. Kahan, D. P. Stubbs and R. V. Jones, "The Potentialities of Fine Grained Ceramics for Optical and Acoustical Applications," pp. 185-203. in *Optical and Acoustical Micro-Electronics*, Edited by J. Fox. Polytechnic Press, Brooklyn, NY, 19745, 1975.

CHAPTER 2

ON THE EFFECT OF BIREFRINGENCE ON LIGHT TRANSMISSION IN POLYCRYSTALLINE MAGNESIUM FLUORIDE

2.1 Introduction

Light transmission in polycrystalline ceramics is affected by several intrinsic and extrinsic factors. The intrinsic factors include atomic bonding and crystal structure, while the extrinsic factors include surface finish, void and second-phase sizes and concentrations, and grain size in birefringent polycrystalline materials. Ionic bonding, elements of low atomic weights, cubic crystal structure, optically-smooth surfaces, low concentrations and small sizes of second phases including voids, and small grain size in noncubic crystal structures promote high transmittance in ceramics. The effects of most intrinsic and extrinsic factors on light transmission in ceramics are well understood and discussed in several books and articles [1-6].

Noncubic polycrystalline ceramics are birefringent, i.e., the refractive index varies in different crystallographic directions. In birefringent polycrystalline ceramics, such as magnesium fluoride (MgF_2, tetragonal) and alumina (Al_2O_3, hexagonal close-packed), the in-line transmittance decreases with increasing grain size [7-13]. Figure 2.1 shows representative data for three polycrystalline ceramics, spinel ($MgAl_2O_3$, cubic) [14], alumina [11], and magnesium fluoride [9]. The birefringence of these ceramics, defined by $\Delta n_{max} = (n_e - n_o)$, where n_e is the refractive index in the extra-ordinary direction and n_o is

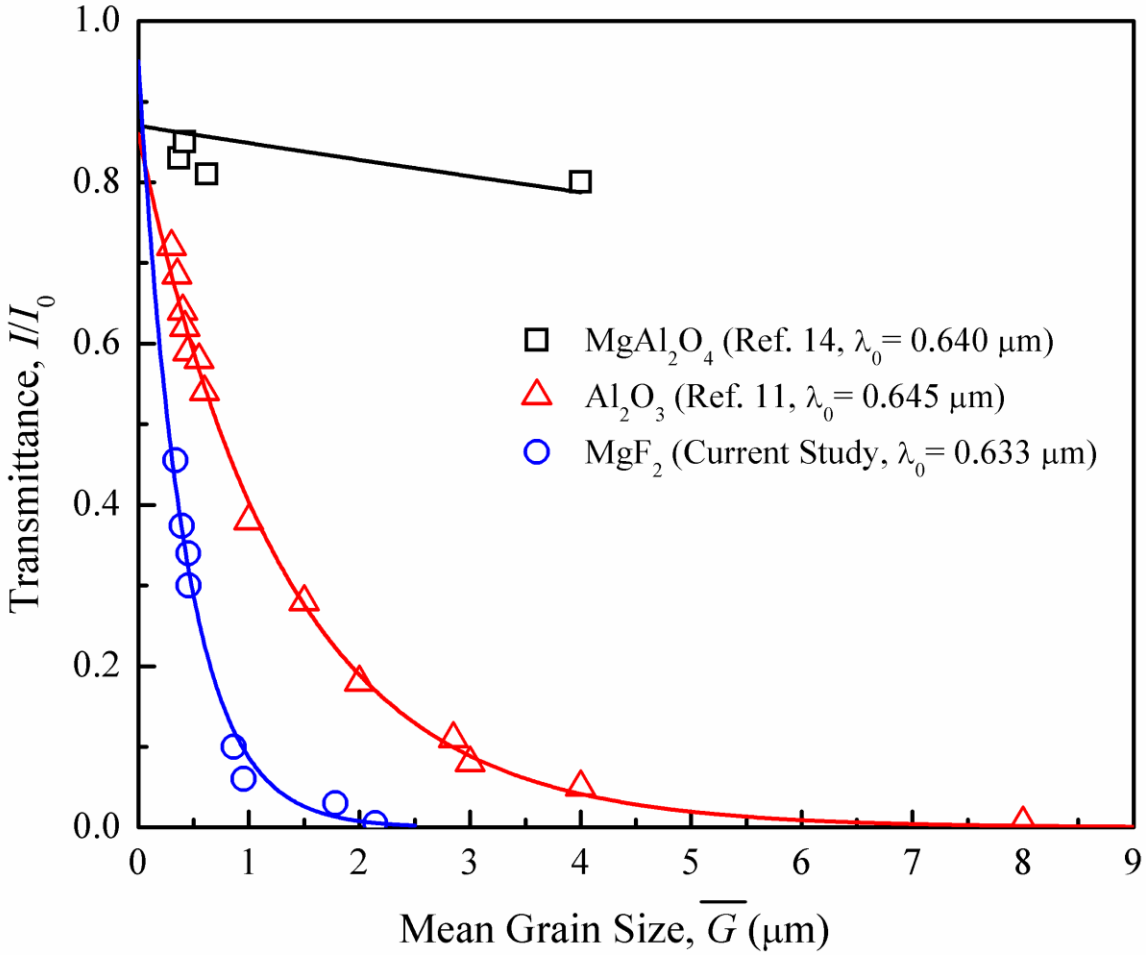

Figure 2.1 Variations of the transmittance of polycrystalline $MgAl_2O_4$, Al_2O_3 and MgF_2 as functions of the grain size at the indicated wavelengths (birefringence for Al_2O_3 and MgF_2 are listed in Table 2.1).

the refractive index in the ordinary direction [1], is listed in Table 2.1. It is evident from Figure 2.1 that the decrease of the in-line transmittance with grain size is most pronounced for MgF_2, which has the highest birefringence ($\Delta n_{max} = 0.012$), while the transmittance of $MgAl_2O_4$ is almost independent of grain size because it is cubic and nonbirefringent ($\Delta n_{max} = 0$). Al_2O_3 exhibits intermediate behavior ($\Delta n_{max} = 0.008$). It is pointed out here that MgF_2 exhibits the highest amount of light attenuation due to birefringent grains even though it has the lowest value of the refractive index among the three ceramics. It is generally understood that light attenuation in birefringent polycrystalline ceramics is due to variations in the refractive index along the path of light traversing arbitrarily oriented grains. However, it cannot be explained simply by geometrical optics theory considering only light reflection and refraction at grain boundaries [11]. Apetz and van Bruggen [11] have given an excellent review of these general aspects of light transmission in birefringent ceramics.

The effect of birefringence on light transmission in polycrystalline ceramics has been treated in two different ways. Apetz and van Bruggen [11] treated a birefringent polycrystalline ceramic as a two-phase composite of isotropic spherical particles with a refractive index, n_p, dispersed in an isotropic matrix of refractive index, n_m. They assumed that the difference in the refractive indices, $\Delta n = (n_p - n_m)$, was related to the intrinsic birefringence, Δn_{max}, of the crystal, and the particle diameter, d_p, was the average grain size. Since the relative refractive index, $m = n_p/n_m$ is nearly 1 for polycrystalline alumina, they used the large particle size limiting form of the Raleigh-Gans-Debye (RGD) theory of light scattering by spherical particles. The decrease of the transmittance of polycrystalline alumina with average grain size was in good agreement with the RGD theory for the

Table 2.1 The isotropic refractive index of $MgAl_2O_4$ and the refractive indices in the ordinary (n_o) and the extraordinary (n_e) directions for Al_2O_3 and MgF_2 at different wavelengths.

Materials	λ_0 (μm)	n_o	n_e	$\lvert\Delta n_{max}\rvert$
$MgAl_2O_4$	0.640	1.7134	1.7134	0
Al_2O_3	0.645	1.7653	1.7573	0.008
MgF_2	0.633	1.3770	1.3888	0.0118
MgF_2	1.064	1.3732	1.3848	0.0116
MgF_2	3.39	1.3560	1.3664	0.0104

assumed material parameters, volume fraction of grains, $\phi = 0.5$, and $\Delta n = 2\Delta n_{max}/3$.

Raman and Viswanathan [15], on the other hand, treated light transmission in polycrystalline ceramics as a light retardation problem. As a light ray passes through grains of different orientations in a polycrystalline ceramic, its velocity varies in each grain and the cumulative effect of all the grains in the light path is accounted for by taking into account both the path length in each grain and the grain orientation distribution. Ranganath and Ramaseshan [16] extended the theory by including the effect of change in polarization of the light during its passage through the polycrystalline material. There has been no attempt to date to quantitatively compare this theory with transmission measurements in polycrystalline ceramics.

Kahan *et al.* [17] treated wave propagation in polycrystalline ceramics using a scalar Helmholtz equation for an appropriate scalar amplitude function. They derived equations for the scattering coefficient and the Rayleigh ratio in terms of a two-point correlation function with two terms, one corresponding to pore scattering and the other for grain-boundary scattering. The variation of the measured scattering coefficient with porosity in high-density alumina (LUCALOX®) was consistent with their theory. Schroeder and Rosolowski [3] used this theory to rationalize the variations of the width of the scattering profiles with specimen thickness and grain size of high-density alumina (LUCALOX®). It is shown in this paper that the theoretical approach of Kahan *et al.* [17]. is similar to that of Raman and Viswanathan [15] and results in a similar equation for the scattering coefficient under the conditions of the experiments in this study.

The purpose of this paper is to critically examine the applicability of the particle scattering model of Apetz and van Bruggen [11] and the light retardation theory of Raman

and Viswanathan [15] to light transmission in polycrystalline MgF_2. Although the effect of grain size on light transmission in polycrystalline MgF_2 has been reported in prior studies [8, 9], the data were not critically examined and compared with the theories. In this study, the in-line transmission measurements were used to assess the two theoretical approaches. It is shown that the measured variations of the scattering coefficient of MgF_2 with grain size and wavelength of light are qualitatively consistent with both the theories. Quantitative predictions of the theories, however, can vary significantly due to the uncertain values of the material parameters that appear in each model: particle (or grain) volume fraction, ϕ, and the average refractive index mismatch, Δn, in the particle light scattering model; and the grain orientation distribution and the average refractive index variation along the light path in the light retardation theory. The paper also shows that transmittance predicted by particle-scattering models are particularly sensitive to grain-size distribution in addition to the effect of average grain size.

2.2 Theoretical Background

The intensity of light transmitted through a window of thickness, t, that partially scatters light in the bulk and reflects at the two surfaces is given by the following equation [1]:

$$I(t) = I_0 \left[\frac{(1-R)^2 e^{-\gamma t}}{1 - R^2 e^{-2\gamma t}} \right] \tag{2.1}$$

In Eq. (2.1), I_0 is the intensity of the incident light, R is the single-surface reflectance, and γ is the scattering coefficient that accounts for the light scattered and/or absorbed in the material. For a window with optically smooth surfaces and negligible absorption, the single-surface reflectance is given by the following equation [1]:

$$R = \left(\frac{1-n}{1+n}\right)^2 \tag{2.2}$$

In Eq. (2.2), n is the average refractive index of the window. The formulation of the scattering coefficient, γ, for grain-boundary attenuation depends on the theoretical approach used. In the following, we briefly summarize the formulations of γ for light attenuation in a birefringent polycrystalline ceramic treated as particle light scattering and light propagation in random media, respectively.

2.2.1 Grain-Boundary Attenuation as Particle Light Scattering

In this approach, suggested by Apetz and van Bruggen [11], a polycrystalline ceramic consisting of birefringent crystals is treated as a two-phase composite of isotropic spherical particles (diameter, d_p, and refractive index, n_p) dispersed in a homogeneous, isotropic matrix (refractive index, n_m). Grain-boundary attenuation is treated as scattering of light by the spherical particles. In 1908, Mie [18] solved Maxwell's equation for the diffraction of a plane monochromatic wave by a homogeneous sphere surrounded by a medium of different refractive index. His solution is of the form:

$$K = K(m, x) \tag{2.3}$$

In Eq. (2.3), K is the scattering efficiency of the particle, m is the relative refractive index defined earlier, and x is the normalized particle size defined as:

$$x = \frac{\pi d_p n_m}{\lambda_0} \tag{2.4}$$

In Eq. (2.4), λ_0 is the wavelength of light in vacuum. Mie's solution for K as a function of the two fundamental parameters, m and x, consists of an infinite sum of terms involving spherical Bessel functions and associated Legendre polynomials, and can only

be assessed using a software. Figure 2.2 shows an example of the Mie solution in the form of a plot of the scattering efficiency, K, as a function of x for a fixed value of m = 1.01 calculated using MieCalc® [19]. A value of $m \sim 1$ was used here because birefringence in polycrystalline ceramics of interest in optical applications, such as magnesium fluoride and alumina, is typically small. The scattering efficiency increases monotonically with increasing x in the range, x = 0 to 100. Above this range, it reaches a peak and oscillates around an average value of ~2.

Mie's solution is rigorous and applicable for a spherical particle of arbitrary size and refractive index relative to the medium. RGD theory is a special case of Mie theory applicable under the following conditions [20]: (1) The refractive index of the particle is close to that of the medium, i.e., $|m - 1| << 1$. (2) The 'phase shift' is small, i.e., $2x|m - 1| << 1$. And as a consequence of the above conditions, (3) the scattering efficiency is small, i.e., $K << 1$. In the regime defined by these conditions, a large particle size approximation of the RGD theory is given by the following equation [20]:

$$K = 2(m-1)^2 x^2 \tag{2.5}$$

The dashed line in Figure 2.2 is a plot of Eq. (2.5). It is noted that Eq. (2.5) is close to the Mie solution for values of x less than about 50. Apetz and van Bruggen [11] used Eq. (2.5) to model the effect of birefringence on light transmission in polycrystalline alumina.

The scattering coefficient of a two-phase system consisting of monodisperse spherical particles in a homogeneous medium is obtained from the single-particle scattering efficiency using the following equation [20]:

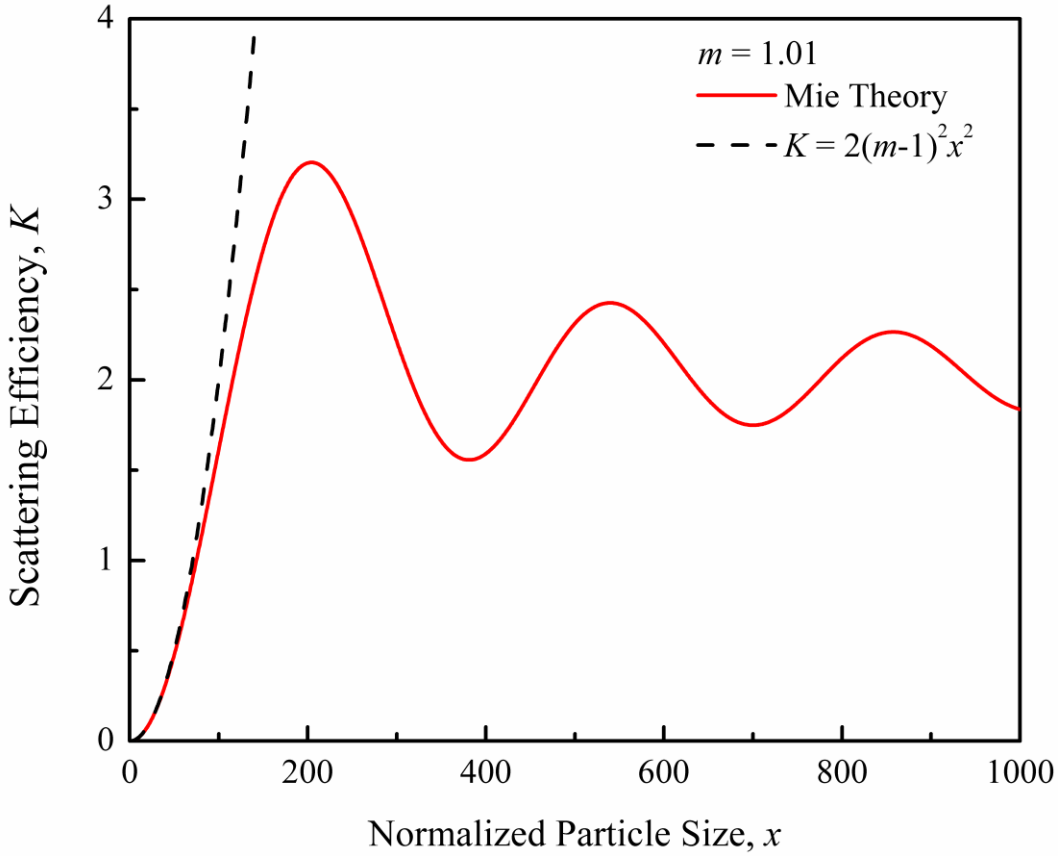

Figure 2.2 Variation of the scattering efficiency (K) as a function of the normalized particle size (x) for a spherical particle in a medium with small mismatch in refractive index according to Mie theory and an approximation of the RGD theory.

$$\gamma = \frac{N\pi d_p^2 K}{4} \tag{2.6}$$

In Eq. (2.6), N is the number of particles per unit volume. It is emphasized here that K is the scattering efficiency for single scattering by an isolated spherical particle. Therefore, Eq. (2.6) is applicable to multiparticle systems only when there is no multiple scattering, i.e., for low concentrations of particles [20]. It is useful to express the scattering coefficient in terms of the volume fraction of the spherical particles, ϕ:

$$\gamma = \frac{3K\phi}{2d_p} \tag{2.7}$$

If we employ the analytical approximation of Eq. (2.5) for K and substitute for m and x, Eq. (2.7) for the scattering coefficient takes the following form:

$$\gamma = \frac{3\pi^2 \phi d_p \Delta n^2}{\lambda_0^2} \tag{2.8}$$

Equation (2.8) is the same as the one derived by Apetz and van Bruggen [11] where they assumed $\phi = 0.5$ and $\Delta n = 2\Delta n_{max}/3$. We note here that there is uncertainly in establishing values of the two parameters, Δn and ϕ, for polycrystalline ceramics and this affects the predicted values of the scattering coefficient and light transmittance significantly.

2.2.2 Light Propagation in Random Media

Raman and Viswanathan [15] assumed a polycrystalline material to be made of uniform, cube-shaped grains with edges of length, Δ, aligned along three optical axes with refractive indices, n_1, n_2 and n_3. An incident light ray traverses the polycrystalline material in a direction parallel to one set of edges covering a total number, N, grains made up of k_1 grains of refractive index, n_1, k_2 grains of refractive index, n_2 and k_3 grains of refractive

index, n_3, through a window of thickness, t. The emergent wave-train was obtained by summing waves with appropriate amplitudes and phases for all possible integral values of k_1, k_2 and k_3 subject to the relation, $k_1+k_2+k_3 = N$:

$$y = P \sum_{k_1+k_2+k_3=N} \left(\frac{N!}{k_1!k_2!k_3!} \right) \left(p_1^{k_1} p_2^{k_2} p_3^{k_3} \right) e^{\frac{2\pi i}{\lambda_0}[c\tau - Z - (k_1 n_1 + k_2 n_2 + k_3 n_3)\Delta]} \tag{2.9}$$

In Eq. (2.9), y is the amplitude of the emergent wave, P is a factor that accounts for the loss in intensity of light due to reflections at the grain boundaries, and p_1, p_2 and p_3 are the fractions of grains with the three optical axes, respectively, τ is time, and Z is a reference position coordinate at $\tau = 0$. It is noted that the first two terms in parentheses in Eq. (2.9) represent the number of ways k_1, k_2 and k_3 grains can be arranged along the optical path and the probability of occurrence of each of the arrangements, respectively. The exponential term includes the change in amplitude and phase due to light retardation arising from the variation in refractive index along the light path. A number of mathematical manipulations of Eq. (2.9) lead to the following equation for the transmittance:

$$\frac{I}{I_0} = P^2 e^{-\frac{4\pi^2 \Delta \sum p_2 p_3 (n_2 - n_3)^2}{\lambda_0^2} t} \tag{2.10}$$

Or, the scattering coefficient due to the cumulative light retardation can be written as

$$\gamma = \frac{4\pi^2 \Delta \sum p_2 p_3 (n_2 - n_3)^2}{\lambda_0^2} \tag{2.11}$$

It is interesting to note that Eq. (2.11) is essentially similar to Eq. (2.8) in terms of the dependence of the scattering coefficient on the parameters, particle size, d_p (or, grain size, Δ), the mismatch in the refractive index, Δn, and the wavelength of the incident light, λ_0.

The theory of Kahan *et al*. [17] is conceptually similar to that of Raman and Viswanathan [15], but their mathematical approach is quite different. They solve the scalar Helmholtz equation with a two-point correlation function and derive a general equation for the scattering coefficient for combined grain-boundary and pore scattering. They consider grains to be oriented only in two possible orientations corresponding to the highest and the lowest refractive index of the crystal. If pore scattering is negligible relative to grain-boundary scattering and the normalized mean grain intercept length is large ($x >> 1$), their equation for the scattering coefficient reduces to the following form:

$$\gamma = \frac{8\pi^2 \Delta (p_1 p_2)(n_1 - n_2)^2}{\lambda_0^2} \tag{2.12}$$

It should be noted that Eq. (2.12) is similar to Eq. (2.11) in the dependence of γ on Δn, Δ, and λ_0. The absolute values of γ differ in the two expressions because of the different assumptions of the grain orientations in the two theories. Kahan *et al.* [17] assumed a more restrictive grain-orientation distribution (only two orientations), while Raman and Viswanathan [15] assumed three orientations. This study focuses mainly on comparing the measured transmittance of polycrystalline MgF_2 with the theoretical formulations of the scattering coefficient, γ, based on the RGD theory (Eq. (2.8)) and that based on the wave retardation theory (Eq. (2.11)).

2.3 Experimental Procedures

2.3.1 Processing of Dense Polycrystalline MgF_2

Dense billets of polycrystalline MgF_2 were obtained from Chung Shan Institute of Science and Technology, Taoyuan, Republic of China. The billets were processed by hot-pressing MgF_2 powder at 580ºC and 276 MPa pressure for 30 minutes. The as-hot-pressed

material had an average grain size, $\overline{G_N}\approx$ 0.33 μm. Scanning electron microscope (SEM) examination of the polished surfaces of showed no evidence of residual porosity. In order to increase the average grain size, small sections (25 x 25 x 2 mm) of the billets were annealed at temperatures varying from 600 to 800ºC for 1 hour in argon. The specimens were ground successively on SiC papers (grit numbers, 180, 320 and 400) and polished with diamond paste with 15, 9, 6, 3 and 1μm particles on both faces. The final thickness of the specimens was 1.0 mm and the root mean square roughness (R_q), as measured with a surface profilometer, was 10 nm.

2.3.2 Measurements of Grain Size and Orientation by Electron Backscatter Diffraction (EBSD)

The grain sizes and orientations in the polycrystalline MgF_2 were characterized by EBSD. The principles and applications of this technique have been described in several review articles [21, 22]. Grain orientation is determined from the characteristic electron backscatter diffraction (Kikuchi) pattern obtained from a bulk sample in a scanning electron microscope (SEM) equipped with EBSD hardware and software. Grain sections are mapped from the change in grain orientation across grain boundaries. This is also referred to as orientation imaging microscopy (OIM) [21]. A field emission gun scanning electron microscope (Phillips XL/30 FEGSEM, Eindhoven, Netherlands) equipped with a sensitive CCD camera and EBSD software (OIM Analysis and Data Collection, Version 7, EDAX) was used in the present study. The SEM was operated at 20 kV and 3 nA beam current and EBSD patterns collected at 50 or 70 nm per step and 100 steps/s. The EBSD data collected over a mapped region were transformed to an orientation image, such as the one shown in Figure 2.3 for polycrystalline MgF_2 annealed at 700°C, by assigning colors

to grains of different orientations as indicated by the standard projection triangle. In this process of image creation, the software employs two clean-up functions: neighbor-orientation correlation and grain confidence index (CI) standardization. Both functions operate by examining each data point individually, comparing to its neighbors, and removing unreliable or nonindexed points from the map. Then, the software replaced the unreliable data with more reliable orientation from neighboring pixels. However, the points with lower than 0.1 confidence index were excluded from the image. These nonindexed pixels are indicated by black color (see Figure 2.3). Error in grain size is reduced to less than 5% when 90% of image area is indexed using image clean-up functions [22]. The percent of image area indexed is a function of the average grain size and it typically exceeds 90% for an average grain size greater than 1 μm in an FEGSEM [22]. In Figure 2.3, for example, 98.7% of the image area was indexed by the software. Although a highest spatial resolution of 15 nm is feasible and quoted, the practical limit of the grain size that can be measured currently with EBSD mapping is 0.2 μm [21]. An orientation angle resolution in the range, 0.5-1°, is quoted for the EBSD technique [22].

The EBSD software calculates a mean linear grain intercept length, $\bar{L}_x$, in the x-direction using the following equation:

$$\bar{L}_x = \frac{R_x P_x \delta}{N_x} \tag{2.13}$$

In Eq. (2.13), R_x is the number of rows scanned in the x direction, P_x is the number of pixels in each row, δ is the scan step distance between pixels, and N_x is the total number of grain-boundary intersections in all the rows. A mean linear grain intercept length, $\bar{L}_y$, in the y-direction was similarly calculated. In the MgF_2 investigated in this study, the two mean

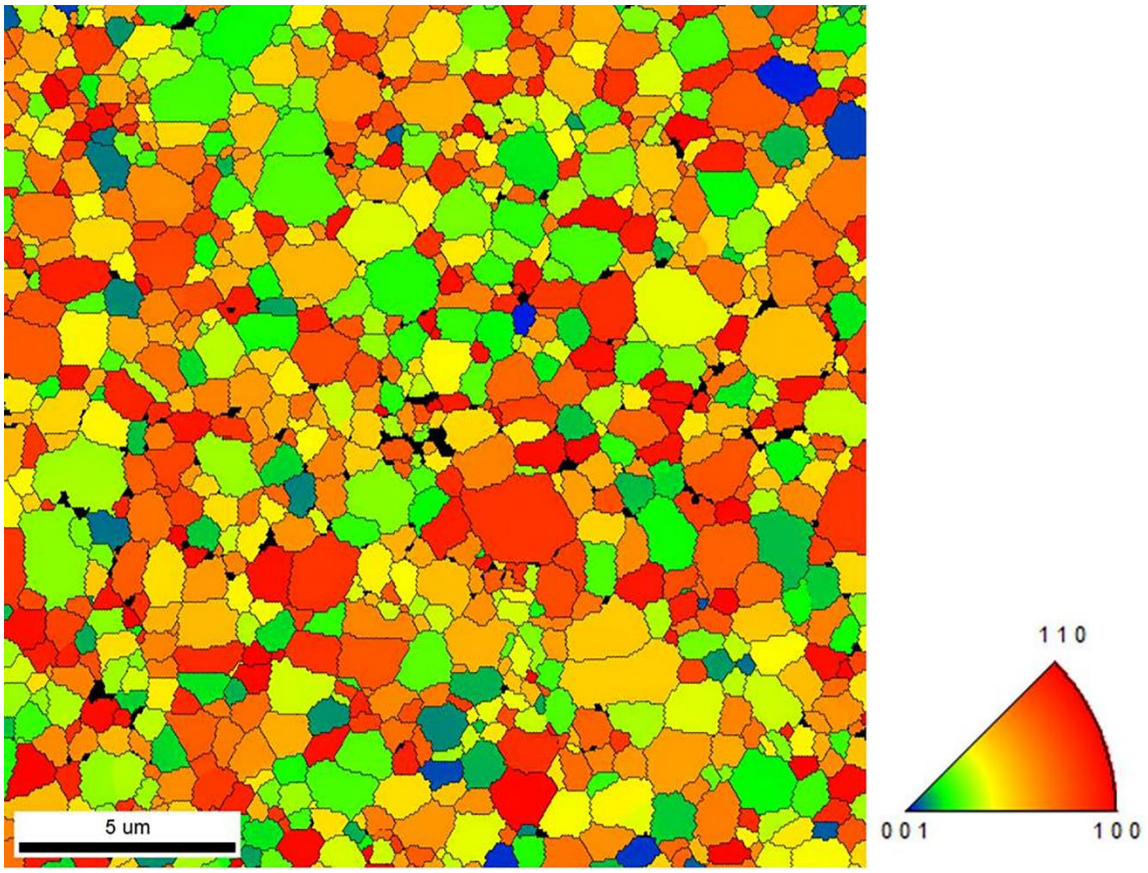

Figure 2.3 Microstructure of polycrystalline MgF_2 annealed at 700°C for 1 hour as revealed by EBSD. The color key for orientation is shown by the standard triangle.

linear intercept lengths were nearly identical. In other words, the grains were equiaxed. In Eq. (2.13), R_x is the number of rows scanned in the x direction, P_x is the number of pixels in each row, δ is the scan step distance between pixels, and N_x is the total number of grain-boundary intersections in all the rows. A mean linear grain intercept length, $\overline{L}_y$, in the y-direction was similarly calculated. In the MgF_2 investigated in this study, the two mean linear intercept lengths were nearly identical. In other words, the grains were equiaxed. Therefore, a mean linear intercept length, $\overline{L}$, was calculated as the mean of $\overline{L}_x$ and $\overline{L}_y$. A mean grain size, $\overline{G}$, was calculated from the mean linear intercept length, $\overline{L}$, using the following equation [23]:

$$\bar{G} = 1.558\bar{L} \tag{2.14}$$

In Eq. (2.14), the constant of proportionality arises from a stereological analysis that relates the average grain size of a log-normal distribution of sizes of grains in the shape of tetrakaidecahedron [23]. In addition to the mean intercept lengths, the software also provided intercept-length distributions and grain-orientation distributions from the EBSD data of a mapped region. These result are presented in Chapter 2.4.

2.3.3 Measurement of In-Line Transmittance

In-line transmittance of the polycrystalline specimens, I/I_0, were measured using three systems: (a) single wavelength laser and detector system on an optical bench, (b) a spectrophotometer operating in a wavelength range from 190 to 1100 nm, and (c) an FTIR (Fourier Transform Infra Red) operating in a wavelength range, 1.66 to 10 μm.

Figure 2.4 shows a schematic of the light source, specimen and detector used in the single wavelength laser and detector system. Lasers of three different wavelengths, 633 nm

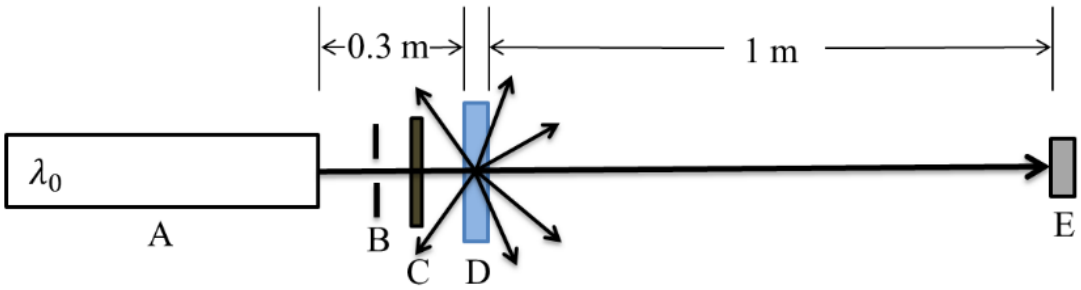

Figure 2.4 Schematic of the optical setup used in transmittance measurements using single wavelength lasers. A: laser, B: aperture, C: filter, D: specimen, E: detector.

(He-Ne laser, model 1122, JDS Uniphase, Milpitas, CA), 1.064 μm (YAG laser, model 4400, Quantronix Corp., East Setauket, NY), and 3.39 μm (He-Ne laser, model R-32172, Newport, Irvine, CA) were used in the single wavelength laser measurements. A Si detector was used to measure the incident (I_0) and the transmitted (I) intensities of the 633 nm and 1.064 μm lasers. A PbSe detector (model PDA20H, Thor Labs, Newton, NJ) was employed with the 3.39 μm laser. The long distance between the specimen and the detector (1 m) and the small active area of the detector ensured a small solid angle, ~0.5°, for measuring the light intensities. Because of this characteristic, transmittance measurements with the single-wavelength laser and detector system are sometimes referred to as real-in-line transmittance (RIT) [11].

In-line transmittance (IT) was also measured with two commercial instruments, a spectrophotometer (UV mini-1240, Shimadzu, Japan) and an FTIR (Excalibur 3100, Varian Inc., Palo Alto, CA). The spectrophotometer had two light sources: (1) a deuterium lamp covered the wavelength range from 190 to 340 nm, and (2) a halogen lamp covered the wavelength range from 340 to 1100 nm. The transmittance spectra were measured by a silicon photodiode detector at a scanning speed of 700 nm per minute and 1 nm per step. The FTIR was equipped with a ceramic filament light source, a KBr beam splitter, and a deuterated triglycine sulfate (DTGS) detector. The scanning parameters of the FTIR included 5 kHz scanning speed and 4 cm^{-1} resolution. Both the spectrophotometer and the FTIR had large aperture angles (3-5°).

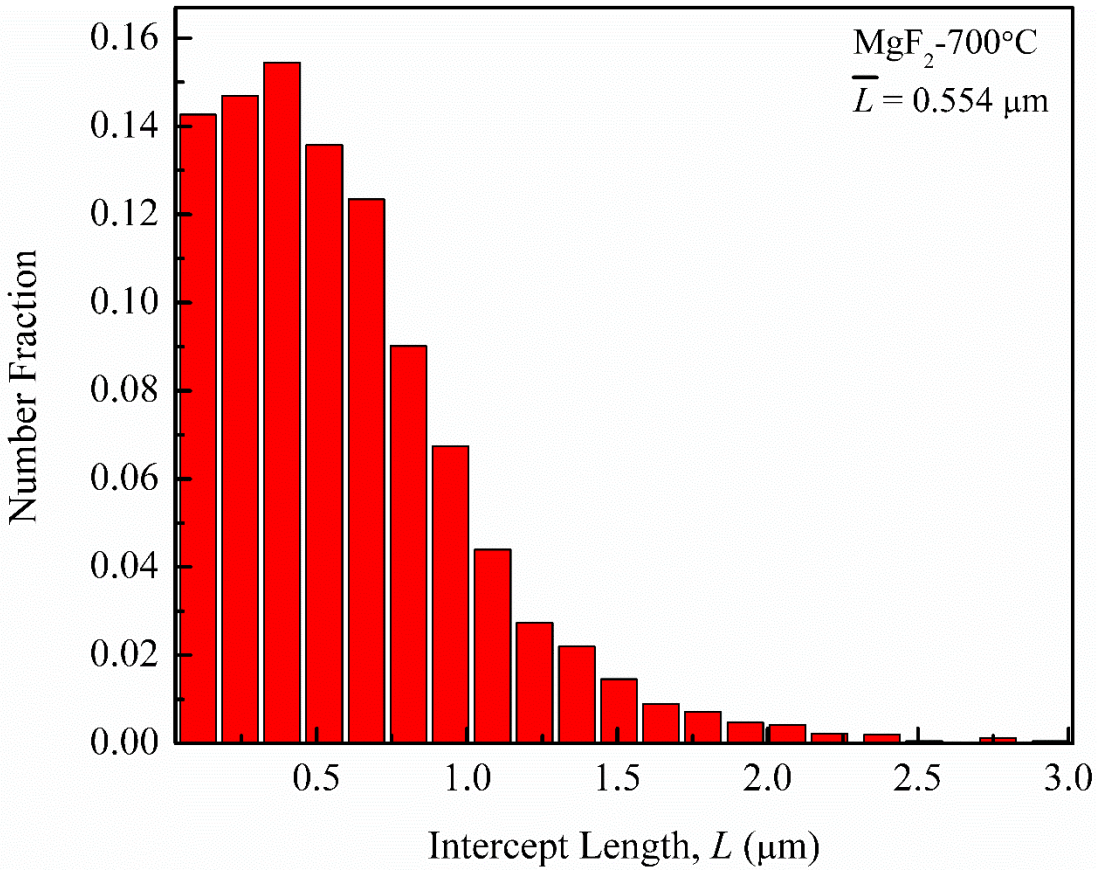

Figure 2.5 Histogram of grain intercept length for polycrystalline MgF_2 annealed at 700°C for 1 hour as measured by EBSD.

2.4 Experimental Results

2.4.1 Sizes and Orientations of Grains in Polycrystalline MgF_2

Figure 2.5 shows a representative histogram of the grain intercept length distribution for MgF_2 annealed at 700°C. The mean intercept length, $\overline{L}$, for this material was 0.554 μm. The calculation of the mean was based on measurements of intercept lengths on 4051 grain sections. The intercept length distribution was positively skewed on the linear plot, i.e., there was a long tail at long intercept lengths. The mean intercept length increased from 0.216 μm for the as hot-pressed MgF_2 to 1.376 μm for the MgF_2 annealed at 800°C (see Table 2.2). The intercept length distributions for the hot-pressed and the annealed materials were all similar in that they were all positively skewed.

Figure 2.6 shows a plot of the cumulative fraction of the grains, $F(\theta)$, as a function of the grain orientation angle, θ, for MgF_2 annealed at 700°C. The grain orientation was defined by the angle between the c-axis of a grain and the normal to the grain section. Grains oriented along the *c*-axis (θ = 0) were relatively few and are shown by the blue color in Figure 2.3. The line plotted in Figure 2.6 represents cumulative distribution of grains for isotropic random orientation as defined by the following equation:

$$F(\theta) = \int_0^{\theta} \frac{2\pi r \sin\theta r d\theta}{2\pi r^2} = \int_0^{\theta} \sin\theta d\theta = 1 - \cos\theta \qquad (2.15)$$

Eq. (2.15) is based on the idea that for random isotropic distribution of grain orientations the cumulative fraction of grains with orientations equal to and less than θ is the ratio of the surface area of a section of the sphere at an angle θ and the surface area of a hemisphere. It is noted in Figure 2.6 that grains in MgF_2 were randomly oriented and this was true for all materials including hot-pressed MgF_2. A mean grain orientation, $\overline{\theta}$, for the isotropic

Table 2.2 Mean grain intercept lengths, mean orientations and mean square deviations of refractive index for polycrystalline MgF_2.

Processing History	$\bar{L}$ (μm)	$\bar{\theta}$ (°)	$\overline{\Delta n^2}$ (x10^5)		
			0.633 μm	1.064 μm	3.39 μm
As Hot-Pressed #1	0.216	54.89	2.580	2.493	2.003
As Hot-Pressed #2	0.252	53.31	2.683	2.592	2.083
Annealed at 600°C	0.290	52.81	2.977	2.877	2.312
Annealed at 650°C	0.292	55.48	2.699	2.608	2.096
Annealed at 700°C	0.554	55.80	2.682	2.592	2.083
Annealed at 750°C	0.611	55.22	2.582	2.495	2.005
Annealed at 775°C	1.143	55.36	2.665	2.575	2.069
Annealed at 800°C	1.376	57.68	2.540	2.455	1.972
Average		55.07	2.676	2.586	2.078

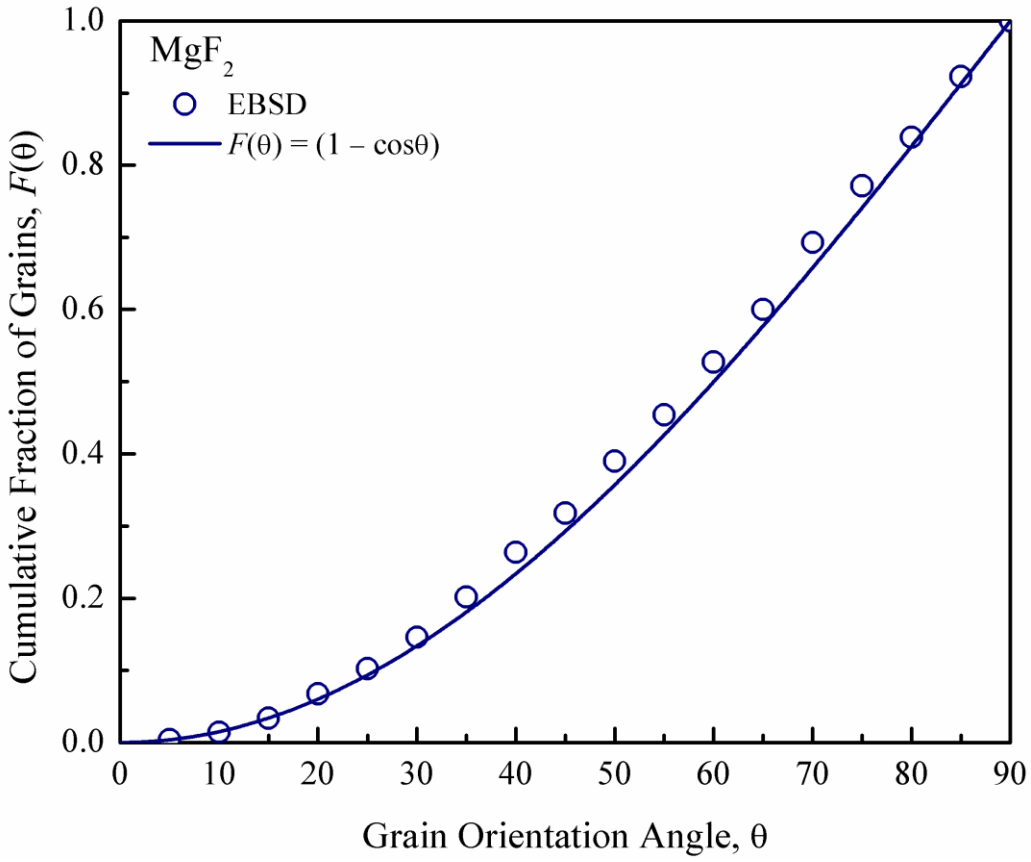

Figure 2.6 Cumulative distribution of grain orientations in MgF_2 annealed at 700°C for 1 hour measured by EBSD compared with isotropic random distribution.

random orientation was defined by the following equation:

$$\bar{\theta} = \int_0^{\pi/2} \theta f(\theta) d\theta = \int_0^{\pi/2} \theta \sin\theta d\theta = 1 \tag{2.16}$$

Thus, the mean grain orientation for an isotropic random distribution is 1 radian or 57.3°. The mean grain orientations measured using the EBSD software for the different MgF_2 materials are listed in Table 2.2. The values ranged from 52.8 to 57.7° with no discernible trend with grain size or annealing temperature. The average measured value for MgF_2 was 55.1°, close to the theoretical value. This is consistent with Figure 2.6.

The EBSD results were also used to define a mean square deviation of the refractive index, $\overline{\Delta n^2}$, using the following equation:

$$\overline{\Delta n^2} = \frac{1}{N} \sum_{i=1}^{N-1} [n(\theta_{i+1}) - n(\theta_i)]^2 \tag{2.17}$$

In Eq. (2.17), $n(\theta_i)$ is the refractive index of the i^{th} grain with an orientation θ_i along the path of light and $n(\theta_{i+1})$ is the refractive index of the $(i+1)^{th}$ grain with an orientation θ_{i+1}. Because of its tetragonal crystal structure MgF_2 is a uniaxial crystal and the refractive index in a crystallographic direction θ with respect to the *c*-axis is defined by the following equation [24]:

$$n(\theta) = \frac{n_e n_o}{\sqrt{(n_e^2 cos^2\theta + n_o^2 sin^2\theta)}} \tag{2.18}$$

In e Eq. (2.18), n_o is the refractive index in the ordinary direction (*c*-axis) and n_e is the refractive index in the extraordinary direction (normal to the *c*-axis). Values of n_o and n_e, measured on single-crystal MgF_2 and fitted to a three-term Sellmeier-type equation by Dodge [25], are listed in Table 2.1 and used in the calculations of $\overline{\Delta n^2}$ using Eq. (2.17) and

(2.18). Representative values for $\overline{\Delta n^2}$ at the three wavelengths corresponding to the three lasers are listed in Table 2.22. $\overline{\Delta n^2}$ decreased from 2.66 x 10^{-5} at a wavelength of $\lambda_0 = 0.633$ μm to 2.07 x 10^{-5} at $\lambda_0 = 3.39$ μm.

2.4.2 Effect of Grain Size on Transmittance and Scattering Coefficient

Figure 2.7 shows plots of the transmittance (I/I_0) versus mean grain size, $\overline{G}$, for the three wavelengths, 0.633, 1.064 and 3.39 μm. The lines through the data points are 'best fits' of the following equation:

$$\frac{I}{I_0} = \left[\frac{(1-R)^2 e^{-\alpha \bar{G}}}{1 - R^2 e^{-2\alpha \bar{G}}}\right] \tag{2.19}$$

To fit Eq. (2.19) to the data, the single-surface reflectance, R, was calculated from Eq. (2.2) using the following average refractive index for a polycrystalline material with isotropic randomly oriented grains:

$$\bar{n} = \int_0^{\pi/2} n(\theta) \sin\theta d\theta \tag{2.20}$$

α, a material-characteristic parameter that is dependent on wavelength, but independent of grain size, was estimated by nonlinear regression analysis. α is related to the scattering coefficient, γ, via the following equation:

$$\alpha = \frac{\gamma t}{\bar{G}} \tag{2.21}$$

Equation (2.21) fits the variation of transmittance with grain size reasonably well for all the three wavelengths. This is equivalent to a linear variation of the scattering coefficient, γ, with the mean grain size, $\overline{G_N}$. To illustrate this, scattering coefficients were calculated directly from transmittance, $T = (I/I_0)$, at different grain sizes and wavelengths

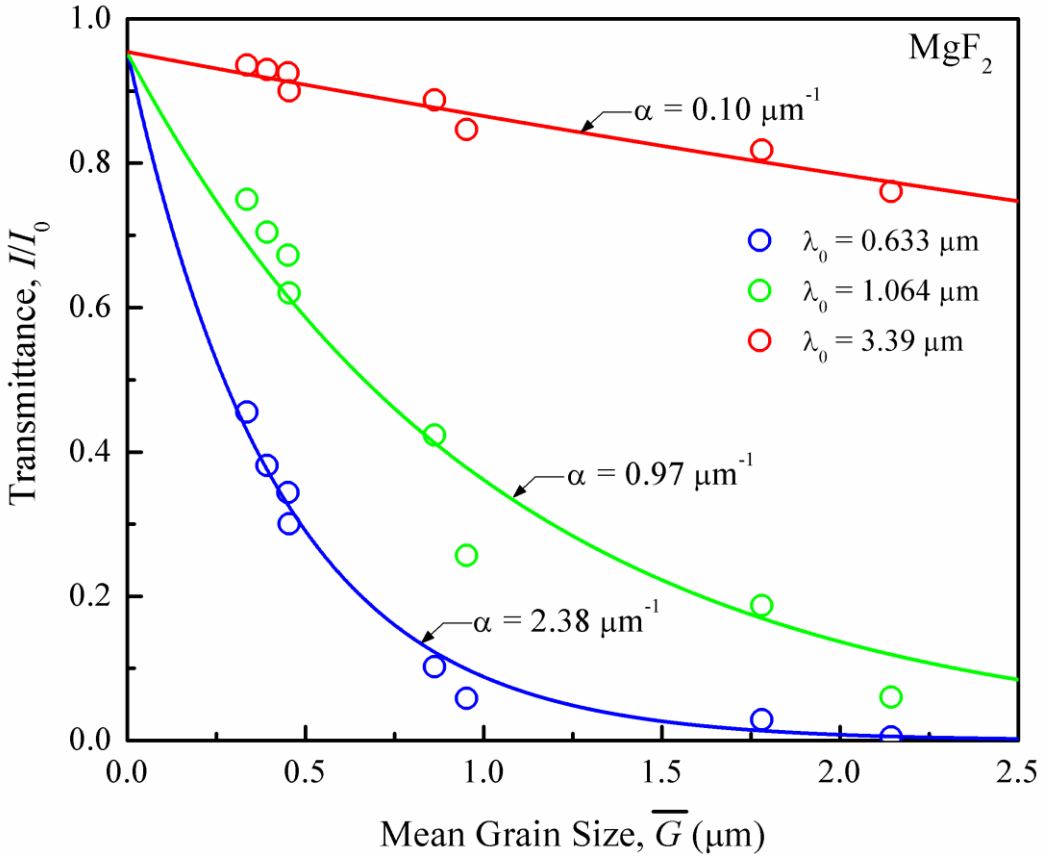

Figure 2.7 Variations of transmittance of polycrystalline MgF2 with mean grain size at three different wavelengths.

of light using the following equation derived from Eq. (2.1):

$$\gamma = \frac{1}{t} ln \left[\frac{(1-R)^2}{2T} + \sqrt{R^2 + \frac{(1-R)^4}{4T^2}} \right] \tag{2.22}$$

Figure 2.8 shows plots of γ versus $\bar{G}$ at the three wavelengths of light. The plots are linear. This confirms the self-consistency of Figure 2.7 and Figure 2.8.

2.4.3 Effect of Light Wavelength on Scattering Coefficient

In addition to the particle or grain-size dependence, the dependence of the scattering coefficient on the wavelength of light is a key to understanding and establishing the mechanism of scattering in birefringent polycrystalline materials. Both the RGD theory (Eq. (2.8)) and the theory of Raman and Viswanathan (Eq. (2.11)) predict a direct inverse square dependence of γ on λ_0 with a weak dependence of $\overline{\Delta n^2}$ on λ_0. To test this dependence, $[\alpha/(t\overline{\Delta n^2})] = [\gamma/(\bar{G}\overline{\Delta n^2})]$ was plotted as a function of λ_0. Figure 2.9 shows such a plot for polycrystalline MgF_2. The line fitted through the data points is a plot of the following equation:

$$\frac{\alpha}{t\overline{\Delta n^2}} = \frac{\gamma}{\bar{G}\overline{\Delta n^2}} = \frac{\Omega}{\lambda_0^2} \tag{2.23}$$

It is evident from Figure 2.9 that Eq. (2.23) gives good fit to the data. The measured scattering coefficient varies inversely with the square of the wavelength of light.

2.5 Discussion

The analyses of the experimental data reported in the previous section established that the scattering coefficient in polycrystalline MgF_2 scales linearly with the mean grain size, $\overline{G}$, and inversely with the square of the wavelength of light, λ_0. These trends are,

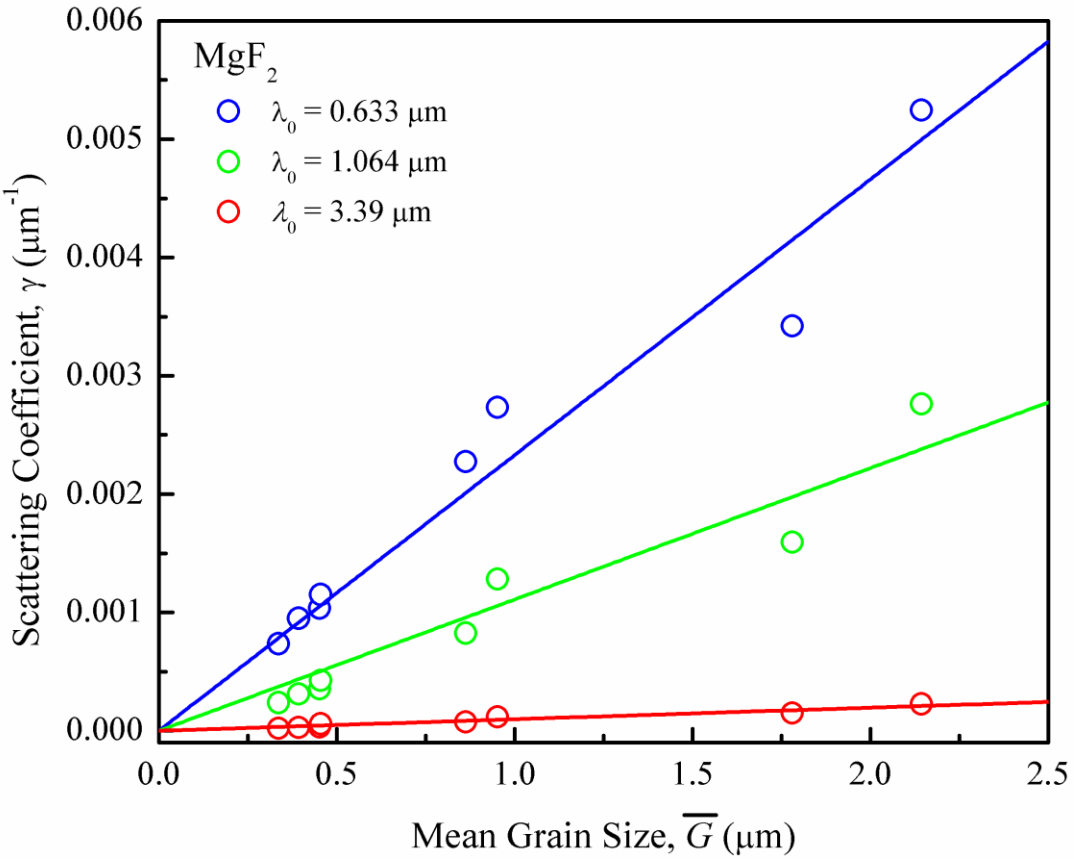

Figure 2.8 Variations of the scattering coefficient of polycrystalline MgF_2 with mean grain size at three different wavelengths.

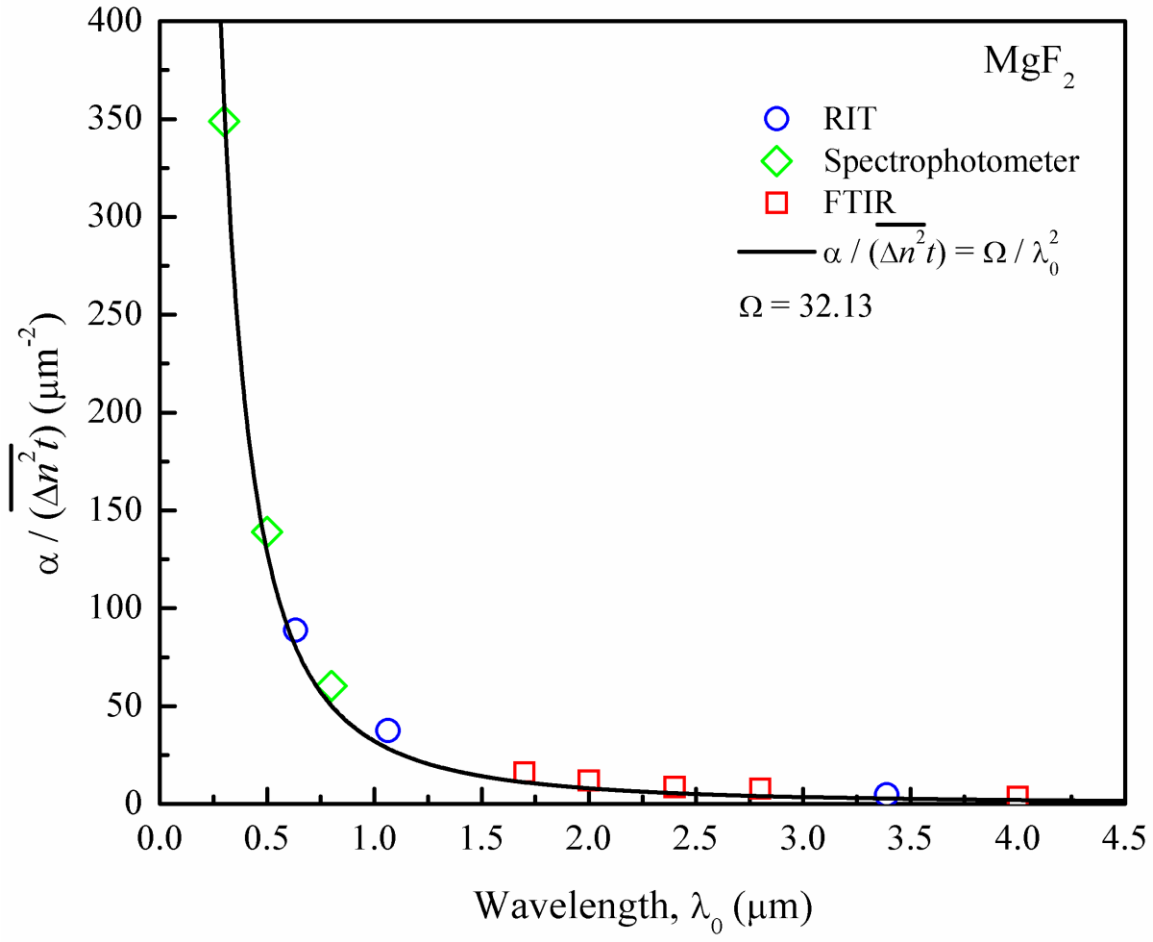

Figure 2.9 Variation of grain size normalized scattering coefficient of polycrystalline MgF_2 with wavelength of light.

however, consistent with both the RGD theory (Eq. (2.8)) and the theory of Raman and Viswanathan (Eq. (2.11)) and they do not help discriminate the two theories. Therefore, the transmittance measured for different grain sizes of MgF_2 were quantitatively compared with the theoretical predictions. Figure 2.10 shows this comparison at the wavelength of $\lambda_0 = 0.633$ μm. In the figure, both the experimental data and the theoretical predictions are shown in terms of the following common equation:

$$\frac{I}{I_0} = \left[\frac{0.9486e^{-\alpha\bar{G}}}{1 - 0.0006778e^{-2\alpha\bar{G}}}\right] \tag{2.24}$$

The numerical factor, 0.9486, is $(1–R)^2$, where the single-surface reflectance, R, was calculated using Eq. (2.2) and an average polycrystalline refractive index, $\bar{n} = 1.3848$, for MgF_2 at $\lambda_0 = 0.633$ μm. The numerical factor, 0.0006778, is the value of R^2. A value, $\alpha = \alpha_{exp} = 2.38$ μm^{-1}, gave the 'best fit' to the experimental data (blue line in Figure 2.10). For the RGD theory, $\alpha = \alpha_{RGD} = 1.98$ μm^{-1} was calculated from Eq. (2.8) and Eq. (2.21) using $\phi = 1$, $d_p = \bar{G}$, $t = 1000$ μm, and $\Delta n^2 = \overline{\Delta n^2} = 0.00002676$, as measured by EBSD at wavelength, $\lambda_0 = 0.633$ μm (Table 2.2). The red solid line in Figure 2.10 corresponds to a plot of Eq. (2.24) with $\alpha = \alpha_{RGD} = 1.98$ μm^{-1}. The RGD theory slightly underestimates the effect of grain size on transmittance in polycrystalline MgF_2.

Application of the Raman and Viswanathan theory (Eq. (2.11)) to polycrystalline MgF_2 is more challenging because of their assumptions with respect to the grain shape and the grain orientations. They assumed a polycrystalline material to be made of uniform cube-shaped grains with the cube edges aligned along the three principal optical axes, 1, 2 and 3 with the refractive indices, n_1, n_2 and n_3. One set of grain edges are parallel to the incident light. A random orientation in this context implies that the probabilities of the

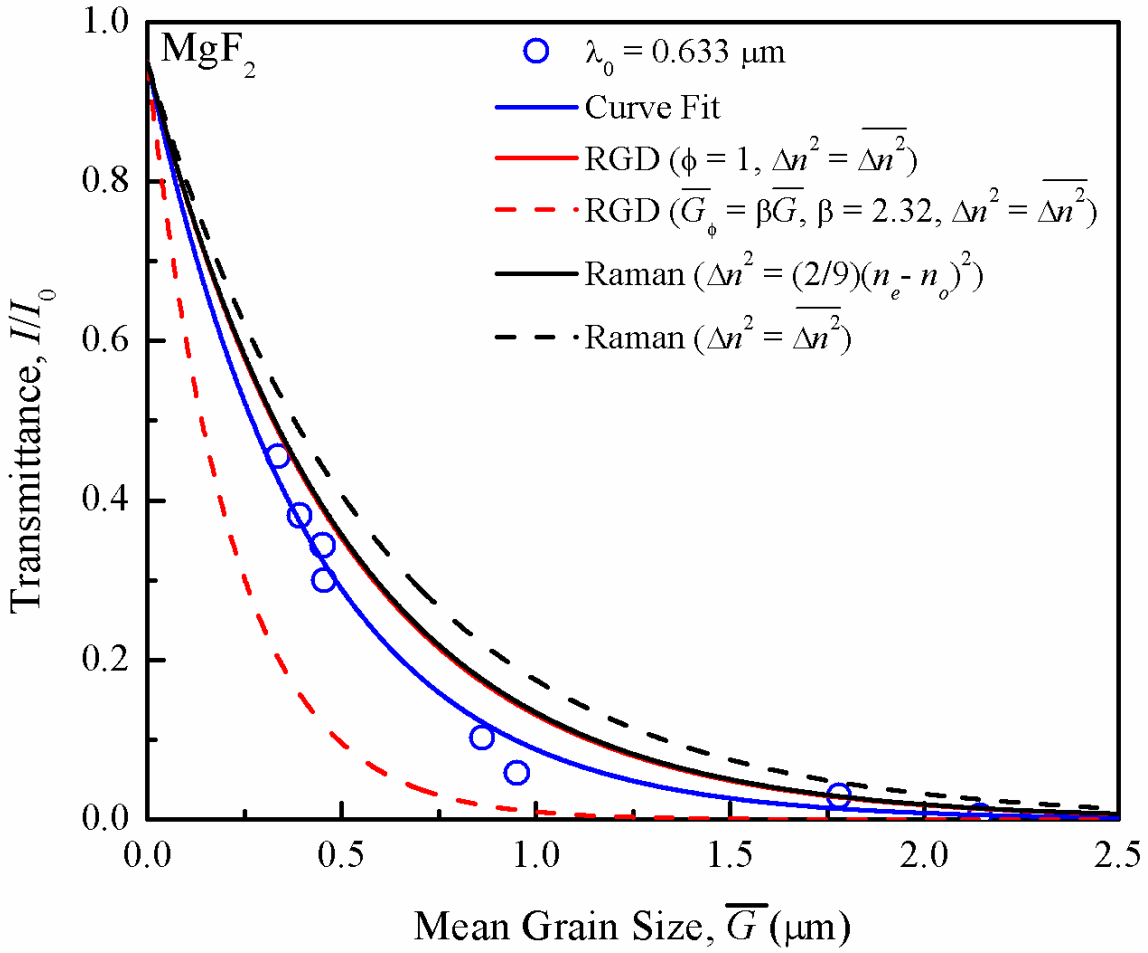

Figure 2.10 Transmittance of polycrystalline MgF_2 as a function of grain size compared with theoretical predictions.

three optical axes being aligned in the direction of the incident light are equal. Therefore, in Eq. (2.11), $p_1 = p_2 = p_3 = 1/3$, and $n_1 = n_o$, and $n_2 = n_3 = n_e$ for MgF_2, a uniaxial crystal.

With these assumptions, we get $\sum p_2 p_3 (n_2 - n_3)^2 = \frac{2}{9}(n_e - n_o)^2 =$ 0.00003094. Note that this value is greater than the average value measured by EBSD and used in the RGD model. The parameter, Δ, in the theory of Raman and Viswanathan [15] is both the edge length of the cube-shaped grains as well as the path length of the light in each grain. For a polycrystalline material with grains of polyhedral shape and a distribution of grain sizes, there is some uncertainty in choosing a value for Δ. It is argued here that Δ should be the mean path length of light in a grain because it is the path length in a grain in combination with the refractive index in a particular crystal direction that determines the light retardation in Raman and Viswanathan theory. Therefore, $\Delta = \bar{L} = \frac{\bar{G}}{1.558}$. Equation (2.11), then, yields $\alpha_{Raman} = 1.96\ \mu m^{-1}$. This is nearly identical to the value predicted by the RGD theory. The plot corresponding to this value of α is shown by the solid black line in Figure 2.9. This line overlaps the line corresponding to the RGD theory ($\alpha = 1.98\ \mu m^{-1}$, red line).

The assumptions of cube-shaped grains and the grains being oriented only in the directions of the principal optical axes are too restrictive and not representative of polycrystalline MgF_2. A modification of the Raman and Viswanathan theory [15] for truly isotropic random orientation of grains with a polyhedral shape and a distribution of grain sizes is nontrivial and beyond the scope of this study. It is reasonable to argue, however, that $\overline{\Delta n^2}$ measured by EBSD represents an average value of $\sum_{i=1}^{N} p_i p_{i+1} (n_{i+1} - n_i)^2$ for MgF_2,

and this N term sum should replace the three-term sum in Eq. (2.11). This approach gives $\alpha_{Raman} = 1.69\ \mu m^{-1}$ and the corresponding prediction (dashed black line in Figure 2.9) is slightly above the other theoretical predictions.

It is clear from the above discussion that it is difficult to discriminate between the RGD theory and the Raman and Viswanathan theory by comparing the measured and the theoretical predictions of the variation of transmittance with the mean grain size of a birefringent polycrystalline ceramic. The theories make assumptions that are not realistic for real polycrystalline ceramics. These assumptions with respect to the grain shape and the grain orientations in the Raman and Viswanathan theory [15] were noted above. Their theory also makes the assumption that polarization of light does not change as the light propagates from grain to grain, an assumption strictly not valid for anisotropic crystals.

There are also important assumptions made in employing the RGD theory to explain the effect of birefringence on transmittance of polycrystalline ceramics. The formulation of the scattering coefficient, γ, from the single-particle scattering efficiency, K, as represented in Eq. (2.6), is based on two assumptions: (1) particles in a medium scatter light independently, and (2) each particle causes only single scattering [20]. Clearly, these assumptions are valid only for two-phase systems with a low concentration of the dispersed phase. van de Hulst [20] suggests that a mutual distance of 3 times the radius is a sufficient condition for independent scattering. This interparticle spacing is equivalent to a volume fraction of 0.0335. Secondly, according to van de Hulst [20], single scattering prevails if $\gamma t < 0.1$. For polycrystalline MgF_2, $\phi \approx 1$ and γt varied from 0.74 to 5.25 with grain size for $\lambda_0 = 0.633\ \mu m$. Only for $\lambda_0 = 3.39\ \mu m$ and $\overline{G} \leq 0.86\ \mu m$, γt was less than 0.1. Strictly speaking, therefore, RGD theory should not be applicable to polycrystalline MgF_2. And

yet, the Apetz and van Bruggen model based on the RGD theory gives a reasonable prediction of the effects of birefringence and grain size on the light transmittance of MgF_2. To resolve this dichotomy, transmittance measurements are being made on a model two-phase system, monodispersed silica spheres in a solution of water in glycerol, where the mismatch of the refractive indices is comparable to the average birefringence in polycrystalline MgF_2. The objective of this study is to establish the range of silica volume fraction where the RGD theory is applicable. These results will be presented in Chapter 3.

We note here in closing that the average grain size, $\overline{G}$, defined in this study is based on an arithmetic number average intercept length, $\overline{L}$. In reality, the intercept length and the grain size are both distributed, as shown by the example of Figure 2.5. What is the effect of this grain-size distribution on grain-boundary scattering? To answer this question, we note that the RGD equation for the scattering coefficient, Eq. (2.6), which is valid for monodisperse particles, now takes the following form for polydisperse systems:

$$\gamma = \frac{3\pi^2 \Delta n^2 \sum_{i=1}^{i=N} \phi_i d_i}{\lambda_0^2} \tag{2.25}$$

In Eq. (2.25), ϕ_i is the volume fraction of particles in a size interval with the midpoint size, d_i, and N is the total number of grain size intervals. The summation in Eq. (25) can, in fact, be identified as a volume fraction weighted average grain size:

$$\overline{G_\phi} = \sum_{i=1}^{i=N} \phi_i d_i = \frac{\sum_{i=1}^{i=N} n_i d_i^4}{\sum_{i=1}^{i=N} n_i d_i^3} \tag{2.26}$$

In Eq. (2.26), n_i is the number of grains (particles) in a size interval centered at d_i. Calculations of $\overline{G_\phi}$ for polycrystalline MgF_2 from EBSD data revealed that $\overline{G}_\varphi = \beta\overline{G}$, where the factor β accounts for the effect of the grain-size distribution on grain-boundary

scattering. For MgF_2 heat-treated at different temperatures, β ranged from 1.89 to 2.76 with an average value of 2.32 (see Table 2.3). In other words, the scattering coefficient predicted by the RGD theory is, on an average, 2.32 times greater than the one based on the number average grain size, $\overline{G}$. The theoretical prediction based on this grain-size distribution corrected RGD scattering theory is shown by the dashed red line in Figure 2.10. The grain-size distribution has a significant effect on the RGD theory prediction. The predicted transmittance is significantly below the measured values. It is interesting to note here that the predictions of the light retardation models are not as sensitive to grain-size distribution because there is no explicit dependence of the scattering coefficient on volume fractions of grains or particles.

2.6 Conclusions

1. The scattering coefficient of polycrystalline MgF_2 scales linearly with grain size and inversely with the square of the wavelength of light.
2. The observed trends of the scattering coefficient with grain size and wavelength of light are consistent with both the Apetz and van Bruggen model based on the RGD theory of particle light scattering as well as the light retardation theory of Raman and Viswanathan.
3. The theoretical predictions of the transmittance in birefringent polycrystalline ceramics are subject to considerable uncertainty due to the uncertain values of the material parameters that appear in the theoretical equations.
4. Transmittance predicted by particle-scattering models, in particular, is strongly affected by grain-size distribution in addition to the average grain-size effect.

Table 2.3 Number average grain size ($\bar{G}$), standard deviation of mean grain size, volume fraction weighted average grain size ($\overline{G_\phi}$) and beta (β) for polycrystalline MgF_2.

	$\bar{G}$ (μm)	S.D. (μm)	$\overline{G_\phi}$ (μm)	β
As Hot-Pressed #1	0.337	0.265	0.802	2.384
As Hot-Pressed #2	0.393	0.258	0.807	2.055
Annealed at 600°C	0.452	0.264	0.853	1.889
Annealed at 650°C	0.455	0.273	0.899	1.976
Annealed at 700°C	0.863	0.637	2.306	2.672
Annealed at 750°C	0.952	0.824	2.626	2.759
Annealed at 775°C	1.781	1.505	4.583	2.574
Annealed at 800°C	2.144	1.571	4.806	2.242

2.7 References

[1] D. C. Harris, *Materials for Infrared Windows and Domes: Properties and Performance*. SPIE Optical Engineering Press, Bellingham, WA, 1999.

[2] J. G. J. Peelen and R. Metselaar, "Light Scattering by Pores in Polycrystalline Materials: Transmission Properties of Alumina," *J. Appl. Phys.,* **45** [1] 216-20 (1974).

[3] J. Schroeder and J. H. Rosolowski, "Light Scattering in Polycrystalline Materials," pp. 156-68. in *Emerging Optical Materials,* Vol. 297. Edited by S. Musikant. SPIE: International Society for Optics and Photonics, 1982.

[4] G. H. Beall and L. R. Pinckney, "Nanophase Glass-Ceramics," *J. Am. Ceram. Soc.,* **82** [1] 5-16 (1999).

[5] H. E. Bennett and J. O. Porteus, "Relation Between Surface Roughness and Specular Reflectance at Normal Incidence," *J. Opt. Soc. Am.,* **51** [2] 123-29 (1961).

[6] A. Krell, J. Klimke and T. Hutzler, "Transparent Compact Ceramics: Inherent Physical Issues," *Opt. Mater.,* **31** 44-50 (2009).

[7] W.-Y. Lin, M.-H. Hon and S.-J. Yang, "Effect of Grain Growth on Hot-Pressed Optical Magnesium Fluoride Ceramics," *J. Am. Ceram. Soc.,* **71** [3] C-136 - C-37 (1988).

[8] C.-S. Chang, M.-H. Hon and S.-J. Yang, "Effect of Grain Growth of Hot-Pressed Magnesium Fluoride on Optical Transmittance," *Jpn. J. Appl. Phys.,* **30** [3] 506-10 (1991).

[9] T.-C. Wen and D. K. Shetty, "Birefringence and Grain-Size Effects on Optical Transmittance of Polycrystalline Magnesium Fluoride," pp. 73020Z-1 - 20Z-6. in *Window and Dome Technologies and Materials XI,* Vol. 7302. Window and Dome Technologies and Materials. Edited by R. W. Tustison. SPIE: International Society for Optics and Photonics, Orlando, FL, 2009.

[10] A. Krell, P. Blank, H. Ma, T. Hutzler, M. P. B. v. Bruggen and R. Apetz, "Transparent Sintered Corundum with High Hardness and Strength," *J. Am. Ceram. Soc.,* **86** [1] 12-18 (2003).

[11] R. Apetz and M. P. B. v. Bruggen, "Transparent Alumina: A Light-Scattering Model," *J. Am. Ceram. Soc.,* **86** [3] 480-86 (2003).

[12] G. Bernard-Granger and C. Guizard, "Influence of Co-Doping on the Sintering Path and on the Optical Properties of a Submicronic Alumina Material," *J. Am. Ceram. Soc.,* **91** [5] 1703-06 (2008).

[13] I. Yamashita, H. Nagayama and K. Tsukuma, "Transmission Properties of Translucent Polycrystalline Alumina," *J. Am. Ceram. Soc.,* **91** [8] 2611-16 (2008).

[14] A. Krell, J. Klimke and T. Hutzler, "Advanced Spinel and Sub-μm Al_2O_3 for Transparent Armour Applications," *J. Eur. Ceram. Soc.,* **29** 275-91 (2009).

[15] C. V. Raman and K. S. Viswanathan, "The Theory of the Propagation of Light in Polycrystalline Media," *Proc. Indian Acad. Sci. A,* **41** 37-43 (1955).

[16] G. S. Ranganath and S. Ramaseshan, "Optical transmission in polycrystals," *Optica Acta,* **19** [9] 781-90 (1972).

[17] H. M. Kahan, D. P. Stubbs and R. V. Jones, "The Potentialities of Fine Grained Ceramics for Optical and Acoustical Applications," pp. 185-203. in *Optical and Acoustical Micro-Electronics*, New York, NY, 1974.

[18] G. Mie, "Contributions on the Optics of Turbid Media - Particularly Colloidal Metal Solutions," *Ann. Phys.,* **330** [3] 377-445 (1908).

[19] B. Michel, MieCalc-Freely Configurable program for Light Scattering Calculations (Mie Theory), http://www.lightscattering.de/MieCalc/eindex.html, (accessed 13 May 2014).

[20] H. C. van de Hulst, *Light Scattering by Small Particles*. Dover Publications, Inc., New York, 1981.

[21] B. L. Adams, S. I. Wright and K. Kunze, "Orientation Imaging: The Emergence of a New Microscopy," *Metall. Trans. A,* **24A** [4] 819-31 (1993).

[22] F. J. Humphreys, "Review: Grain and Subgrain Characterization by Electron Backscatter Diffraction," *J. Mater. Sci.,* **36** 3833-54 (2001).

[23] M. I. Mendelson, "Average Grain Size in Polycrystalline Ceramics," *J. Am. Ceram. Soc.,* **52** [8] 443-46 (1969).

[24] A. Yariv and P. Yeh, *Optical Waves in Crystals: Propagation and Control of Laser Radiation*. John Wiley & Sons, New York, NY (1984).

[25] M. J. Dodge, "Refractive Properties of Magnesium Fluoride," *Appl. Opt.,* **23** [12] 1980-85 (1984).

CHAPTER 3

AN ASSESSMENT OF THE APPLICABILITY OF PARTICLE LIGHT SCATTERING THEORIES TO BIREFRINGENT POLYCRYSTALLINE CERAMICS

3.1 Introduction

Light transmittance of birefringent polycrystalline ceramics decreases with increasing grain size. Figure 3.1 illustrates this phenomenon with a comparison of the optical transmittance of two birefringent ceramics, magnesium fluoride (MgF_2, tetragonal) and alumina (Al_2O_3, hexagonal close-packed) with that of a nonbirefringent cubic ceramic, spinel ($MgAl_2O_4$). The decrease in transmittance with grain size is most pronounced in MgF_2. Al_2O_3 exhibits intermediate behavior, while the transmittance of $MgAl_2O_4$ is nearly insensitive to its grain size. The refractive indices in the ordinary (n_o) and the extraordinary (n_e) directions for MgF_2 and Al_2O_3 and the isotropic refractive index of $MgAl_2O_4$, calculated using the dispersion equations tabulated by Harris [1], are listed in Table 3.1. It is evident from Table 3.1 and Figure 3.1 that the decrease of the transmittance of polycrystalline ceramics with increasing grain size is greater with increasing value of $\Delta n_{max} = |n_e - n_o|$, a measure of the birefringence.

Two different theoretical approaches have been proposed to explain the grain-size effect on light transmittance in birefringent polycrystalline ceramics. One approach, characterized here as wave propagation in random media, was initially proposed by Debye and Bueche [2], and, subsequently, employed by others in various forms [3-6]. This

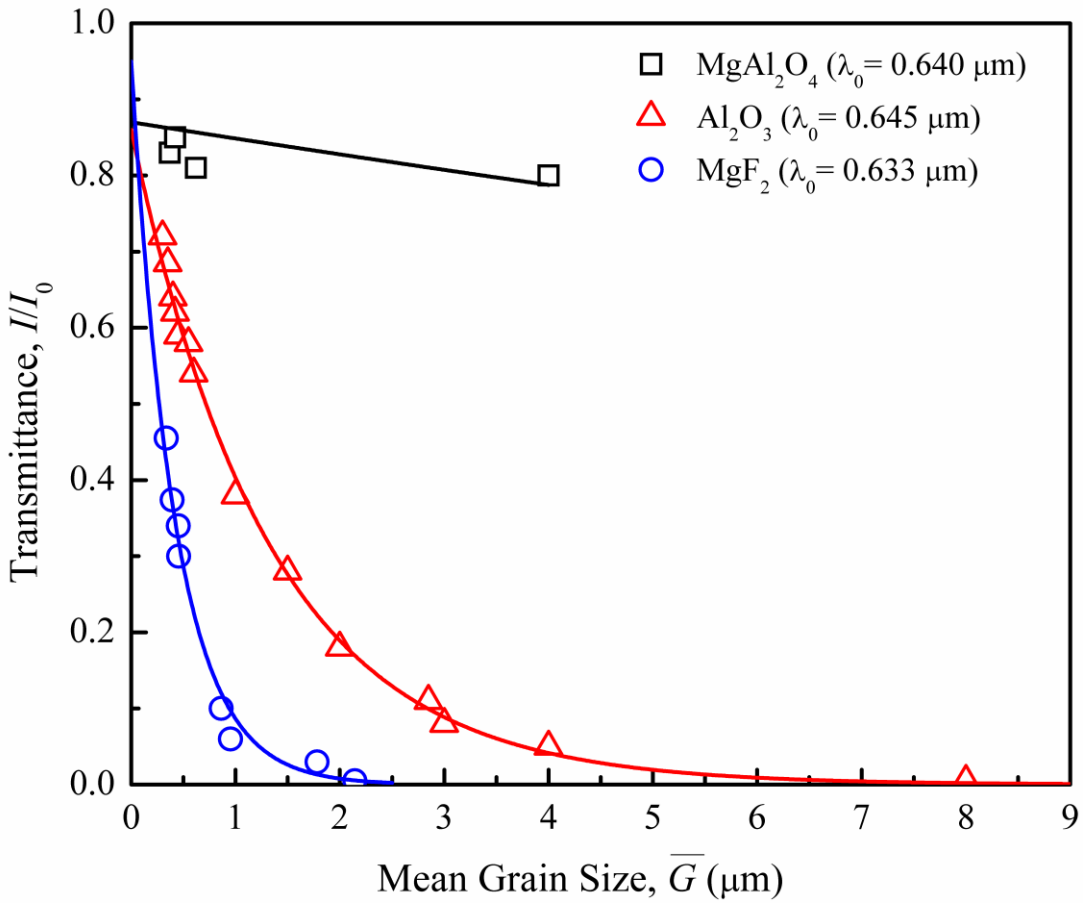

Figure 3.1 Variations of the transmittance of polycrystalline $MgAl_2O_4$, Al_2O_3 and MgF_2 as functions of the grain size at the indicated wavelengths (birefringence for Al_2O_3 and MgF_2 are listed in Table 3.1).

Table 3.1 The isotropic refractive index of $MgAl_2O_4$ and the refractive indices in the ordinary (n_o) and the extraordinary (n_e) directions for Al_2O_3 and MgF_2 at different wavelengths (From Harris [1]).

Material	λ_0 (μm)	n_o	n_e	$\lvert\Delta n_{max}\rvert$
$MgAl_2O_4$	0.640	1.7134	1.7134	0
Al_2O_3	0.645	1.7653	1.7573	0.008
MgF_2	0.633	1.3770	1.3888	0.0118

approach treats the effect of a random distribution of refractive index along the path of light on its intensity using wave-mechanics formulations. A second approach, due to Harrison [7] and Apetz and van Bruggen [8], treats a birefringent polycrystalline ceramic as a two-phase composite of isotropic spherical particles of diameter, d_p, and refractive index, n_p, dispersed in a homogenous matrix of refractive index, n_m. They employed an approximate form of the Raleigh-Gans-Debye (RGD) theory [9] of light scattering by spherical particles to formulate the scattering coefficient of a polycrystalline material.

Wen and Shetty [10] recently reviewed the two theoretical approaches for application to polycrystalline MgF_2. They showed that the scattering coefficient, γ, predicted by both theories can be represented in the following form:

$$\gamma = \frac{\Omega \phi d \overline{\Delta n^2}}{\lambda_0^2} \tag{3.1}$$

In Eq. (3.1), Ω is a nondimensional constant that takes different values in different theoretical models depending on the assumptions, ϕ is the volume fraction of the mono-dispersed spherical particles in the particle light scattering models, and $\phi = 1$ in models based on wave propagation in random media, $d = d_p$, diameter of the spherical particles for particle scattering models, while d is the mean path length in a grain in the direction of light propagation in the wave propagation models, $\overline{\Delta n^2}$ is the mean square deviation of the refractive index as light propagates from grain to grain, or from phase to phase, and λ_0 is the wavelength of light in vacuum. The scattering coefficient calculated from the measured in-line transmittance of polycrystalline MgF_2 varied linearly with the mean grain size and inversely with the square of the wavelength of light in agreement with Eq. (3.1). However, the theoretical models predict wide ranging values of the scattering coefficient due to

varying values of Ω depending on the assumptions made with respect to grain shape, size distribution, and orientation distribution, and choices of the parameters, ϕ, d and $\overline{\Delta n^2}$. Thus, a clear choice between the two theoretical approaches for application to polycrystalline MgF_2 was not possible.

In the present paper, the applicability of particle scattering theories, in general, and the RGD theory in particular, to birefringent polycrystalline ceramics is examined via measurements of the in-line transmittance and calculations of the scattering coefficients for a model two-phase system, silica microspheres dispersed in a glycerol and water solution. The model system was designed to simulate the birefringence of MgF_2. The primary objective of the study was to establish the range of volume fraction of silica microspheres in the suspensions where RGD theory adequately describes light transmission for particle sizes comparable to grain sizes and refractive index mismatch comparable to the average birefringence in MgF_2. This is intended to answer the question of the applicability of RGD theory to a high particle volume fraction system such as a polycrystalline ceramic. A secondary objective was to establish the appropriate average particle or grain size that must be used in analyzing light transmission using particle light scattering theories.

3.2 Materials and Experimental Procedures

3.2.1 Constituents of the Model System

The model system consisted of silica microspheres dispersed in a solution of glycerol and water. Silica microspheres of three different diameters, 0.5, 1.0 and 1.5 μm, were purchased from a vendor (silicon (IV) oxide, 99.9% pure, Alfa Aesar, Ward Hill, MA, USA). These particle sizes are in the range of grain sizes studied in MgF_2 (see Figure 3.2)

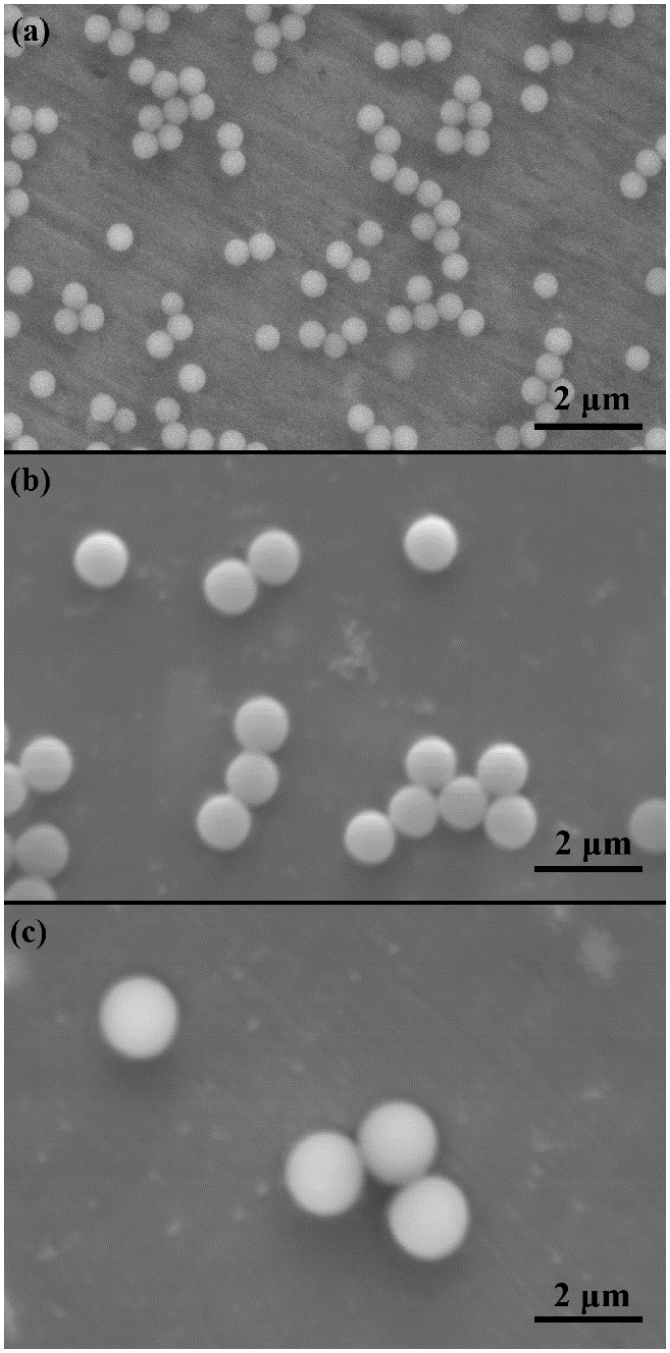

Figure 3.2 SEM images of silica microspheres: (a) d_p = 0.5 μm, (b) d_p = 1 μm, and (c) d_p = 1.5 μm.

[10]. The silica microspheres were made by a sol-gel process [11] and were uniform in size (see Figure 3.2). A solution of glycerol ($C_3H_5(OH)_3$, 99.5%, Mallinckrodt Baker, Inc., Phillipsburg, NJ, USA) and deionized water was used as the suspending medium. Glycerol and water were selected because they are completely miscible in each other and the refractive index of glycerol is greater than and the refractive index of water is less than the refractive index of the silica microspheres. Thus, a desired refractive index mismatch between the silica microspheres (n_p) and the suspending medium (n_m) could be designed by mixing glycerol and water.

3.2.2 Measurements of Refractive Indices

The refractive indices of glycerol, water and their solutions were measured using an Abbe refractometer (ABBE-3L, Bausch & Lomb, Rochester, NY, USA) at a wavelength of 0.589 μm. The refractive index of the silica microspheres was measured by the index-matching method [12, 13]. In this method, the in-line transmittance of a series of suspensions of silica spheres of the same size and volume fraction in solutions with varying glycerol and water contents, and, therefore, varying refractive index, were measured. The refractive index of the solution that produced the highest transmittance is the refractive index of the silica microspheres.

3.2.3 Measurements of In-Line Transmittance

In-line transmittance of suspensions was measured with a spectrophotometer (Lambda 950 UV/VIS/NIR, Perkin Elmer, Waltham, MA, USA). The measurements were made in the wavelength range, 0.55-0.65 μm, using a tungsten light source. The transmitted light intensity was measured with a photomultiplier tube detector. The suspension was

contained in a quartz cell with an internal light path length of 1 mm, the same as the thickness of the MgF_2 specimens [10]. A solution of glycerol and water of the selected composition was used as a reference for incident light intensity, I_0. Thus, any additional attenuation of light due to the presence of the silica particles could be attributed to only particle scattering.

3.3 Experimental Results and Analyses

3.3.1 Refractive Indices of Glycerol-Water Solutions

Figure 3.3 shows a plot of the refractive index of glycerol-water solution as a function of the weight fraction of glycerol. The measured values of the refractive index of pure water (n_w = 1.333), 99.5 w% glycerol (n_g = 1.472) and of the solutions are in agreement with data reported in the literature [14]. The following second-order polynomial fitted the measured data adequately for purposes of interpolation:

$$n_m = 1.333 + 0.10116w_g + 0.03804w_g^2 \qquad (3.2)$$

In Eq. (3.2), n_m is the refractive index of the water-glycerol solution, and w_g is the weight fraction of glycerol in the solution.

3.3.2 Refractive Index of Silica Microspheres

Figure 3.4 shows plots of transmittance of the suspensions of silica microspheres in water-glycerol solutions for a fixed volume fraction of silica, ϕ = 0.01, as functions of he refractive index of the solution, n_m, varied by varying the weight fraction of glycerol. The refractive indices of the solutions were obtained from Eq. (2) using the weight fractions of glycerol. For all three diameters of the silica particles, the transmittance was highest for n_m = 1.441. This value was taken as the refractive index of the silica microspheres (n_p). It

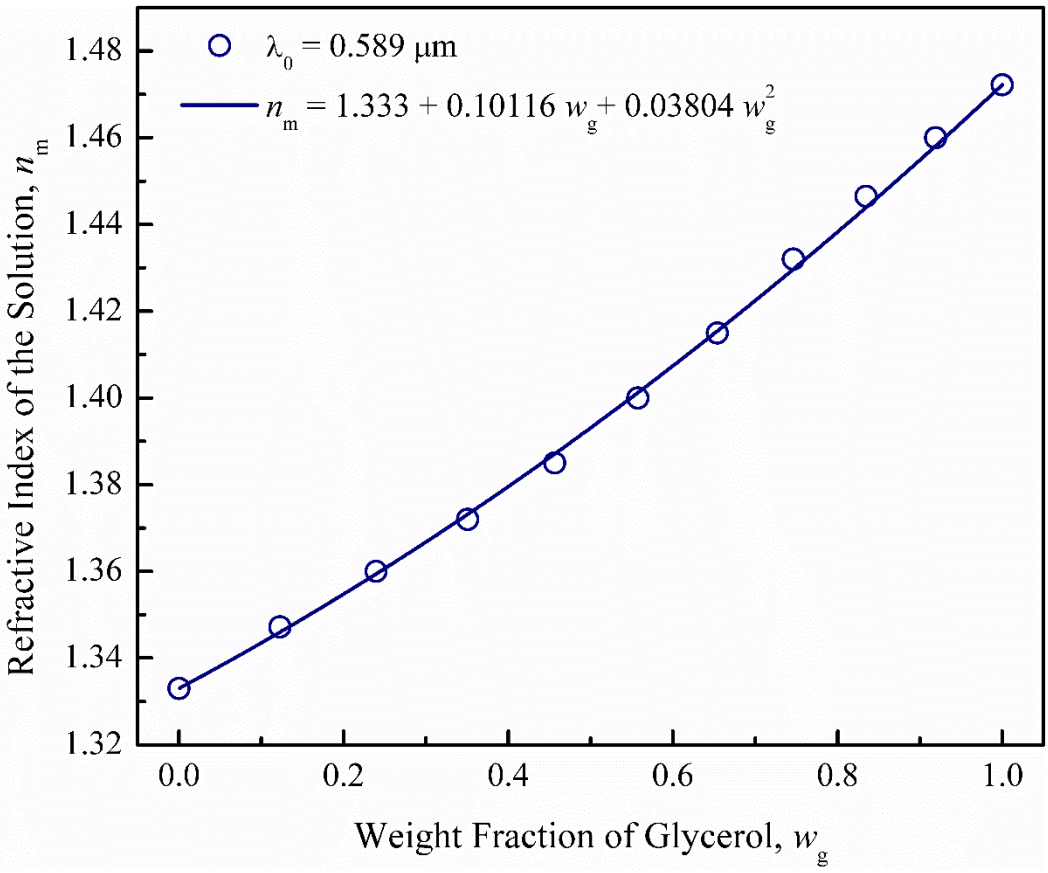

Figure 3.3 Variation of the refractive index of water-glycerol solution as a function of the weight fraction of glycerol in the solution.

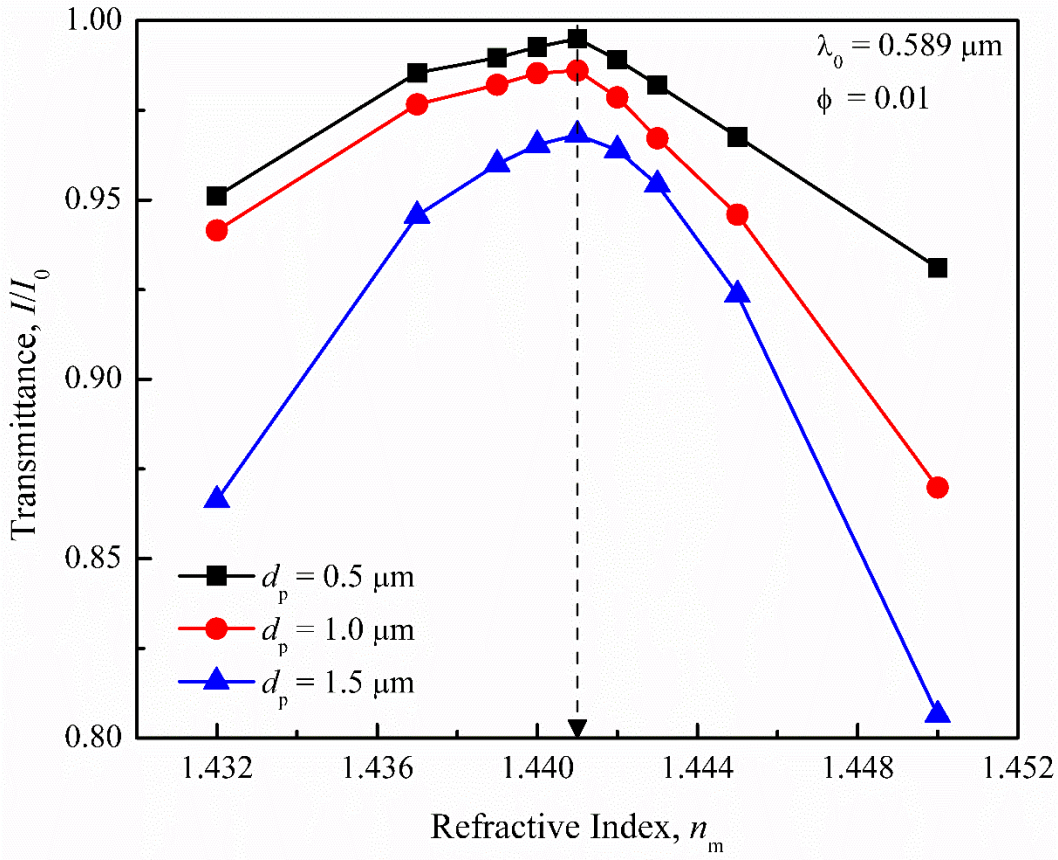

Figure 3.4 Variations of the transmittance of silica suspensions in water-glycerol solutions with varying refractive index.

should be noted that this value is less than the value, $n = 1.458$, one would calculate for $\lambda_0 = 0.589$ μm using the dispersion equation for fused silica [15]. This is because the silica microspheres were made by the sol-gel process and their refractive index increases with the calcination temperature and approaches the value for fused silica at high temperatures [13].

Wen and Shetty [10] measured grain orientations in polycrystalline MgF_2 using electron back scatter diffraction (EBSD). For each grain, the refractive index in the direction of light propagation, $n(\theta)$, where θ is the angle between the direction of light propagation and the c-axis of the tetragonal grains, was calculated using the following equation [16]:

$$n(\theta) = \frac{n_o n_e}{\sqrt{\left(n_e^2 \cos^2 \theta + n_o^2 \sin^2 \theta\right)}} \tag{3.3}$$

The values of n_o and n_e for MgF_2 for $\lambda_0 = 589$ nm were calculated using the dispersion equation reported by Dodge [17]. The mean square deviation of the refractive index for light propagation through polycrystalline MgF_2 was then calculated from the following equation:

$$\overline{\Delta n^2} = \frac{1}{N} \sum_{i=1}^{N-1} \left[n(\theta_{i+1}) - n(\theta_i) \right]^2 \tag{3.4}$$

In Eq. (3.4), N is the total number of grains characterized by EBSD for intercept length and orientation along the optical path of the light. A value, $\overline{\Delta n^2} = 2.676 \times 10^{-5}$, calculated for polycrystalline MgF_2 using Eq. (3.4), was then simulated in the model system by selecting a water-glycerol solution with $w_g = 0.785$ or $n_m = 1.4358$ from Eq. (2).

3.3.3 In-Line Transmittance of Silica Suspensions

Figure 3.5 shows plots of the in-line transmittance of silica suspensions as functions of the particle diameter for four volume fractions, ϕ = 0.05, 0.1, 0.2 and 0.3. The filled symbols represent measurements made on monodispersed suspensions, while the open circles represent polydispersed suspensions described later. The solid lines are the plots of the following approximation of the RGD theory used by Harrison [7] and Apetz and van Bruggen [8] to model the effect of grain size on in-line transmittance of polycrystalline ceramics:

$$\frac{I}{I_0} = \exp\left[-\frac{3\pi^2 \phi d_p \overline{\Delta n^2}}{\lambda_0^2} t\right] \tag{3.5}$$

Figure 3.5 shows that Eq. (3.5) gives reasonable predictions of the decrease in transmittance of the silica suspensions with increasing particle size for solids volume fractions of 0.05, 0.1 and 0.2. The transmittances of the silica suspensions with a solids volume fraction of 0.3 are significantly lower than the prediction of Eq. (3.5). The open circles in Figure 3.5 are measured transmittance of poly-disperse silica suspensions in which the volume fractions of the 0.5 μm, 1 μm, and the 1.5 μm particles, represented as ϕ_1, ϕ_2 and ϕ_3, respectively, met the following two conditions:

$$\left(\phi_1 + \phi_2 + \phi_3\right) = \phi = 0.1 \tag{3.6}$$

$$\overline{d_N} = \left(\frac{n_1}{N} d_1 + \frac{n_2}{N} d_2 + \frac{n_3}{N} d_3\right) = 1\ \mu m \tag{3.7}$$

In Eq. (3.7), n_1, n_2, and n_3 are the number of particles of diameter, d_1 = 0.5 μm, d_2 = 1 μm, and d_3 = 1.5 μm, respectively, in a unit volume of the suspension, and N is the total number of particles in the unit volume of the suspension. $\overline{d_N}$ is the number fraction

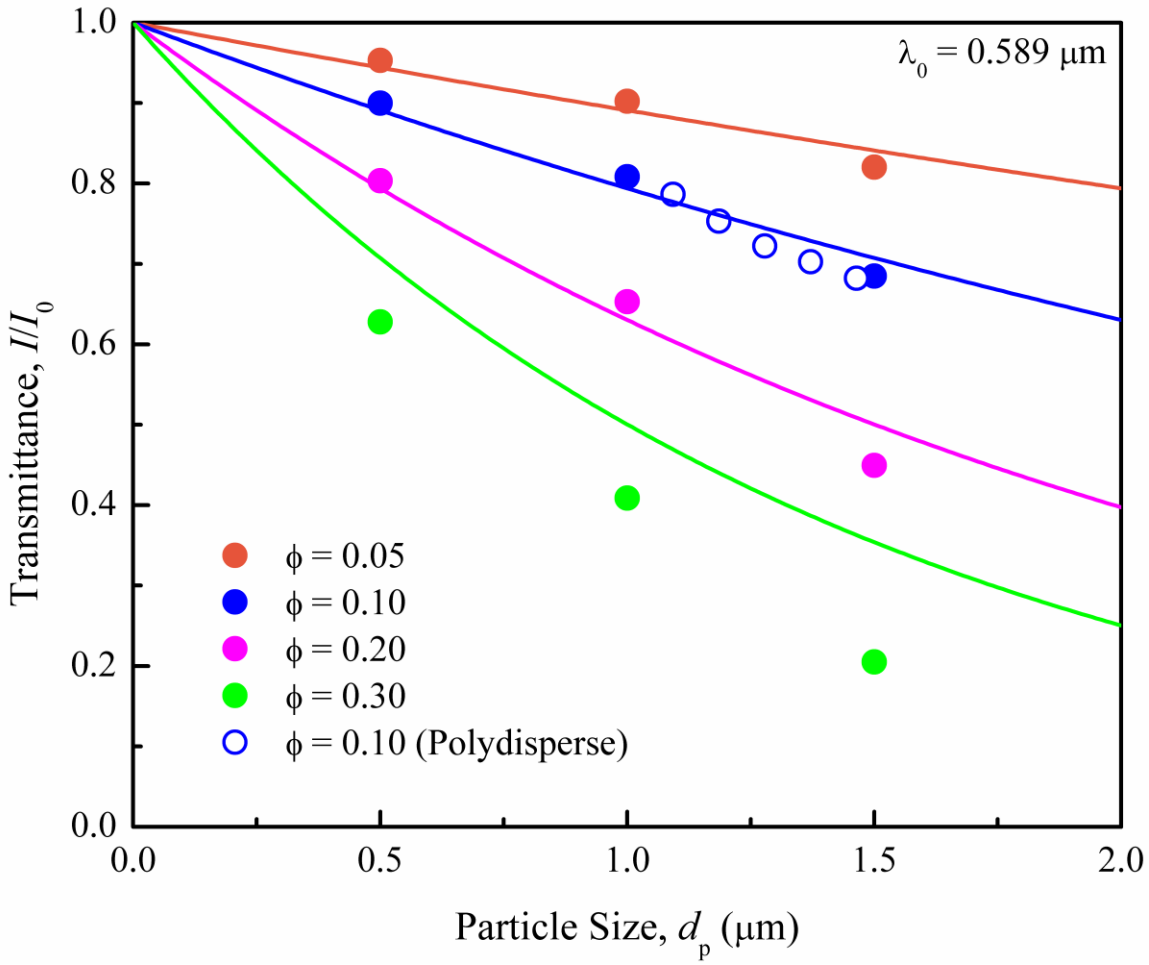

Figure 3.5 Variations of the transmittance of silica microsphere suspensions in a solution of glycerol-water with a refractive index, $n_m = 1.4358$. The lines are plots of Eq. (3.5).

average diameter of the particles in the suspension. The average diameter of the polydisperse particles plotted in Figure 3.5 is the volume fraction average diameter defined by the following equation:

$$\overline{d_\phi} = \left(\frac{\phi_1}{\phi} d_1 + \frac{\phi_2}{\phi} d_2 + \frac{\phi_3}{\phi} d_3 \right) = \frac{1}{\phi} \sum_{i=1}^{3} \phi_i d_i \tag{3.8}$$

Polydisperse suspensions with five different combinations of the volume fractions, ϕ_1, ϕ_2 and ϕ_3, meeting the constraints of Eqs. (3.6) and (3.7), were prepared and characterized by measuring their transmittance (see Table 3.2). The open circles in Figure 3.5 show the measured transmittance as a function of the volume fraction average diameter, $\overline{d_\phi}$. The fact that these experimental data follow the theoretical line of Eq. (3.5) for $\phi = 0.1$ suggests the volume fraction average diameter, $\overline{d_\phi}$, is the pertinent particle size parameter when applying particle scattering theories to polydisperse systems. The implications of this finding for polycrystalline ceramics with a distribution of grain sizes will be addressed in the discussion section.

3.4 Discussion

Light scattering by single spherical particles dispersed in a medium is treated by the Mie solution to Maxwell's equation for the diffraction of a plane monochromatic wave by a homogeneous sphere surrounded by a medium of different refractive index [9, 18]. His solution for scattering efficiency of the particle, *K*, is of the following form:

$$K = K(m, x) \tag{3.9}$$

In Eq. (3.9), *m* is the relative refractive index defined by

Table 3.2 The volume fraction (ϕ) of each particle size, number fraction average diameter ($\overline{d_N}$) and volume fraction average diameter ($\overline{d_\phi}$).

ϕ_2	ϕ_3	ϕ_1	$\overline{d_N}$	$\overline{d_\phi}$
0	0.096429	0.003571	1	1.464
0.02	0.077143	0.002857	1	1.371
0.04	0.057857	0.002143	1	1.279
0.06	0.038571	0.001429	1	1.186
0.08	0.019286	0.000714	1	1.093
0.1	0	0	1	1.000

$$m = \frac{n_{\mathrm{p}}}{n_{\mathrm{m}}} \tag{3.10}$$

and, x is the normalized particle size defined as follows:

$$x = \frac{\pi d_{\mathrm{p}} n_{\mathrm{m}}}{\lambda_0} \tag{3.11}$$

In Eq. (3.11), λ_0 is the wavelength of light in vacuum. Mie's solution is rigorous and applicable to a spherical particle of arbitrary size and refractive index relative to the medium. But, it is a numerical solution with a converging infinite sum of terms that can be calculated to the required accuracy with a computer software [19].

RGD theory describes light scattering by a spherical particle under the following conditions [9]: (1) the refractive index of the particle is close to that of the medium, i.e., $|m\text{-}1| << 1$, (2) the "phase shift" is small, i.e., $2x(m\text{-}1) << 1$. And as a consequence of the above conditions, (3) the scattering efficiency is small, i.e., $K << 1$. In the $(m - x)$ regime defined by these conditions, a large particle size approximation of the scattering efficiency in the RGD theory is given by the following equation:

$$K = 2(m-1)^2 x^2 \tag{3.12}$$

Figure 3.6 compares the scattering efficiency calculated using Eq. (3.12) with the Mie solution calculated using the software [19] for values of m and x applicable to the silica-glycerol/water system. For the parameters of the model system, the approximate form of the RGD solution (Eq. (3.12)) and the Mie solution are essentially identical.

The scattering coefficient of a two-phase system consisting of monodisperse spherical particles in a homogeneous medium is obtained from the single-particle scattering efficiency using the following equation [9]:

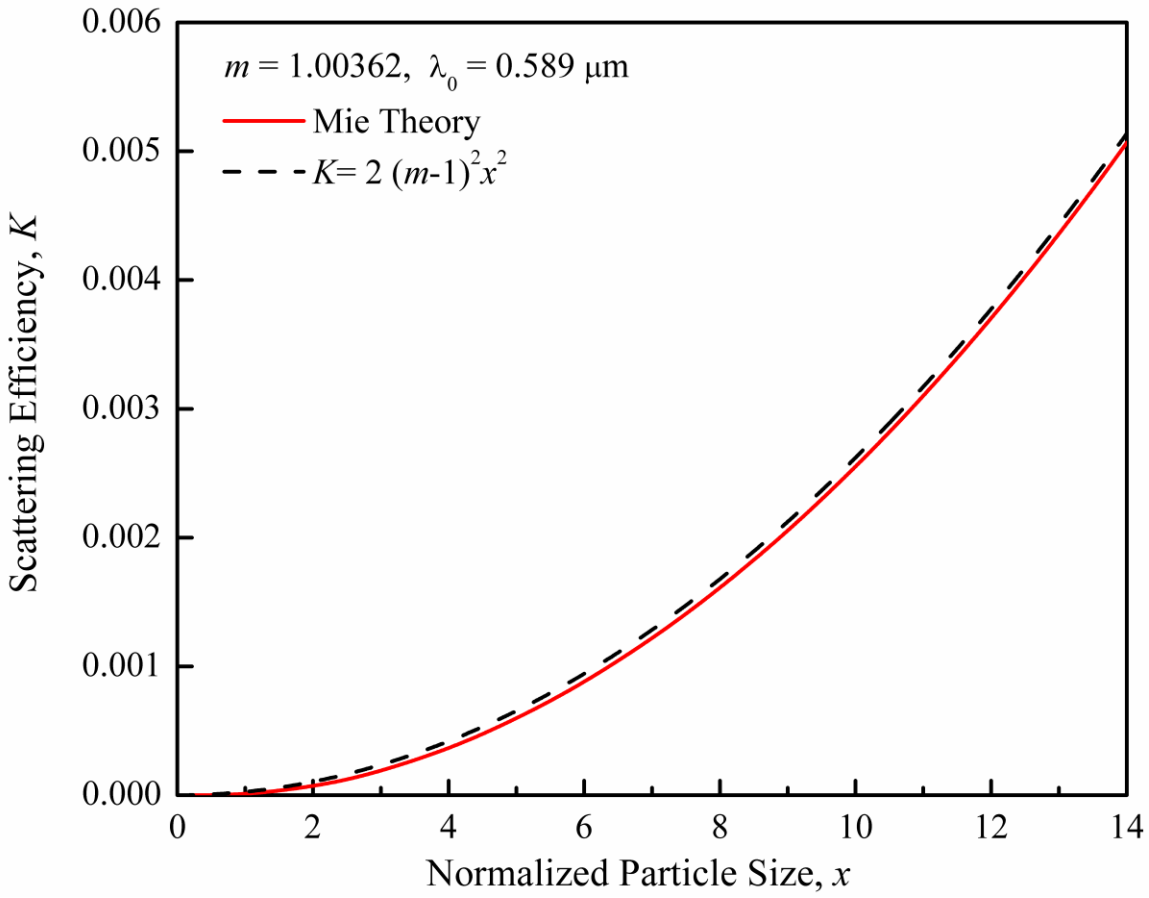

Figure 3.6 Scattering efficiency of a spherical particle in a medium, K, predicted by the Mie theory and an approximate analytical form of the Raleigh-Gans-Debye theory plotted as functions of the normalized particle size, x.

$$\gamma = \frac{N\pi d_p^2 K}{4} \tag{3.13}$$

In Eq. (3.13), N is the number of particles per unit volume. It is important to note here that the formulation of the scattering coefficient, γ, for a multiparticle system, such as a suspension, in terms of the single-particle scattering efficiency, K, is valid only under the following conditions: (1) particles in the suspension scatter light independently, and (2) each particle causes only single scattering [9]. It is useful to express the scattering coefficient in terms of the volume fraction of the spherical particles:

$$\gamma = \frac{3K\phi}{2d_p} = \frac{3\pi^2 d_p \left(n_p - n_m\right)^2}{\lambda_0^2}\phi \tag{3.14}$$

Figure 3.7 compares the scattering coefficients measured for the silica-glycerol/water system, $\gamma = [-\log_e(I/I_0)]/t$, with the predictions of Eq. (3.14) shown as solid lines. It is clear that Eq. (3.14) fits the data only for values of ϕ up to 0.2 and for particle diameters, d_p = 0.5 and 1.0 μm. For higher volume fraction and larger particle size, the scattering coefficient deviates to higher values.

The deviation of the measured scattering coefficients for the silica microspheres from the linear dependence on the volume fraction, ϕ, (Eq. (3.14)) at large volume fractions can potentially be due to three sources: (a) silica microspheres have a range of diameters (polydispersed) rather than a single diameter (monodispersed), (b) silica microspheres aggregate in suspension due to van der Waals attraction, or (c) dependent and multiple scattering prevail at high particle volume fraction. The first two sources were discounted based on the following experimental evidence. Measurements of silica particle diameters using scanning electron microscope (SEM) images revealed that the number mean

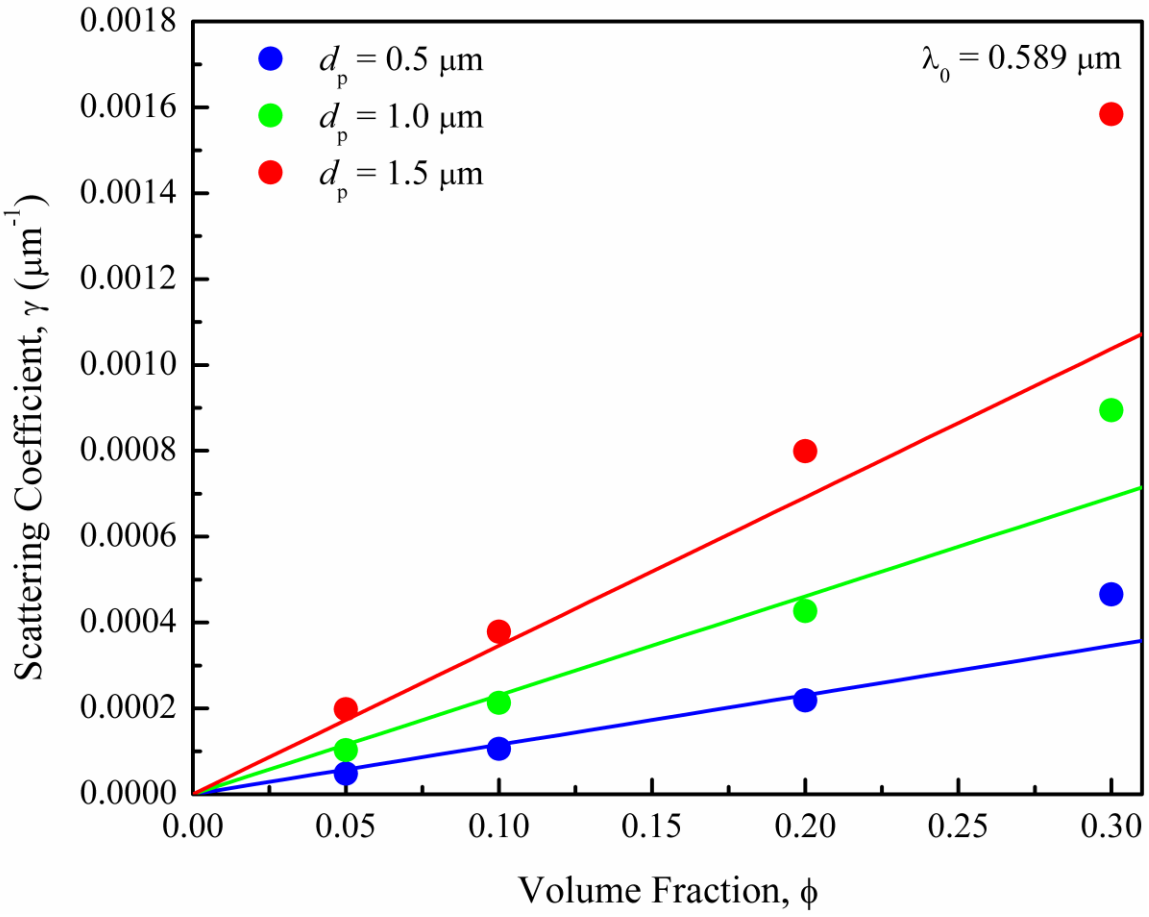

Figure 3.7 Variations of the scattering coefficients, γ, calculated from the measured transmittance of silica-water/glycerol suspensions as functions of the silica volume fraction, ϕ, for the three particle diameters. The lines are plots of Eq. (3.14).

diameters, $\overline{d_N}$, and standard deviations for the three nominal sizes were 0.495 ± 0.0265 μm, 1.019 ± 0.0443 μm, and 1.513 ± 0.0465 μm, respectively. The corresponding volume fraction mean diameters were 0.499, 1.025 and 1.517 μm, respectively (Figure 3.8). The differences between the number mean diameters and the volume fraction mean diameters of the silica microspheres were too small to account for the systematic deviations of the measured scattering coefficients from the theoretical predictions. Particle aggregation was eliminated as a source of the deviation because suspensions prepared with 0.2 w% poly(methacrylic acid) (Grade DARVAN C-N, Vanderbilt Minerals LLC, Norwalk, CT) as a dispersant showed same transmittance and scattering coefficient as the suspensions without the dispersant.

Based on the above results, it was concluded that the systematic deviations observed in Figure 3.7 must be due to dependent and/or multiple scattering. The results of Figure 3.7 are not surprising in view of the guidelines suggested for applying single-particle scattering theories to multiparticle systems. van de Hulst [9], for example, suggests that a minimum interparticle distance of three times the radius is a sufficient condition for independent scattering. This interparticle spacing is equivalent to a volume fraction of only 0.0335. Further, according to van de Hulst [9], single scattering prevails if $\gamma t < 0.1$. For t = 1000 μm, this sets an upper limit of $\gamma = 0.0001\ (\mu m)^{-1}$. Figure 3.7 shows that only the three lowest measured values of the scattering coefficient are within this upper limit. All the other values exceed this limit.

The results of the present study suggest that light scattering models based on single particle scattering are unlikely to provide a viable physical explanation for the effect of grain size on light transmittance in birefringent polycrystalline ceramics. Even if the

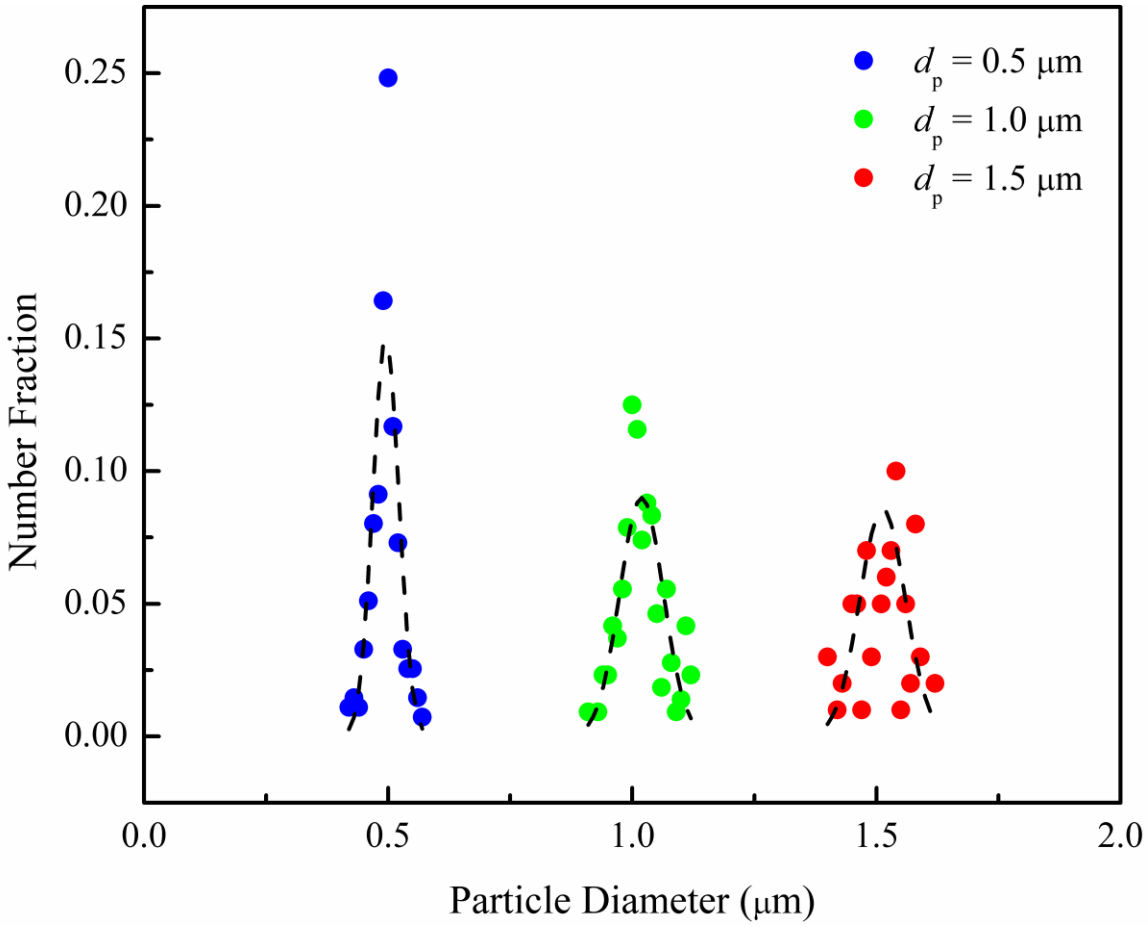

Figure 3.8 Particle size distribution for spherical Stober silica powders

representation of a polycrystalline ceramic as a two-phase composite of spherical particles in a medium is accepted, the volume fraction of the particles would be too high for the single particle scattering theories to be applicable. It is more desirable to seek a model based on light propagation in a random medium where the fluctuations of refractive index and their spatial variations are more representative of polycrystalline materials than what has been modeled to date [3, 6].

A final point that merits discussion is on the particle or grain size that is pertinent when applying particle scattering theories to polydisperse systems. The transmittance measurements on the polydisperse silica suspensions, shown by the open circles in Figure 3.5, provide useful insight on this subject. The five polydisperse suspensions in Figure 3.5 were prepared under two constraints: (a) all of them had the same total volume fraction of solids, $\phi = 0.1$, and (b) the number mean diameter of the particles as defined by Eq. (3.7) was also constant and equal to 1.0 μm. The volume fraction average diameter, $\overline{d_\phi}$, Eq. (3.8), however, varied for the five samples and is plotted in Figure 3.5. The fact that the transmittance of the polydisperse suspensions varies with $\overline{d_\phi}$ and the measured data are close to the theoretical line in Figure 3.5 suggests that $\overline{d_\phi}$ is the pertinent particle size parameter when applying particle scattering theories to polydisperse systems rather than $\overline{d_N}$. This is relevant to polycrystalline optical ceramics, such as MgF_2 and Al_2O_3, because $\overline{d_\phi} = \beta \overline{d_N}$, where β is about 2.3 ± 0.33 for MgF_2 [10] and 2.4 ± 0.46 for Al_2O_3. The light transmittance of polycrystalline ceramics is often plotted as a function of $\overline{d_N}$ instead of $\overline{d_\phi}$. This tends to make the data closer to the predictions of the particle scattering models

[10]. Figure 3.9 illustrates this point with the data from Wen and Shetty [10] for polycrystalline MgF_2. The open circles in Figure 3.9 are the measured in-line transmittance plotted versus the measured mean number grain size,. The solid red line represents the prediction of the approximate form of the RGD theory with $d_p = \overline{d_N} = \overline{G}$. The dashed red line represents the prediction of the approximate form of the RGD theory with $d_p = \overline{d_\phi} = \overline{G_\phi} = 2.32\overline{G}$. It is evident from Figure 3.9 that plotting the data and the RGD theory in terms of the number mean grain size, $\bar{G}$, makes the data appear closer to the theoretical line.

3.5 Conclusions

1. Scattering coefficients for light attenuation in birefringent polycrystalline ceramics scale linearly with mean grain size and inversely with the square of the wavelength of light. These results are qualitatively consistent with two different theories: (a) wave propagation in random media, and (b) an analytical approximation of Raleigh-Gans-Debye theory of light scattering by spherical particles.
2. Comparison of the measured transmittance as a function of mean grain size in birefringent polycrystalline ceramics is not adequate to discriminate between the two theories due to different assumptions in the models with respect to grain shape, size, size distribution and orientation distribution, and associated variations in the refractive index.
3. Measurements of light transmittance and calculations of scattering coefficients in a model silica-glycerol/water system, designed to simulate polycrystalline MgF_2, show systematic deviation from RGD theory for particle volume fraction, $\phi > 0.2$, and large

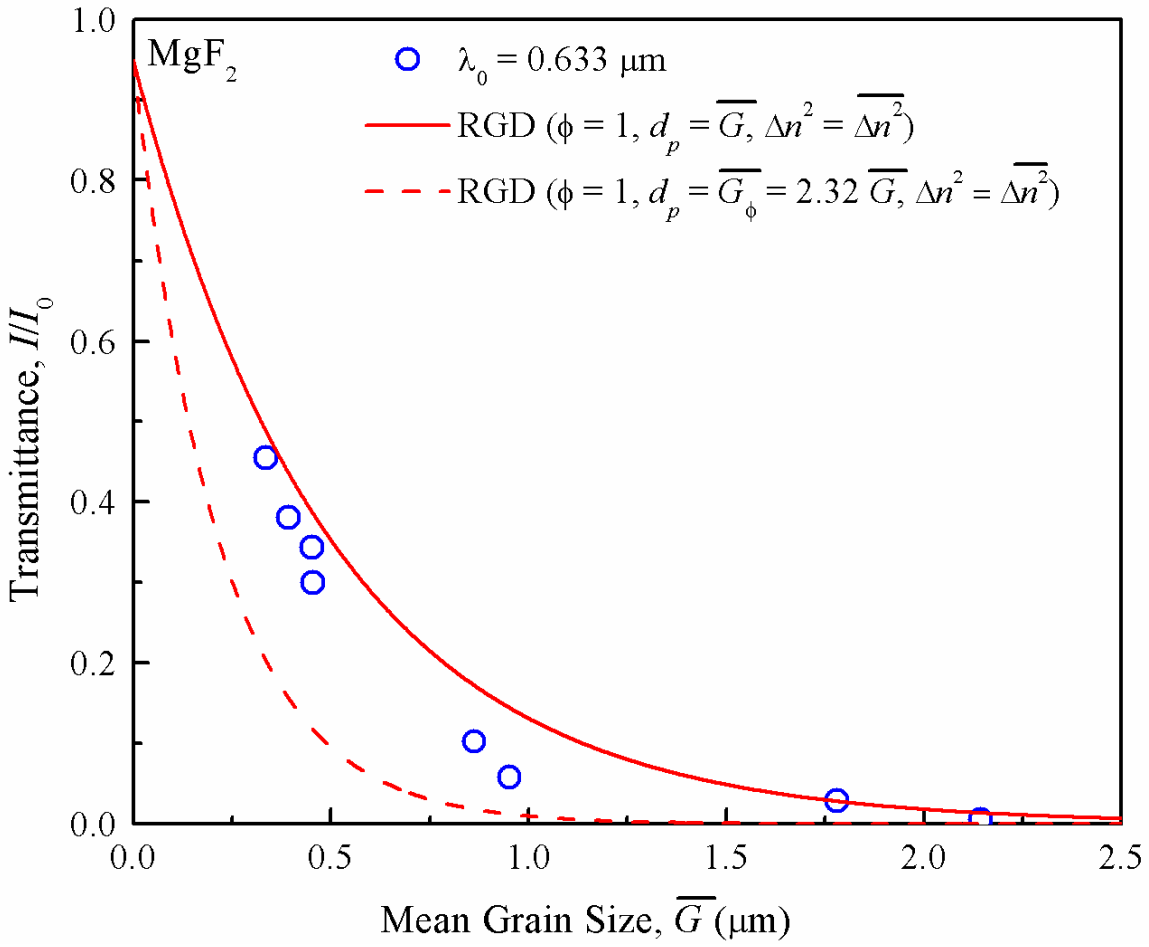

Figure 3.9 Comparison of the measured (open circles) and predictions of an approximate form of the RGD theory for in-line transmittance of polycrystalline MgF_2 as a function of mean grain size. Use of number mean grain size, $\bar{G}$, makes the data appear closer to the theoretical prediction.

particle size ($d_p > 1$ μm). This makes the application of particle scattering theories to light attenuation in birefringent polycrystalline ceramics tenuous.

4. Improved models based on light propagation in random media, which take into account a distribution of grain sizes and orientations, are desired to treat effects of birefringence on light attenuation in polycrystalline ceramics.

3.6 References

[1] D. C. Harris, *Materials for Infrared Windows and Domes: Properties and Performance*. SPIE Optical Engineering Press, Bellingham, WA, 1999.

[2] P. Debye and A. M. Bueche, "Scattering by an Inhomogeneous Solid," *J. App. Phys.*, **20**, 518-525 (1949).

[3] C. V. Raman and K. S. Viswanathan, "The Theory of the Propagation of Light in Polycrystalline Media," *Proc. Ind. Acad. Sci. **A***, **41**, 37-43 (1955).

[4] J. B. Keller, "Wave Propagation in Random Media"; pp. 227-46 in *Hydrodynamic Instability*, Proc. Symp. Appl. Math., Vol. XIII, G. Birkhoff, R. Bellman and C. C. Lin (Eds.); American Mathematical Society, 190 Hope St., Providence, RI (1962).

[5] G. S. Ranganath and S. Ramaseshan, "Optical Transmission in Polycrystals," *Optica Acta*, **19** [9] 781-90 (1972).

[6] H. M. Kahan, D. P. Stubbs and R. V. Jones, "The Potentialities of Fine Grained Ceramics for Optical and Acoustical Applications"; pp. 185-203 in *Optical and Acoustical Micro-Electronics*, Microwave Research Institute Symposia Series, Vol. XXIII, J. Fox (Ed.); Polytechnic Press, Brooklyn, NY, 1975.

[7] W. H. Harrison, "Optical Model"; pp. 209-19, Section 3.0 in *Advanced Optical Ceramics*, Phase II, Annual Report, General Electric Company, ONR Contract N00014-78-C-0466, August 31, 1980.

[8] R. Apetz and M. P. B. van Bruggen, "Transparent Alumina: A Light Scattering Model," *J. Am. Ceram. Soc.*, **86** [3] 480-86 (2003).

[9] H. C. van de Hulst, *Light Scattering by Small Particles*. Dover Publications, Inc., New York, NY, 1981.

[10] T. C. Wen and D. K. Shetty, "On the Effect of Birefringence on Light Transmission in Polycrystalline Magnesium Fluoride," *J. Am. Ceram. Soc.*, **98** [3] 829-837 (2014).

[11] W. Stober, A. Fink and E. Bohn, "Controlled Growth of Monodisperse Silica Spheres in the Micron Size Range," *J. Colloid Interface Sci.*, **26**, 62-69 (1968).

[12] A. van Blaaderen and A. Vrij, "Synthesis and Characterization of Monodisperse Colloidal Organo-silica Spheres," *J. Colloid Interface Sci.*, **156**, 1-18 (1993).

[13] F. Garcia-Santamaria, H. Miguez, M. Ibisate, F. Meseguer and C. Lopez, "Refractive Index Properties of Calcined Silica Submicrometer Spheres," *Langmuir*, **12**, 1942-44 (2002).

[14] F. Koohyar, A. A. Rostami, M. J. Chaichi and F. Kiani, "Study on Thermodynamic Properties for Binary Systems of Water + L-Cysteine Hydrochloride Monohydrate Glycerol, and D-Sorbitol at Various Temperatures," *J. Chem.*, **2013**, 1-10 (2013).

[15] I. H. Malitson, "Interspecimen Comparison of the Refractive Index of Fused Silica," *J. Opt. Soc. Am.*, **55**, 1205-09 (1965).

[16] A. Yariv and P. Yeh, *Optical Waves in Crystals: Propagation and Control of Laser Radiation*. John Wiley & Sons, New York, NY (1984).

[17] M. J. Dodge, "Refractive Properties of Magnesium Fluoride," *Appl. Opt.*, **23** [12] 1980-85 (1984).

[18] G. Mie, "Contributions on the Optics of Turbid Media – Particularly Colloidal Metal Solutions," *Ann. Phys.*, **330** [3] 377-445 (1908).

[19] B. Michel, Mie-Calc-Freely Configurable Program for Light Scattering Calculations (Mie Theory), Available at http://www.lightscattering.de/MieCalc/eindex.html, (accessed June 2015).

CHAPTER 4

LIGHT TRANSMISSION IN POLYCRYSTALLINE ALUMINA: EFFECTS OF BIREFRINGENCE AND GRAIN SIZE

4.1 Introduction

Alumina (Al_2O_3) is a versatile ceramic used in structural (cutting tools, thread guides), electrical (insulators), and optical applications [1]. The optical applications of polycrystalline Al_2O_3 began in the early 1960s when Coble [2] developed the first translucent alumina for high pressure sodium vapor lamps. The material, named Lucalox®, is a coarse-grained polycrystalline Al_2O_3 with an average grain size around 30 μm [3]. Lucalox® exhibits high total forward transmittance, but a low in-line transmittance because of the birefringence of the hexagonal crystals. For this reason, Lucalox® is not useful for domes and window applications. About the same time, single crystal or sapphire was being developed and used for domes and windows protecting infrared detectors [4]. Processing and fabrication costs of sapphire limited its use to applications demanding high durability.

Even though translucent polycrystalline Al_2O_3 has been available since the 1960s, the development of fully-dense, fine-grained polycrystalline Al_2O_3 that is transparent with high in-line transmittance did not occur until 2003 [5-7]. Three factors contributed to the development of fine-grained, transparent polycrystalline Al_2O_3. First, a high purity (>99.99%) α-Al_2O_3 powder with submicron mean particle size ($\bar{d}$ = 0.16 μm) and narrow particle size distribution became available. Second, colloidal processing techniques, such

as slip casting, pressure filtration, or gel casting, were employed to form green bodies with high solids fraction and uniform packing. Finally, compacts were consolidated to theoretical density via a combination of sintering at modest temperatures (1200 - 1300°C) and hot-isostatic pressing (HIP). Apetz and van Bruggen [5] demonstrated an in-line transmittance of 70% in the visible range (λ_0 = 0.645 μm) for a fully-dense, 0.8 mm thick Al_2O_3 plate with a mean grain size of 0.3 μm. It is interesting to note that they obtained the fine grain size and theoretical density without using any dopant to inhibit grain growth. Similar results were reported at the same time by Krell *et al.* [6-8]. They emphasized the need to start with a powder with a mean particle size in the range, 0.1 – 0.2 μm instead of nanosize powder, use of slip- or gel casting to achieve high solids fraction and uniform particle coordination, and two-stage densification by sintering to closed porosity followed by HIPing to full density. More recently, Krell *et al*. [9] have reported an in-line transmittance of 72% in the visible range (λ_0 = 0.640 μm) for a 0.8 mm thick polycrystalline Al_2O_3 plate with a mean grain size of 0.33 μm. A number of other investigators have since reported similar results of transparency in fine-grained, polycrystalline Al_2O_3 [10-14].

Unlike the progress made in the processing of fine-grained ceramics for optical applications, the theoretical studies of light transmission in polycrystalline ceramics are limited. Two different theoretical approaches have been used to explain the effect of grain size on light transmittance in birefringent polycrystalline ceramics. The first approach, proposed by Harrison [15] and Apetz and van Bruggen [5], treats a birefringent polycrystalline ceramic as a two-phase composite of isotropic spherical particles of diameter, d_p, and refractive index, n_p, dispersed in a homogenous matrix of refractive index,

n_m. They employed an approximate form of the Raleigh-Gans-Debye theory [16] of light scattering by spherical particles to formulate the scattering coefficient of a polycrystalline material. The second approach, characterized here as wave propagation in random media, was proposed by Debye and Bueche [17], and subsequently employed by Raman and Viswanathan [18] and Kahan *et al.* [19, 20]. Raman and Viswanathan [18] showed the grain orientation distribution and path length of the grain have the cumulative effect of causing light retardation in polycrystalline ceramics. Kahan *et al.* [19, 20] derived the scattering coefficient and Rayleigh ratio in terms of a two-point correlation function with two terms, one corresponding to pore scattering and the other for grain-boundary scattering. It is interesting to note that in both theoretical approaches, the scattering coefficient scales linearly with grain size and inversely with the square of the wavelength of light.

Wen and Shetty [21] critically examined the two theoretical approaches for application to hot-pressed magnesium fluoride (MgF_2). The measured variations of the scattering coefficient with grain size and wavelength of light were consistent with both the RGD theory of particle light scattering and the light retardation theory of Raman and Viswanathan [18]. However, neither of the two theories could accurately predict the absolute value of the transmittance at a given grain size. They attributed the discrepancies to the over-simplification of the polycrystalline microstructure in the theories, specifically, the grain shape and orientation distributions. In the interest of discriminating between the two theories, Wen and Shetty [22] studied light transmission in a model system, silica microspheres dispersed in a solution of water and glycerine, designed to simulate the effects of birefringence in polycrystalline MgF_2. The measured scattering coefficients showed systematic deviations from the RGD theory for particle volume fraction, $\phi > 0.2$,

and particle size $d_p > 1$ μm. Based on these results, Wen and Shetty [22] concluded that light scattering models based on single particle scattering are unlikely to provide viable physical explanation for the effect of grain size on light transmittance in birefringent polycrystalline ceramics. Therefore, models based on wave propagation in random media that take into account the distribution of grain size and orientation are more appropriate for treating the effects of birefringence on light attenuation in birefringent polycrystalline ceramics.

The primary objective of this paper was to investigate the applicability of the theories of wave propagation in random media to light transmittance in polycrystalline Al_2O_3. To this end, the paper reports the processing and the optical properties of fully-dense polycrystalline Al_2O_3 with varying intercept lengths with the theoretical predictions of Raman and Viswanathan [18] and Kahan *et al*. [19, 20]. Specifically, the paper examines the variations of the scattering coefficients of polycrystalline Al_2O_3 with intercept length and wavelength of light. The paper also presents the scattering profiles, i.e., the variations of the scattered light intensity as functions of the scattering angle, for coarse-grained and fine-grained polycrystalline Al_2O_3.

4.2 Theoretical Background

The intensity of light transmitted through a window is given by the following equation [23]:

$$I(t) = I_0 \left[\frac{(1-R)^2 e^{-\gamma t}}{1 - R^2 e^{-2\gamma t}} \right] \tag{4.1}$$

In Eq. (4.1), I_0 is the intensity of the incident light, R is the single-surface reflectance, t is the thickness of the window, and γ is the scattering coefficient that accounts for the light

scattered and/or absorbed in the material. The single surface reflectance for a smooth surface is defined as [23]:

$$R = \left(\frac{1-n}{1+n}\right)^2 \tag{4.2}$$

In Eq. (4.2), n is the average refractive index of the window. Here we summarize the two theoretical models based on wave propagation in random media.

4.2.1 Wave Propagation Theory of Raman and Viswanathan

Raman and Viswanathan [18] assumed a polycrystalline material to be made of uniform, cube-shaped grains with edges of length, Δ, aligned along three optical axes with refractive indices, n_1, n_2 and n_3. An incident light ray traverses the polycrystalline material in a direction parallel to one set of edges that cover a total number, N, grains made up of k_1 grains of refractive index, n_1, k_2 grains of refractive index, n_2 and k_3 grains of refractive index, n_3, through a window of thickness, t. The emergent wave-train was obtained by summing waves with appropriate amplitudes and phases for all possible integral values of k_1, k_2, and k_3 subject to the relation, $k_1+k_2+k_3 = N$:

$$y = P \sum_{k_1+k_2+k_3=N} \left(\frac{N!}{k_1!k_2!k_3!}\right)\left(p_1^{k_1}\, p_2^{k_2}\, p_3^{k_3}\right) e^{\frac{2\pi i}{\lambda_0}[c\tau - Z - (k_1 n_1 + k_2 n_2 + k_3 n_3)\Delta]} \tag{4.3}$$

In Eq. (4.3), y is the amplitude of the emergent wave, P is a factor that accounts for the loss in intensity of light due to reflections at the grain boundaries, and p_1, p_2, and p_3 are the fractions of grains with the three optical axes, respectively, τ is time, and Z is a reference position coordinate at $\tau = 0$. The first two terms in parentheses in Eq. (4.3) represent the number of ways that k_1, k_2, and k_3 grains can be arranged along the optical path and the probability of occurrence of each of the arrangements, respectively. The exponential term

includes the change in amplitude and phase due to light retardation arising from the variation in refractive index along the light path. A number of mathematical manipulations of Eq. (4.3) lead to the following equation for the transmittance:

$$\frac{I}{I_0} = P^2 e^{-\frac{4\pi^2 \Delta \sum p_2 p_3 (n_2 - n_3)^2}{\lambda_0^2} t} \tag{4.4}$$

Or, the scattering coefficient due to the cumulative light retardation can be written as[6]

$$\gamma = \frac{4\pi^2 \Delta \sum p_2 p_3 (n_2 - n_3)^2}{\lambda_0^2} \tag{4.5}$$

4.2.2 Wave Propagation Theory of Kahan *et al.*

The theory of Kahan *et al*. [19, 20] is conceptually similar to that of Raman and Viswanathan [18], but their mathematical approach is quite different. They solve the scalar Helmholtz equation with a two-point correlation function and derive a general equation for the scattering coefficient for combined grain-boundary and pore scattering. They consider grains to be oriented only in two possible orientations corresponding to the highest and the lowest refractive index of the crystal. If pore scattering is negligible relative to grain-boundary scattering and the normalized mean grain intercept length is large ($x >> 1$), their equation for the scattering coefficient reduces to the following form:[7]

$$\gamma = \frac{8\pi^2 \Delta (p_1 p_2)(n_1 - n_2)^2}{\lambda_0^2} \tag{4.6}$$

It should be noted that Eq. (4.6) is similar to Eq. (4.5) in the dependence of γ on Δn,

---

[6] See Appendix D for derivations of this equation.
[7] See Appendix E for derivations of this equation.

Δ, and λ_0. The absolute values of γ differ in the two expressions due to the difference of assumptions about grain orientations in each of the two theories. Kahan *et al.* [19, 20] assumed a more restrictive grain-orientation distribution (only two orientations), while Raman and Viswanathan [18] assumed three orientations. This study focuses mainly on comparing the measured transmittance of polycrystalline Al_2O_3 with the theoretical formulations of the scattering coefficient, γ, developed by Raman and Viswanathan (Eq. (4.5)) and Kahan *et al.* (Eq. (4.6)).

4.3 Experimental Procedures

4.3.1 Processing of Dense Polycrystalline Al_2O_3

Colloidal processing was used to fabricate dense polycrystalline Al_2O_3. An alumina powder (grade: TM-DAR, Taimei Chemical Company, Tokyo, Japan) of high purity (99.99 w% Al_2O_3), high surface area (13.3 m^2/g), and small average particle size (0.17 μm) was used to prepare a water-based suspension with high solids content. Viscosity measurements were used to identify the optimum conditions for the preparation of stable aqueous slurries. A slurry with 75w% of Al_2O_3 and 0.1 mg/m^2 of dispersant (grade: DARVAN C-N, Vanderbilt Minerals LLC, Norwalk, CT) was the starting point. The slurry tended to aggregate without the dispersant, and 0.1 mg/m^2 amount of dispersant was the smallest increment for the lab test. Ammonium hydroxide and citric acid were used to change the pH. Then, the slurries were ball-milled with alumina grinding media for 2 hours before the viscosity was measured using a rotary viscometer (model RVDV II + Pro Extra, Brookfield, Stoughton, MA) with shear rates of 2.8, 5.6, 14 and 28 s^{-1}.

The stabilization of alumina slurry with high solid content was achieved at a PH of 9.3-10 with 0.1 mg/m^2 amount of dispersant [24, 25]. The stabilized slurry not only showed

low viscosity but also ensured the particles did not settle within a short period of time. The final slurry exhibited a shear-thinning behavior (i.e., a reduction in apparent viscosity with increasing shear rate) [24], as shown in Figure 4.1. Polyethylene glycol was used as a binder (0.2 w%, PEG 400, Alfa Aesar, Ward Hill, MA) to increase the strength of the green compacts. The suspension was ball milled for eight hours to breakdown agglomerates.

Disk-shaped green compacts of the alumina were consolidated directly from the stable suspension by pressure filtration using the device shown in Figure 4.2. A pressure of 20 MPa was applied during filtration for 10 minutes. The disks were dried in a sealed chamber with increased humidity for two days before sintering. The dried compacts were bisque-fired in air at 700°C for 1 hour to remove organic additives. Sintering was done in air at temperatures ranging from 1200 to 1600°C for 4 hours. The sintered compacts were hot-isostatically-pressed (HIPed) at 200 MPa for 4 hours in argon either at 1200 °C (disks sintered at 1200 to 1300°C) or at 1400°C (disks sintered at 1400 to 1600°C). The sintered and HIPed disks were surface finished using a series of grinding and polishing steps to obtain a final specimen thickness of 1 mm and a surface roughness, $Rq \sim$ 20 nm. The densities of the sintered and HIPed disks were measured using the Archimedes method [26].

4.3.2 Measurements of Grain Sizes and Orientations by Electron Backscatter Diffraction (EBSD)

The grain sizes and orientations in the polycrystalline Al_2O_3 were characterized by EBSD. A field emission gun scanning electron microscope (Phillips XL/30 FEGSEM, Eindhoven, Netherlands) equipped with a sensitive CCD camera and EBSD software (OIM

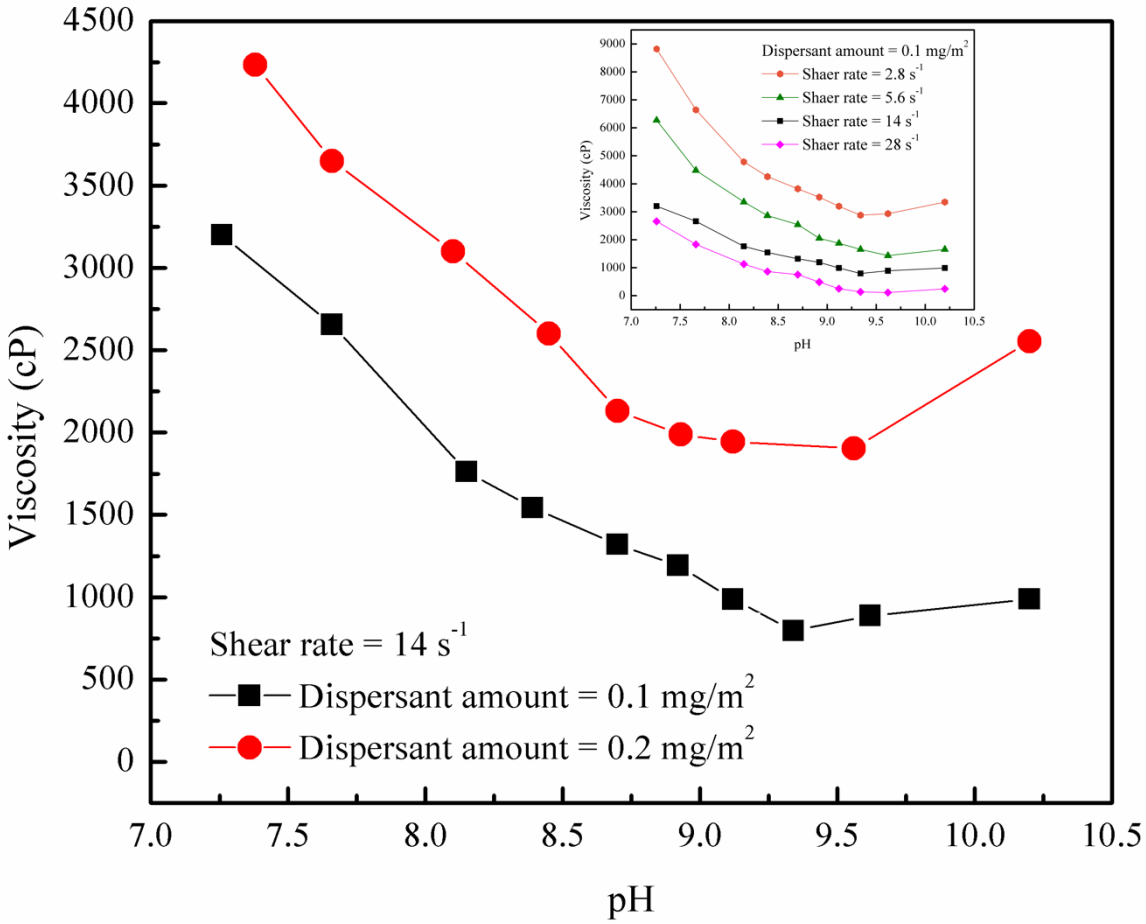

Figure 4.1 Viscosity measurements at various pH, dispersant amount and shear rate (2.8, 5.6, 14 and 28 s^{-1}).

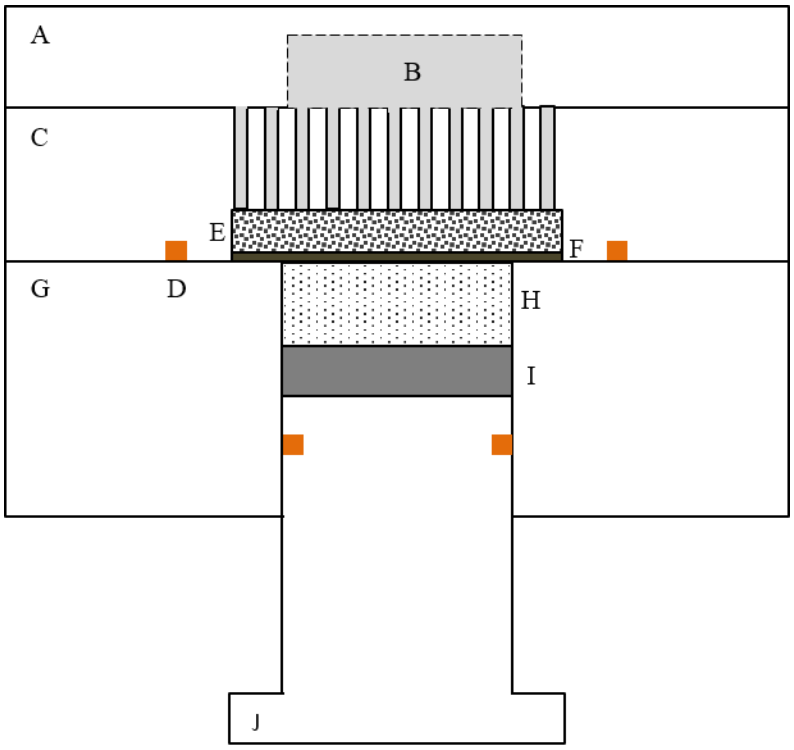

Figure 4.2 Schematic of the pressure filtration devices. A: drain plate, B: outlet for the filtrate, C: filter plate, D: o-ring, E: porous metal disk, F: filter paper, G: bore plate, H: alumina suspension, I: Teflon disk, J: cylinder

Analysis and Data Collection, Version 7, EDAX) was used. The SEM was operated at 20 kV and 3 nA beam current and EBSD patterns collected at 50 or 70 nm per step and 100 steps/s. The EBSD data collected over a mapped region were transformed to an orientation image, such as the one shown in Figure 4.3 for polycrystalline Al_2O_3 sintered at 1210°C, by assigning colors to grains of different orientations as indicated by the standard projection triangle. In this process of image creation, the software employs two cleanup functions: neighbor-orientation correlation and grain confidence index (CI) standardization. Both functions operate by examining each data point individually, comparing each data point to its neighbors, and removing unreliable or nonindexed points from the map. Then, the software replaced each unreliable data point with a more reliable orientation based on neighboring pixels. However, the points with lower than 0.1 confidence index were excluded from the image. These nonindexed pixels are indicated in black (see Figure 4.3). Error in grain size is reduced to less than 5% when 90% of image area is indexed using image cleanup functions [27]. For example, in Figure 4.3, 94.8% of the image area was indexed by the software. Although a highest spatial resolution of 15 nm is feasible and quoted, the practical limit of the grain size that can be measured currently with EBSD mapping is 0.2 μm. An orientation angle resolution in the range 0.5-1° is quoted for the EBSD technique [27, 28]. The intercept length and grain size measurements followed the same methods as described in Section 2.3.2. In addition to the mean intercept lengths, the EBSD software also provided intercept-length distributions and grain-orientation distributions from the EBSD data of a mapped region.

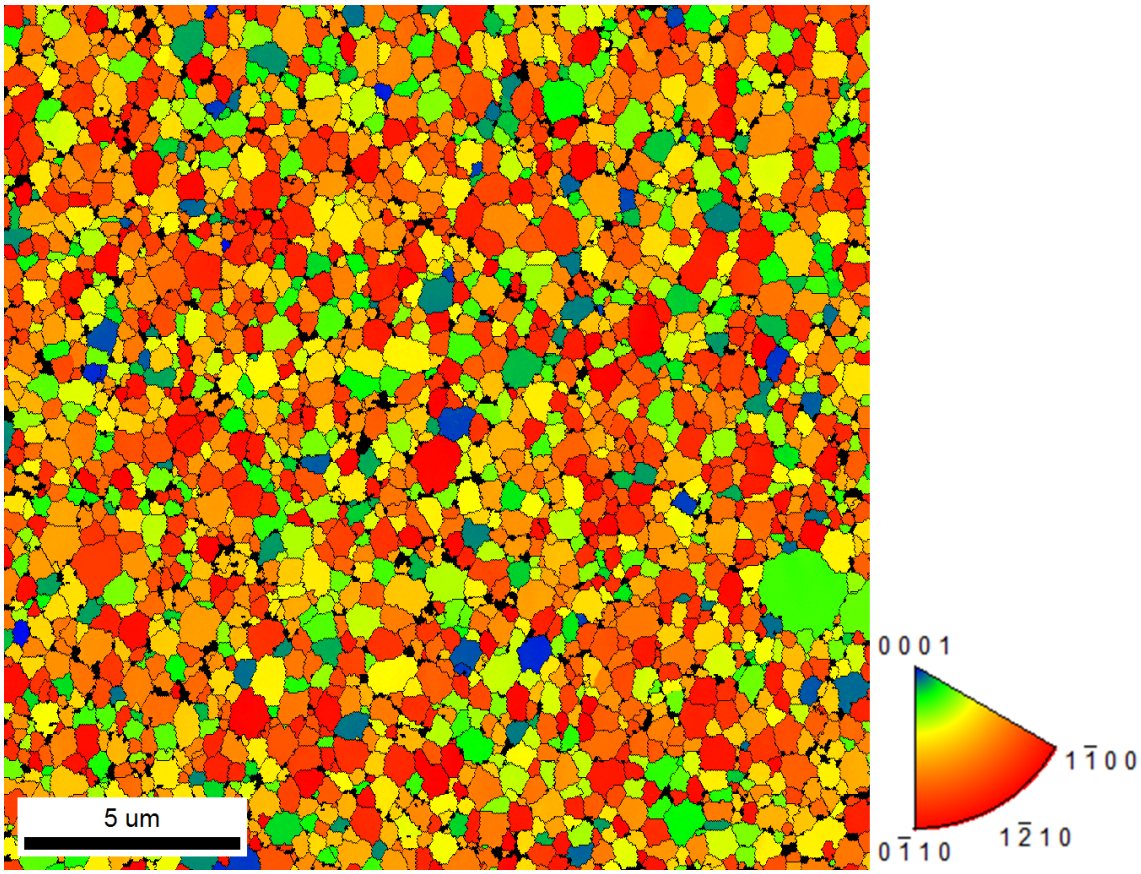

Figure 4.3 Microstructure of polycrystalline Al_2O_3 sintered at 1210°C for 4 hours as revealed by EBSD. The color key for orientation is shown by the standard triangle.

4.3.3 Measurement of In-Line Transmittance

In-line transmittance, I/I_0, was measured using three systems: (a) single wavelength laser and detector system on an optical bench, (b) a spectrophotometer operating in a wavelength range of 0.19 to 1.1 μm, and (c) an FTIR (Fourier Transform Infra Red) operating in a wavelength range, 1.66 to 10 μm.

Lasers of three different wavelengths, 0.633 μm (He-Ne laser, model 1122, JDS Uniphase, Milpitas, CA), 1.064 μm (YAG laser, model 4400, Quantronix Corp., East Setauket, NY), and 3.39 μm (He-Ne laser, model R-32172, Newport, Irvine, CA) were used in the single wavelength laser measurements. An Si detector was used to measure the incident (I_0) and the transmitted (I) intensities of the 0.633 μm and 1.064 μm lasers. A PbSe detector (model PDA20H, Thor Labs, Newton, NJ) was employed with the 3.39 μm laser. The long distance between the specimen and the detector (1 m) and the small active area of the detector ensured a small solid angle, ~0.5°, for measuring the light intensities. Because of this characteristic, transmittance measurements with the single-wavelength laser and detector system are sometimes referred to as real-in-line transmitta In-line transmittance (IT) was also measured with two commercial instruments, a spectrophotometer (UV mini-1240, Shimadzu, Japan) and an FTIR (Excalibur 3100, Varian Inc., Palo Alto, CA). The spectrophotometer had two light sources: (1) a deuterium lamp covered the wavelength range from 0.19 to 0.34 μm, and (2) a halogen lamp covered the wavelength range from 0.34 to 1.1 μm. The transmittance spectra were measured by a silicon photodiode detector at a scanning speed of 700 nm per minute and 1 nm per step. nce (RIT) [5]. The FTIR was equipped with a ceramic filament light source, a KBr beam splitter, and a deuterated triglycine sulfate (DTGS) detector. The scanning parameters of

the FTIR included 5 kHz scanning speed and 4 cm^{-1} resolution. Both the spectrophotometer and the FTIR had large aperture angles (3-5°).

4.3.4 Measurements of Scattering Profiles and Calculation of Forward Scatter

The measurements of scattering profiles were performed at an off-campus facility (Schmitt Industries, Inc., Portland, OR). The measurements were made at the wavelength of 0.633 μm with a Si detector, and at the wavelength of 3.39 μm with an indium antimonide (InSb) detector. The sample was vertically mounted in the optical positioner. An optical chopper chopped the laser beam at 210 Hz to provide modulated light for the detectors and a reference signal for the lock-in amplifier. At the start of the measurements, the transmitted beam was focused in the center of the detector. The scattered light from the specimen was measured as a function of scattering angle, which was referenced from the initial detector location. The scattering signal was collected between the angles from -1° to 90° with aperture diameter ranging from 1064 to 13850 μm, and the detector arm was rotated with various step angles from 0.041° to 0.529°. The measured data were collected and analyzed by a software (CASI Analysis, Schmitt Measurement System, Inc. Portland, OR).

The scattering profiles were measured with a single crystal sapphire, two fine-grained polycrystalline Al_2O_3 ($\bar{G}$ = 0.62 and 1.00 μm) and one coarse-grained polycrystalline Al_2O_3 (Lucalox®, $\bar{G}$ = 25 μm). The measurements were made with a specimen thickness of 1 mm, surface roughness of 10 nm (RMS). The background signal was detected without the specimens.

The signal collected within a solid angle of 0.5° was considered as the transmitted

intensity. The forward scatter (S_F) was obtained between 0.5° to 90° using the following equation [29]:

$$S_F = 2\pi \int_{0.5}^{90} \frac{P_s \sin\theta_s}{P_i \Omega_s} d\theta_s \tag{4.7}$$

where P_s is the power measured by a detector at a scattering angle θ_s from the incident light direction, P_i is the power measured by the detector in the direction of the incident beam without the specimen, and Ω_s is the solid angle subtended by the detector as seen from the scattering surface [30]:

$$\frac{1}{\Omega_s} = \frac{L^2}{\pi l^2} \tag{4.8}$$

where L is the distance from the specimen surface to the aperture in front of the detector and l is the radius of the aperture in front of the detector.

4.4 Experimental Results

4.4.1 Densities, Grain Sizes and Orientations of the Polycrystalline Al_2O_3

Figure 4.4 shows plots of the densities of the disks after sintering and HIPing as functions of the sintering temperature. The density after sintering increased rapidly at sintering temperatures above 1200°C and reached a maximum value of 3.983 g/cm^3 at 1300°C. The density after sintering was slightly lower when sintered at temperatures above 1300°C. The density after HIPing was essentially theoretical (3.986 g/cm^3) for all disks sintered at 1225°C and above.

Figure 4.5 shows the grain intercept length distribution for Al_2O_3 sintered at 1210°C. The mean intercept length, $\bar{L}$, for this specimen, calculated using Eq. (2.13) with 8380 grain intercepts, was 0.338 μm. The mean grain size, $\bar{G}$, was calculated using $\bar{G} =$

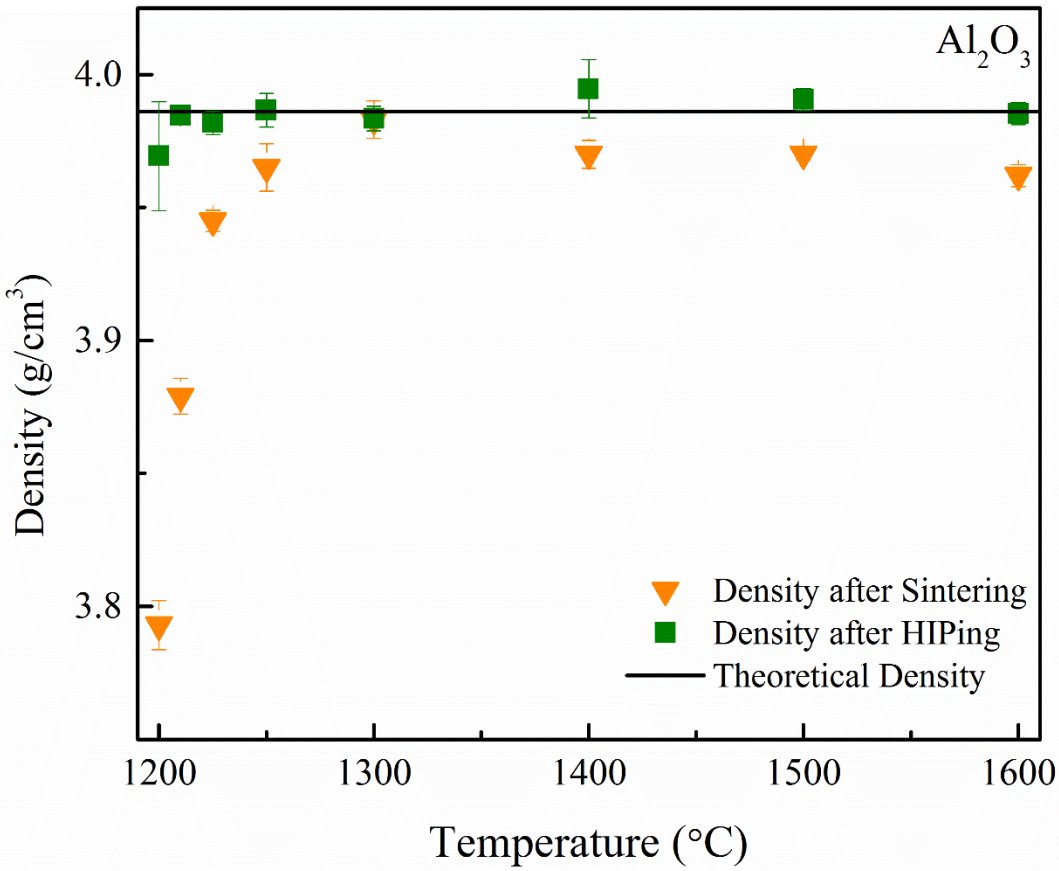

Figure 4.4 The density measurement of sintered and HIPed polycrystalline Al_2O_3.

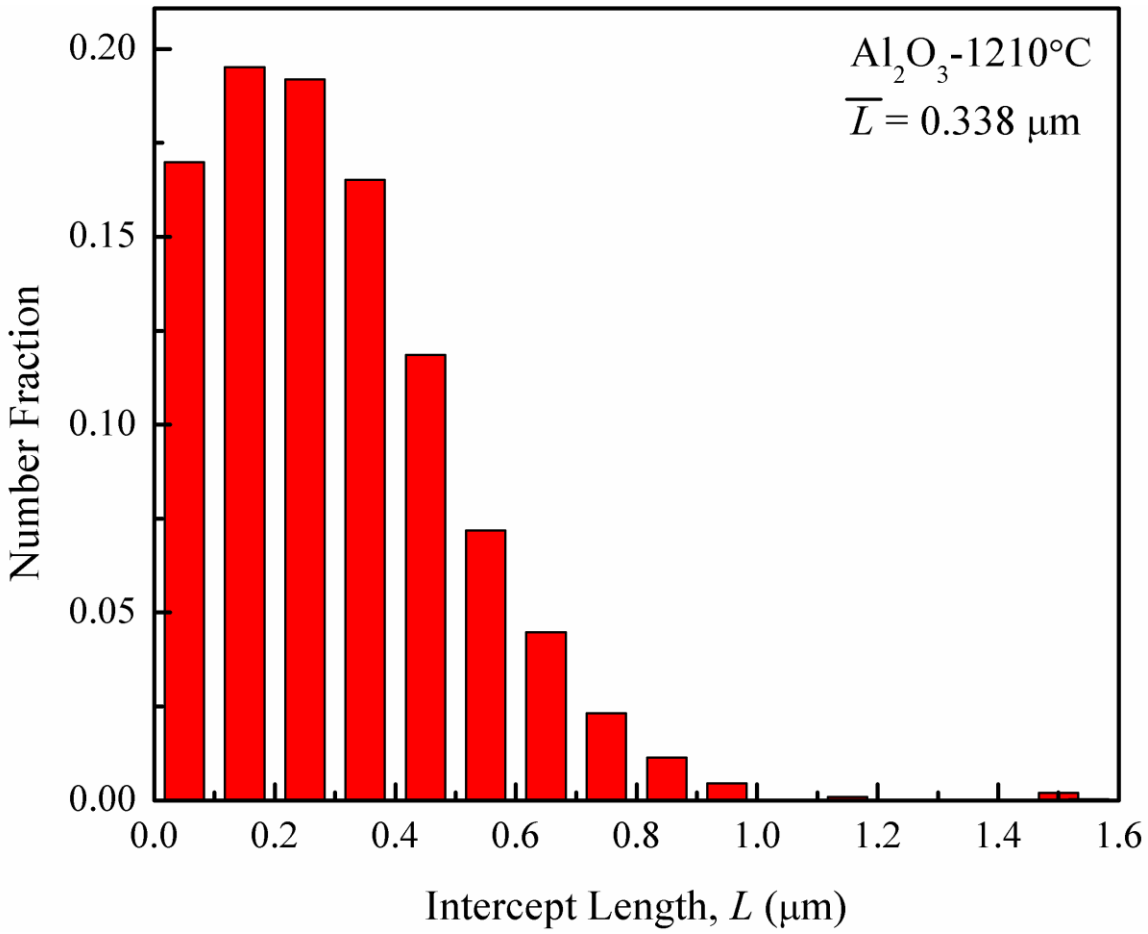

Figure 4.5 Histogram of grain intercept length for polycrystalline Al_2O_3 annealed at 1210°C for 4 hour as measured by EBSD.

Table 4.1 Mean grain intercept lengths, mean orientations and mean square deviations of refractive index for polycrystalline Al_2O_3.

Processing History	$\bar{L}$ (μm)	$\bar{\theta}$ (°)	$\overline{\Delta n^2}$ (x10^5)		
			0.633 μm	1.064 μm	3.39 μm
Sintered 1210 / HIPed 1200	0.338	57.30	1.126	1.098	0.963
Sintered 1225 / HIPed 1200	0.363	57.91	1.099	1.072	0.940
Sintered 1250 / HIPed 1200	0.372	57.73	1.158	1.129	0.991
Sintered 1300 / HIPed 1200	0.529	56.19	1.153	1.124	0.986
Sintered 1400 / HIPed 1400	1.097	55.21	1.040	1.014	0.890
Sintered 1500/ HIPed 1400	2.248	58.08	1.099	1.072	0.941
Average		57.07	1.112	1.085	0.952

$1.558\bar{L}$, with assumption of the grains in the shape of tetrakaidecahedron [31]. Table 4.1 lists the mean intercept lengths for polycrystalline Al_2O_3 sintered at various temperatures. The mean intercept length increased from 0.338 μm to 2.248 μm as the sintering temperature increased from 1210 to 1600°C. Table 4.1 also lists the mean grain orientation ($\bar{\theta}$, Eq. (2.16)) and mean square deviation of the refractive index ($\overline{\Delta n^2}$, Eq. (2.17)) for Al_2O_3 sintered at different temperatures. The average grain orientation ranged from 55.21° to 58.08° with no specific trend with sintering temperature or grain size. The mean grain orientation for all the materials was 57.1°, close to the theoretical value (57.3°) for isotropic random orientation distribution. Similar to $\bar{\theta}$, $\overline{\Delta n^2}$ did not show any trend with sintering or grain size. $\overline{\Delta n^2}$ did decrease systematically with wavelength from 1.112 x 10^{-5} at a wavelength of 0.633 μm to 0.952 x 10^{-5} at 3.39 μm. temperature

Figure 4.6 shows a plot of the cumulative fraction of the grains, $F(\theta)$, as a function of the grain orientation angle, θ, for Al_2O_3 sintered at 1210°C as measured by EBSD. The solid line in Figure 4.6 is the cumulative distribution for random isotropic distribution of grain orientations as defined in Eq. (2.15).[8] Grains oriented along the *c*-axis (θ = 0) were relatively few and are shown by the blue color in Figure 4.3. It is noted in Figure 4.6 that grains in polycrystalline Al_2O_3 were randomly oriented and this was true for specimens sintered at all temperatures.

[8] See Appendix F for derivations of this equation.

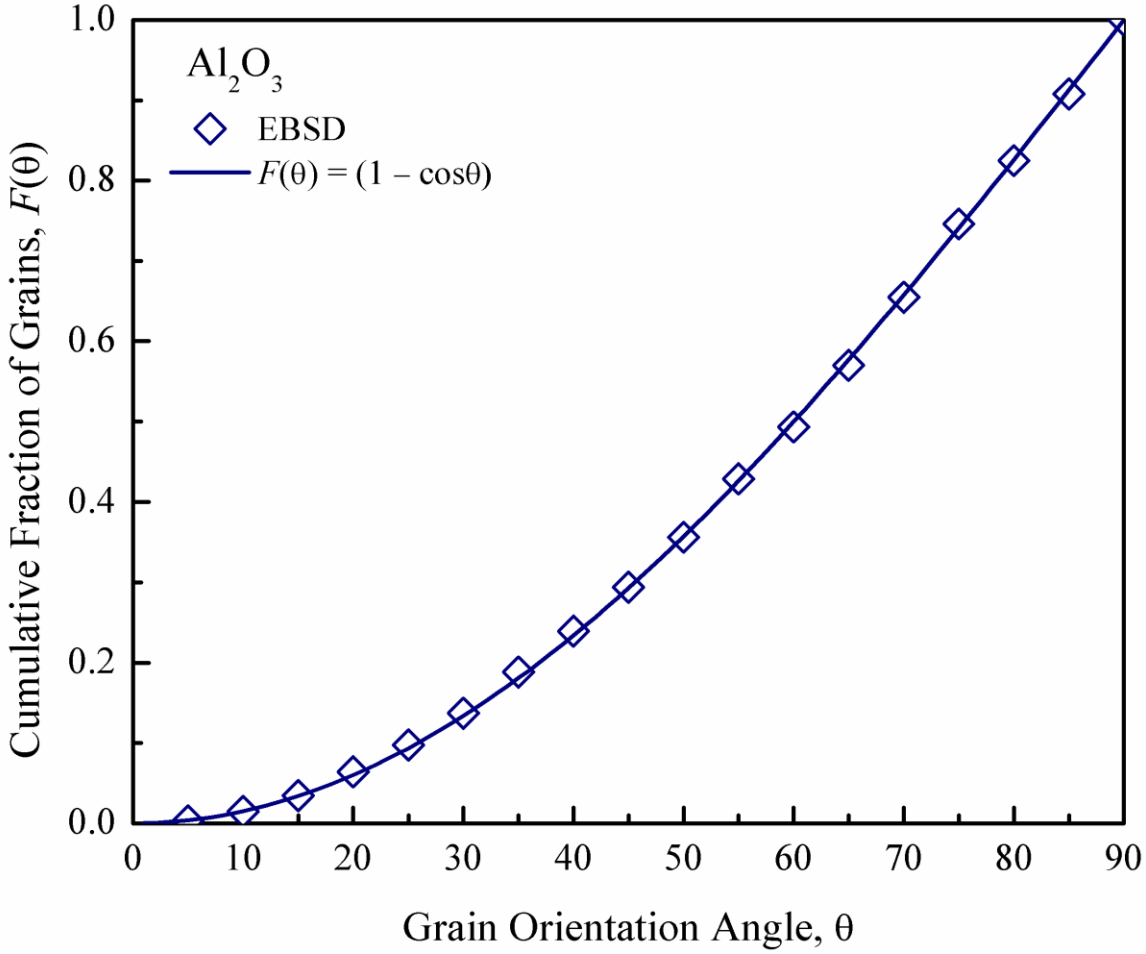

Figure 4.6 Cumulative distribution of grain orientations in Al_2O_3 annealed at 1210°C for 4 hours measured by EBSD compared with isotropic random distribution.

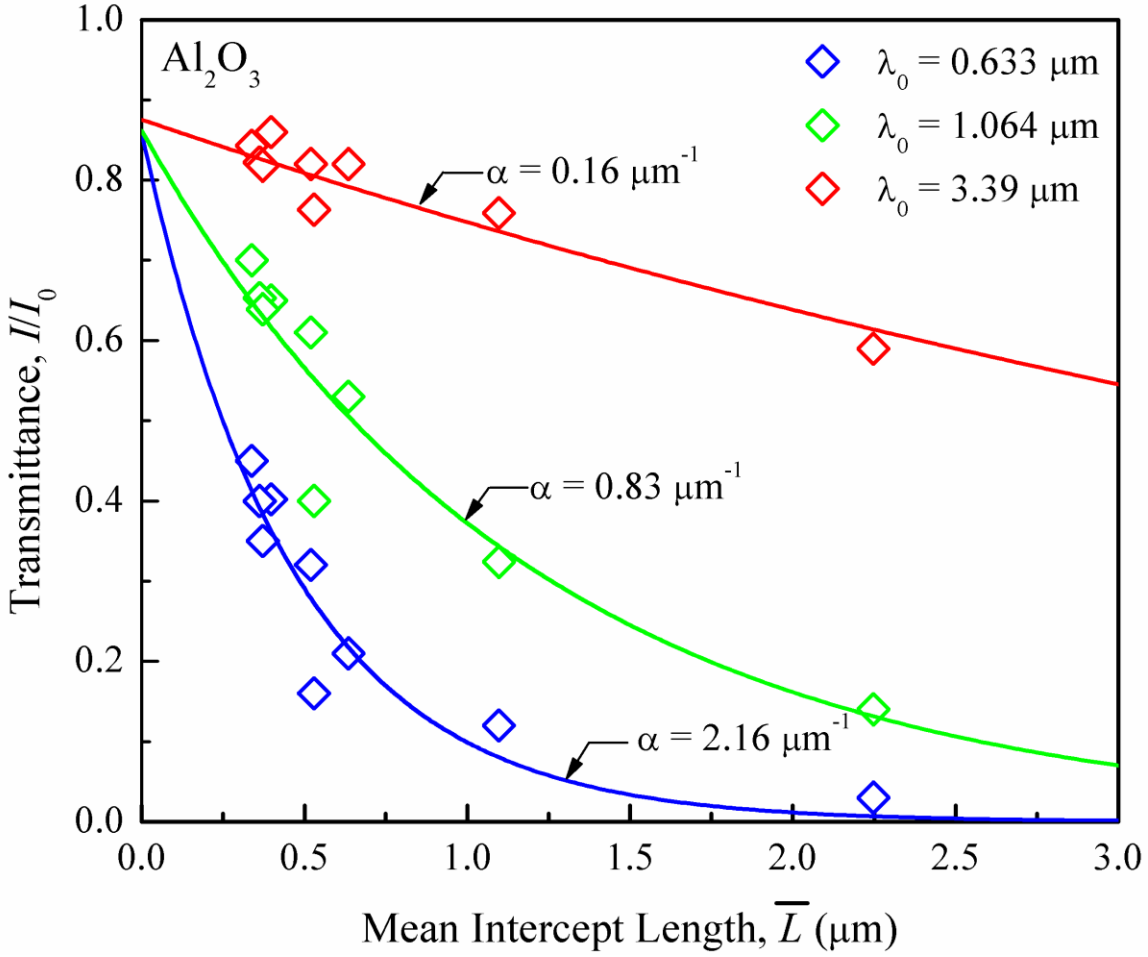

Figure 4.7 Variations of transmittance of polycrystalline Al_2O_3 with mean intercept length at three different wavelengths.

4.4.2 Effect of Grain Size on Transmittance and Scattering Coefficient

Figure 4.7 shows plots of the transmittance (I/I_0) versus mean grain size, $\bar{L}$, for the three wavelengths, 0.633, 1.064 and 3.39 μm. The lines through the data points are the best fits of the following equation:

$$\frac{I}{I_0} = \left[\frac{(1-R)^2 e^{-\alpha\bar{L}}}{1-R^2 e^{-2\alpha\bar{L}}}\right] \tag{4.9}$$

In Eq. (4.9), α is a material-characteristic parameter which is dependent on wavelength and specimen thickness, but independent of the grain size. α is related to the scattering coefficient, γ, via the equation, $\alpha = \gamma t/\bar{L}$. It should be noted that this interdependence of α and γ requires that γ must scale linearly with intercept length. At each wavelength and for the specimen thickness, t = 1mm, α was estimated by nonlinear regression analysis.

In order to test the linear dependence of the scattering coefficient on the intercept length, the scattering coefficients were calculated directly from transmittance, T, using the following equation [23]:

$$\gamma = \frac{1}{t} ln\left[\frac{(1-R)^2}{2T} + \sqrt{R^2 + \frac{(1-R)^4}{4T^2}}\right] \tag{4.10}$$

Figure 4.8 shows the variations of the scattering coefficient of polycrystalline Al_2O_3 with mean intercept length at three different wavelengths. The linear plots confirmed the self-consistency of Figures 4.7 and 4.8.

4.4.3 Effect of Light Wavelength on Scattering Coefficient

The dependence of the scattering coefficient on the wavelength of light can give Rayleigh scattering regime, i.e., when the particles are much smaller than the wavelength,

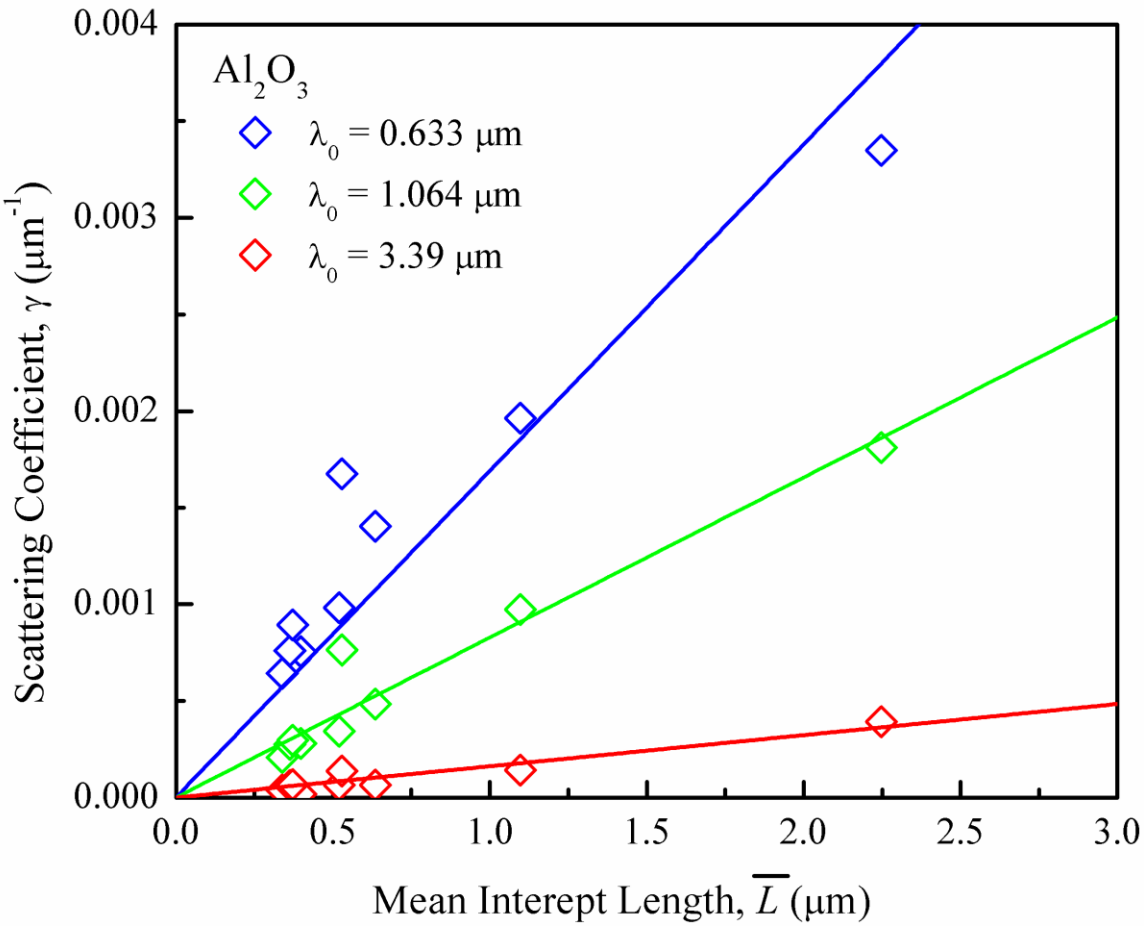

Figure 4.8 Variations of the scattering coefficient of polycrystalline Al_2O_3 with mean intercept length at three different wavelengths.

insight on the dominant light-scattering mechanism. Thus, for example, in the scatter coefficient is inversely proportional to the fourth power of the wavelength. Both the Raman and Viswanathan [18] and Kahan *et al.* [19, 20] models, however, predict scattering coefficients that are inversely proportional to the square of the wavelength, with a weak dependence of $\overline{\Delta n^2}$ on λ_0. To test this dependence, $[\alpha/(t\overline{\Delta n^2})] = [\gamma/(\bar{L}\overline{\Delta n^2})]$ was plotted as a function of λ_0 as shown in Figure 4.9. The line through the data points is a plot of the following equation:

$$\frac{\alpha}{t\overline{\Delta n^2}} = \frac{\gamma}{\bar{L}\overline{\Delta n^2}} = \frac{\Omega}{\lambda_0^2} \tag{4.11}$$

The good fit to the data in Figure 4.9 indicates that the measured scattering coefficient varies inversely with the square of the wavelength of light.

4.4.4 Scattering Profiles and Total Integrated Forward Scatter of Polycrystalline Al_2O_3

Figure 4.10 and Figure 4.11 show the scattering profiles of fine-grained ($\bar{G}$ = 0.62 and 1.0 μm) and coarse-grained ($\bar{G}$ = 25 μm) polycrystalline Al_2O_3 and of single crystal sapphire at wavelengths of 0.633 and 3.39 μm, respectively. In these figures, y-axis is the relative intensity which is calculated as the power density of the scattered beam divided by the power density of the incident beam. Specifically, the power density is the measured signal (watt) divided by the aperture area. The sharp peaks at small scattering angles indicate that the specimens have become partially transparent as shown in the subfigures of Figure 4.10 and Figure 4.11. The coarse-grained Al_2O_3 exhibited a flat curve at the wavelength of 0.633 μm because of light attenuation due to birefringence. The scattered intensity of the sapphire specimen was mainly contributed by specular reflection. At the

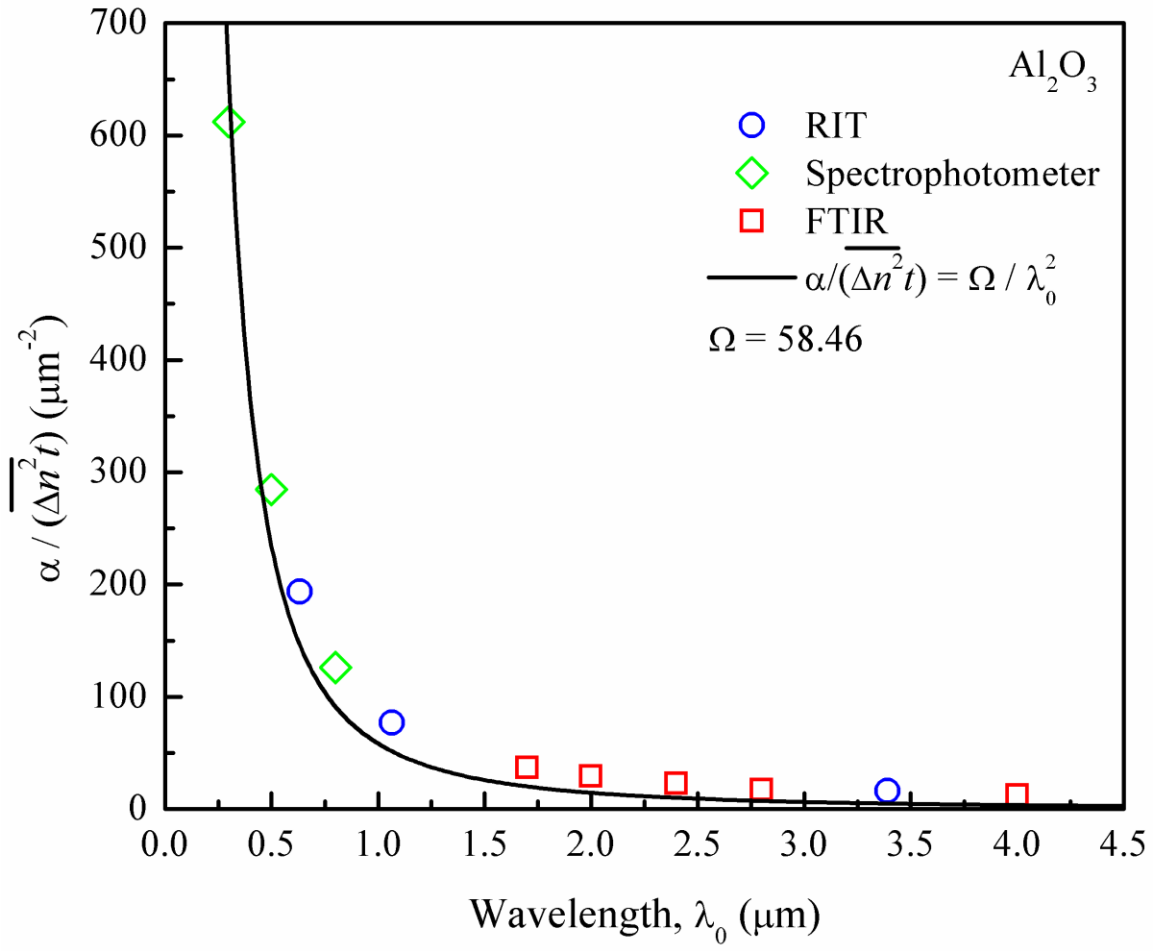

Figure 4.9 Variation of intercept length normalized scattering coefficient of polycrystalline Al_2O_3 with wavelength of light.

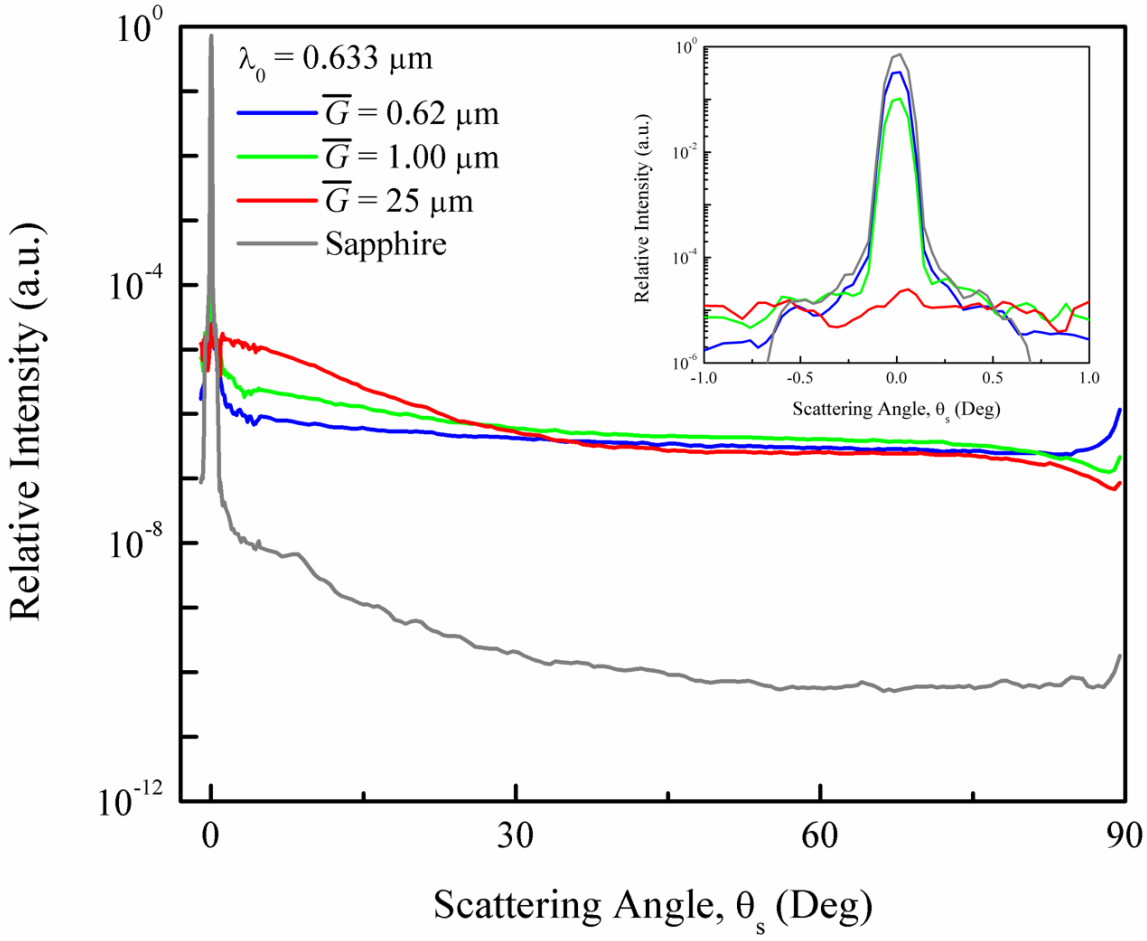

Figure 4.10 The scattering profiles at the wavelength of 0.633 μm for fine-grained, coarse-grained polycrystalline Al_2O_3 and sapphire.

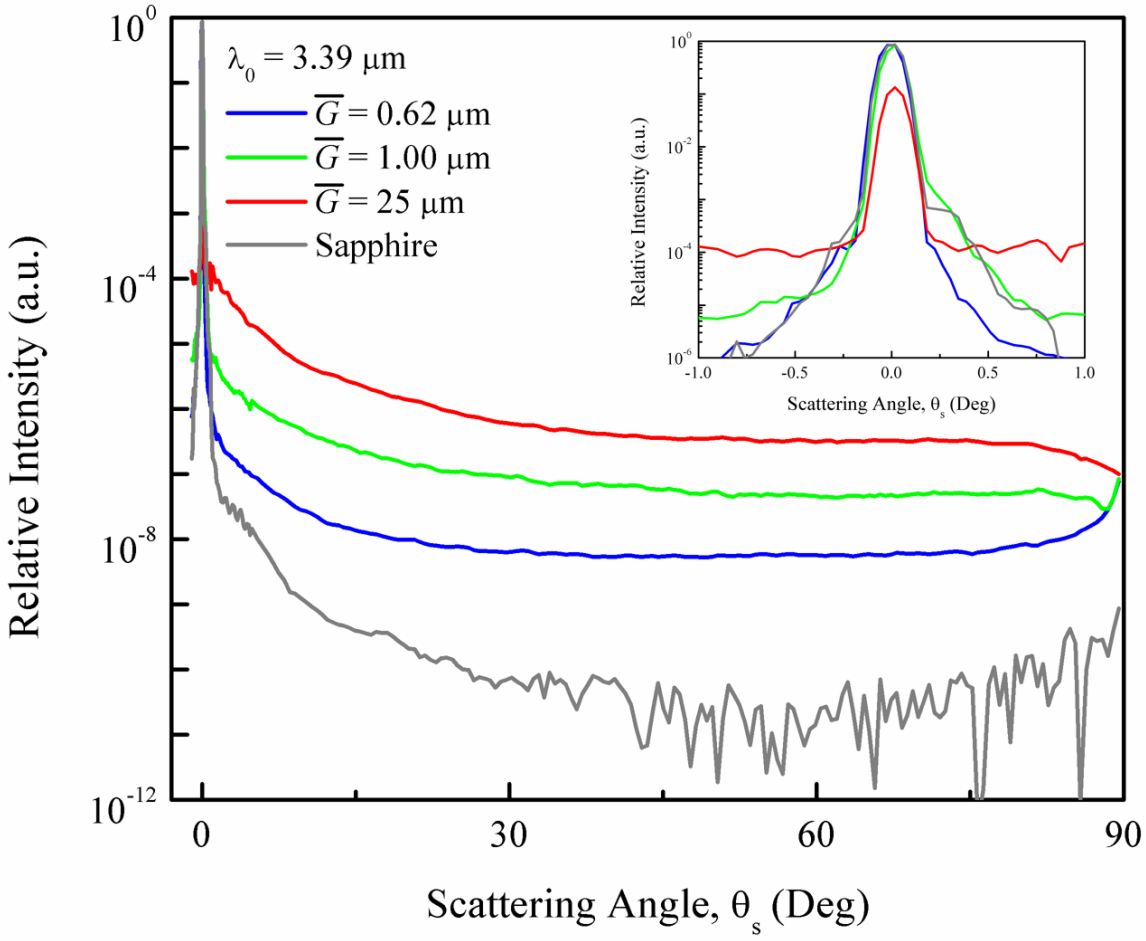

Figure 4.11 The scattering profiles at the wavelength of 3.39 μm for fine-grained, coarse-grained polycrystalline Al_2O_3 and sapphire.

wavelength of 0.633 μm, the scattered intensities were insensitive to grain size especially at the larger scattering angles ($\theta_s > 30°$). At the wavelength of 3.39 μm, the effect of grain size on the scattered intensity was more evident with the scattered intensity increasing as grain size increased. Table 4.2 lists the calculated values of forward scatter (S_F), total scatter (S_T), and backward scatter (S_B) at the wavelengths of 0.633 and 3.39 μm. The forward scatter was based on Eq. (4.7) and the total scatter was calculated using the following equation [23]:

$$S_T = 1 - T - A - R_T \tag{4.12}$$

In Eq. (4.12), T is the transmittance, A is the absorptance, R_T is the total reflectance which is expressed as $R_T = 2R/(1 + R)$, and R is the single-surface reflectance defined in Eq. (4.2). For polycrystalline Al_2O_3, the value of R_T is 0.141 and 0.125 for the wavelengths of 0.633 and 3.39 μm, respectively. Since no absorption peak was detected at these wavelengths, $A = 0$, and the sum of the transmittance, scatter, and reflectance must be unity [23]. The backward scatter, S_B, was calculated from $S_B = (S_T - S_F)$. Table 4.2 shows a trend of increasing scatter as the grain size increases in both the forward scatter and the total scatter.

4.5 Discussion

It is evident from the previous section that the scattering coefficient of polycrystalline Al_2O_3 scales linearly with the mean intercept length, $\bar{L}$, and inversely with the square of the wavelength of light, λ_0. These trends are consistent with both the theory of Raman and Viswanathan [18] and the theory of Kahan *et al.* [19, 20] and, therefore, these trends are not useful to discriminate the two theories. Therefore, the transmittance

Table 4.2 Forward scatter (S_F), total scatter (S_T) and backward scatter (S_B) of fine-grained Al_2O_3, Lucalox® and sapphire at wavelengths of 0.633 and 3.39 μm.

	PCA ($\bar{G}$=0.62 μm)	PCA ($\bar{G}$=1 μm)	Lucalox® ($\bar{G}$ = 25 μm)	Sapphire
S_F (λ_0 = 0.633 μm)	0.335	0.521	0.716	0.0007
S_T (λ_0 = 0.633 μm)	0.459	0.739	0.859	0.009
S_B (λ_0 = 0.633 μm)	0.124	0.218	0.143	0.0083
S_F (λ_0 = 3.39 μm)	0.005	0.056	0.574	0.0009
S_T (λ_0 = 3.39 μm)	0.025	0.058	0.730	0.005
S_B (λ_0 = 3.39 μm)	0.020	0.002	0.233	0.0041

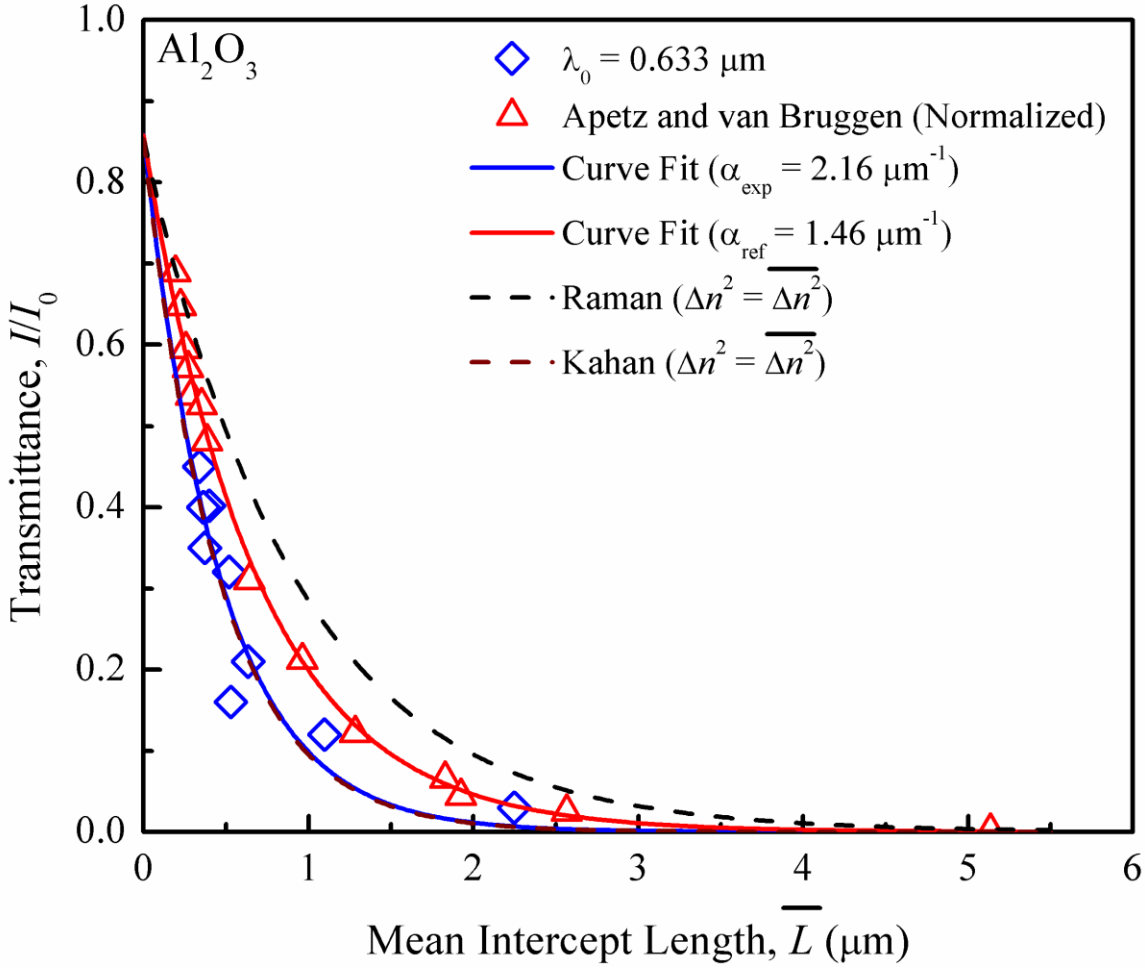

Figure 4.12 Transmittance of polycrystalline Al_2O_3 as a function of mean intercept length compared with theoretical predictions at the wavelength of 0.633 μm.

were quantitatively compared with theoretical predictions at the wavelength of 0.633 μm as shown in Figure 4.12. In the figure, the blue symbols are experimental data of the present study with t = 1 mm. The red symbols are data of Apetz and van Bruggen [5] corrected for the thickness using the following equation:

$$T_2 = T_1 exp[-\gamma(t_2 - t_1)] \tag{4.13}$$

In Eq. (4.13), T_1 is the transmittance measured with specimens of thickness t_1 = 0.8 mm, and T_2 is the transmittance calculated for the specimen thickness, t_2 = 1 mm. ϒ is the scattering coefficient calculated from the measured transmittance of T_1 for thickness t_1 at each grain size. The grain sizes reported by Apetz and van Bruggen [5] were divided by the geometric factor of 1.558, in order to present the data as intercept length. The blue and the red lines are the best fits of the following equation:

$$\frac{I}{I_0} = \left[\frac{0.8540e^{-\alpha\bar{L}}}{1 - 0.00576e^{-2\alpha\bar{L}}}\right] \tag{4.14}$$

The numerical factor, 0.8540, is $(1-R)^2$, where the single surface reflectance, R, is calculated using Eq. (4.2) and an average polycrystalline refractive index, $\bar{n}$ = 1.7605 for polycrystalline Al_2O_3 at λ_0 = 0.633 μm. The numerical factor, 0.00576, is the value of R^2. The present experimental data show lower transmittance than the measurements of Apetz and van Bruggen [5]. This is likely due to a higher residual porosity in the Al_2O_3 specimens of the current study. Thus, the curve fit of the experimental data showed a higher value of the material- characteristic parameter, α_{exp} = 2.16 μm^{-1} (blue line in Figure 4.12), compared with the reference data, α_{ref} = 1.46 μm^{-1} (red line in Figure 4.12).

Figure 4.13 shows the effect of the pore scattering on the optical transmittance of polycrystalline Al_2O_3. Assuming the data of Apetz and van Bruggen with no residual

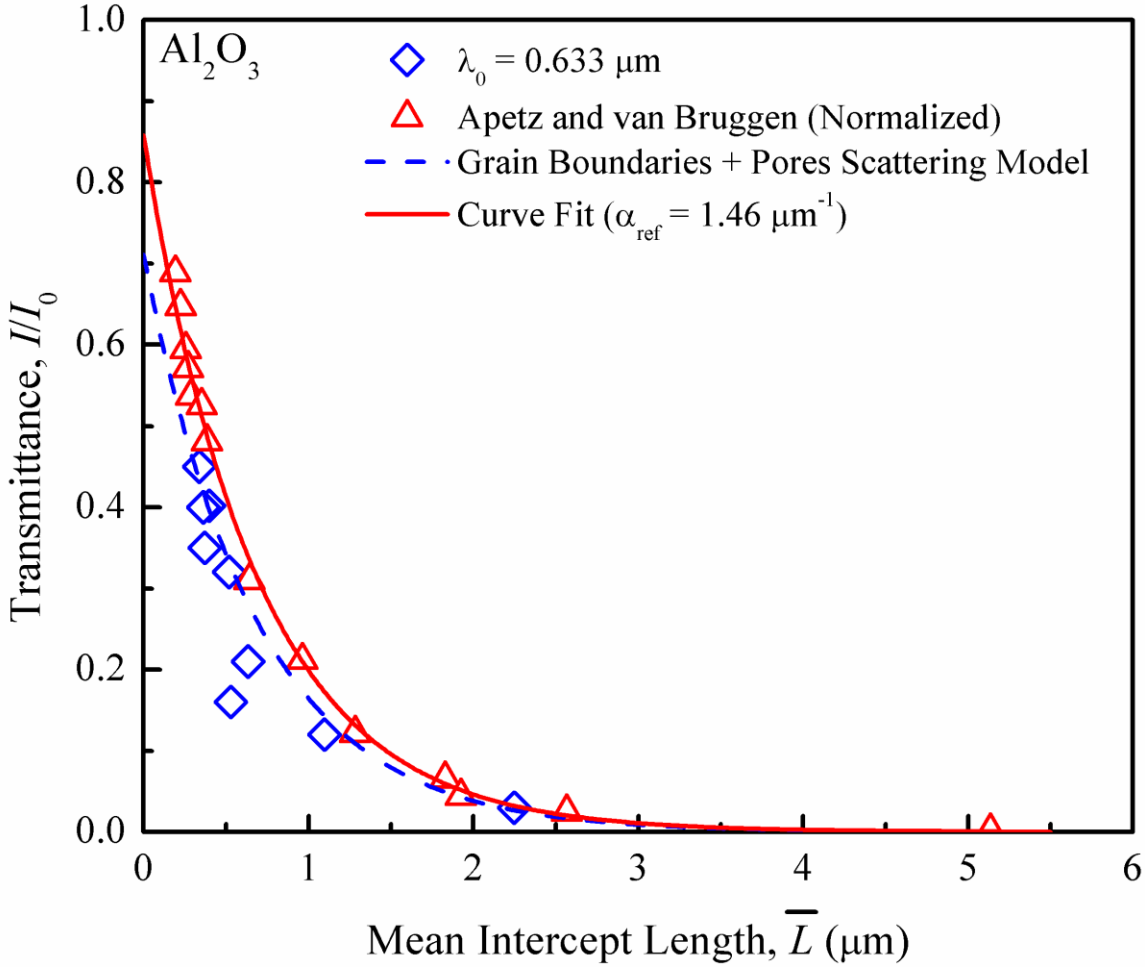

Figure 4.13 Effects of the pore scattering on the optical transmittance of polycrystalline Al_2O_3.

porosity, the transmittance influenced by the pores scattering can be calculated as $T_{Pore} = T_2 \exp(-\gamma_{pore} t)$ (dashed blue line in Figure 4.13). γ_{pore} is the scattering coefficient of the pore scattering and it can be expressed as:

$$\gamma_{pore} = \frac{3K\phi_{pore}}{2d_{pore}} \tag{4.15}$$

In Eq (4.15), K is the scattering efficiency for a specific pore size, using the software MicCalc® [32] (taking a value of 1 for the refractive index of pores and 1.7605 for the refractive index of the surrounding media). d_{pore} is the true pore diameter and it is the average section pore diameter measured from SEM micrographs times the geometrical factor 1.5708. The residual porosity, ϕ_{pore}, can be acquired by counting the number of pores (n) in a certain area (A) using the following equation [33]:

$$\phi_{pore} = \frac{n \cdot \frac{1}{6}\pi d_{pore}^3}{A d_{pore}} \tag{4.16}$$

By applying the Eq. (4.15) and Eq. (4.16), the scattering coefficient of pore scattering, γ_{pore}, is 1.88×10^{-4} μm^{-1}, using $K = 0.27124$, $\phi_{pore} = 0.0000726$ and $d_{pore} = 0.1571$ μm. Consequently a slightly lower transmittance in the dashed blue line is attributed to both grain boundaries and pore scattering.

As discussed in Chapter 2, Raman and Viswanathan [18] assumed a polycrystalline material to be made of uniform cube-shaped grains with the common edge length Δ. The cube edges are aligned along the three principal optical axes with the refractive indices of n_1, n_2 and n_3. One set of grain edge is parallel to the incident light. None of these assumptions are valid for polycrystalline Al_2O_3. If one applies their theory to polycrystalline Al_2O_3, a uniaxial crystal in the context of random orientation, the

probabilities of three principal optical axes are equal. Therefore, in Equation (4.5), $p_1 = p_2 = p_3 = 1/3$, and $n_1 = n_o$, and $n_2 = n_3 = n_e$. With these assumptions, we have

$\sum p_2 p_3 (n_2 - n_3)^2 = \frac{2}{9}(n_e - n_o)^2 = 0.00001422$. It is noted that this value is greater than the average value measured by EBSD ($\overline{\Delta n^2} = 0.00001112$) in Table 4.1.

In order to apply the theory of Raman and Viswanathan [18] to polycrystalline Al_2O_3, the following two modifications were made. First, the parameter, Δ, is defined as the mean path length of the light for a polycrystalline material. In the Raman and Viswanathan theory [18], the mean path length in a grain in combination with the refractive index with a particular crystal direction determines the light retardation of polycrystalline material. Thus, $\Delta = \bar{L}$. Second, $\overline{\Delta n^2}$ measured by EBSD represents an average value of $\sum_{i=1}^{N} p_i p_{i+1} (n_{i+1} - n_i)^2$ for Al_2O_3, and the *N* term sum should replace the three-term sum in Eq. (4.5). This approach gives $\alpha_{Raman} = 1.10\ \mu m^{-1}$ and corresponding prediction (dashed black line in Figure 4.12) is above both experimental and reference lines.

The theory of Kahan *et al.* [19, 20] is similar to Raman and Viswanathan [18] with respect to the effect of light retardation due to the combined effects of grain size and orientation. The assumption of the two-grain orientations in the Kahan *et al.* [19, 20] theory creates more restrictions in representing the random orientation of polycrystalline Al_2O_3. Therefore, it was assumed that $\overline{\Delta n^2}$ measured by EBSD can replace the term of $(p_1 p_2)(n_1 - n_2)^2$ in Equation (4.6). This approach gives $\alpha_{Kahan} = 2.19\ \mu m^{-1}$ (dashed brown line in Figure 4.12), and this value was almost identical to the best fit curve in the experimental data ($\alpha_{exp} = 2.16\ \mu m^{-1}$).

It is clear from the above discussion that it is difficult to discriminate between the

Raman and Viswanathan [18] and Kahan *et al.* [19, 20] theories by comparing the measured and the theoretical predictions of the variation in transmittance with the mean intercept length of a birefringent polycrystalline ceramic. Both theories make assumptions concerning the variations of the refractive index that were not applicable to uniaxial polycrystalline ceramics with randomly oriented grains. The approach of obtaining the $\overline{\Delta n^2}$ measured by EBSD in both theories provides the upper bound (dashed black line in Figure 4.12) and lower bound (dashed brown line in Figure 4.12) of the theoretical predictions at the wavelength of 0.633 μm. Moreover, Figure 4.14 and Figure 4.15 plotted the measured transmittance and theoretical predictions of Raman and Viswanathan and Kahan *et al.* at wavelength of 1.064 and 3.39 μm, respectively. It is noted that both theories overestimated the transmittance. Especially at the wavelength of 3.39 μm, the mean intercept length shows less impact on the transmittance. The transmittance loss at the higher wavelength is dominated by surface reflectance.

4.6 Conclusions

1. The sintered and hot isostatic pressed polycrystalline alumina shows the isotropic random orientation with an average grain orientation angle of 57.1°. No texture was detected as the temperature of sintering increased from 1200 to 1500°C.
2. The scattering coefficient of polycrystalline Al_2O_3 scales linearly with grain size and inversely with the square of the wavelength of light.
3. By obtaining the $\overline{\Delta n^2}$ measured from EBSD, the wave propagation in random media theories of the Raman and Viswanathan model gave the upper bound of the theoretical prediction and Kahan *et al.* model gave the lower bound of the theoretical prediction.
4. The forward scatter shows the scatter intensity increased as the grain size increased.

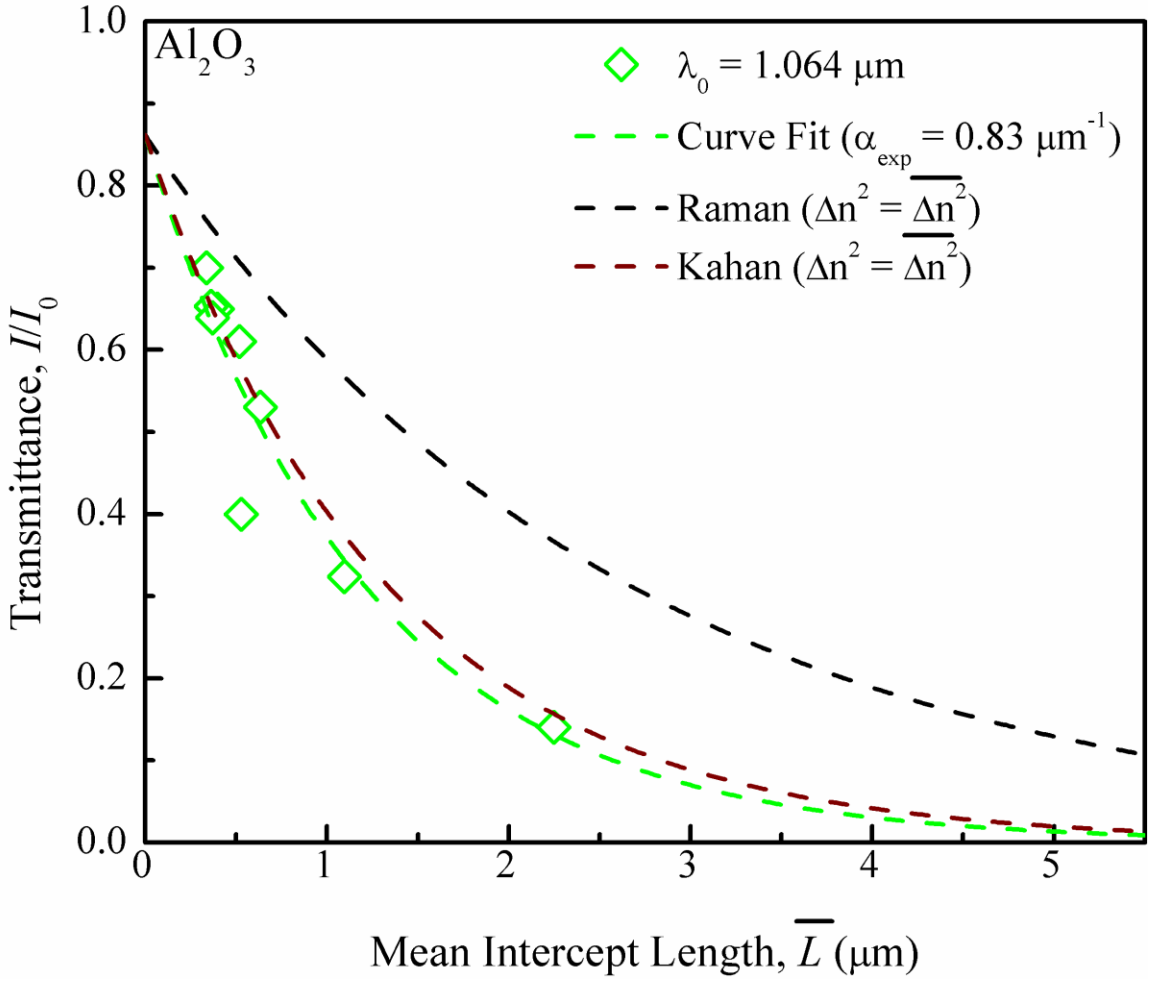

Figure 4.14 Transmittance of polycrystalline Al_2O_3 as a function of mean intercept length compared with theoretical predictions at the wavelength of 1.064 μm.

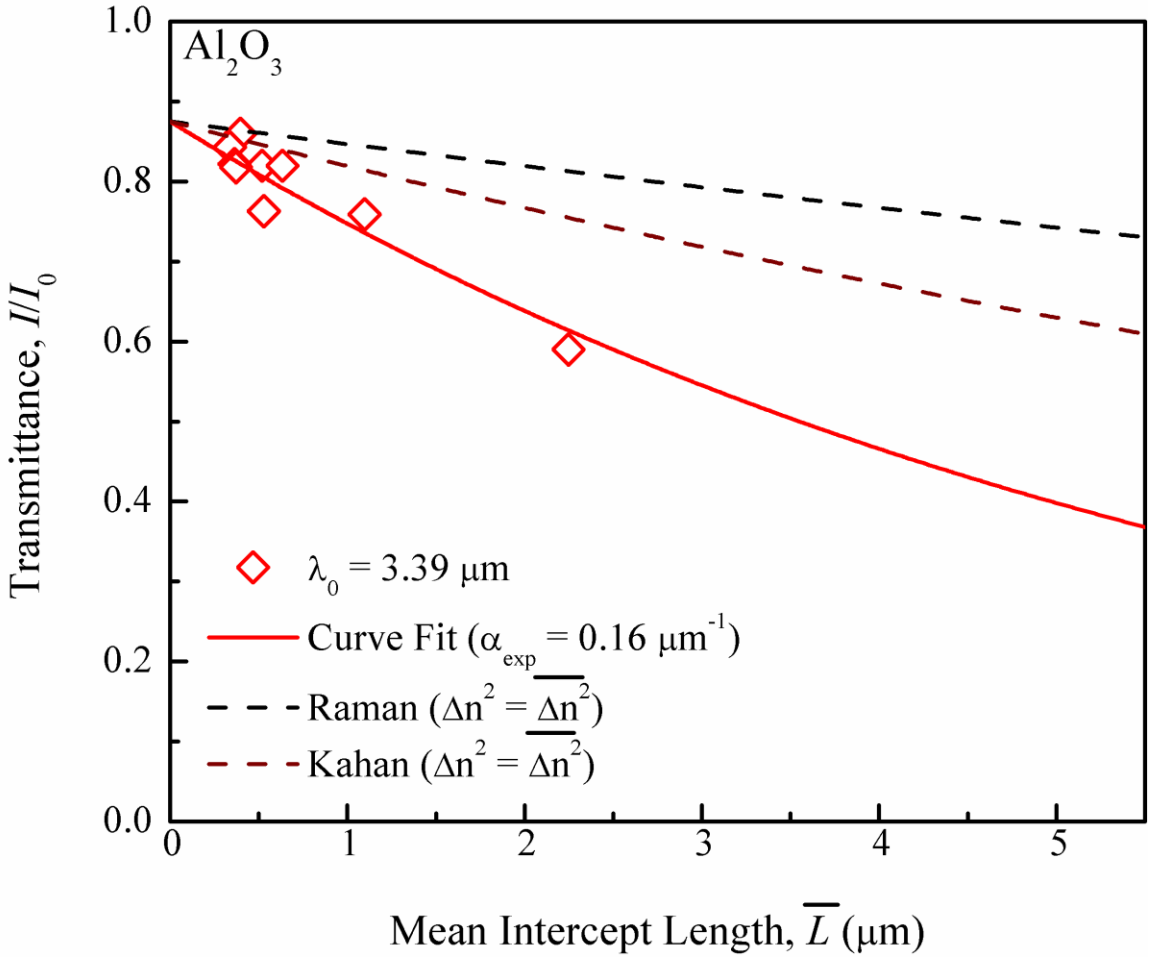

Figure 4.15 Transmittance of polycrystalline Al_2O_3 as a function of mean intercept length compared with theoretical predictions at the wavelength of 3.39 μm.

4.7 References

[1] E. Dorre and H. Hubner, *Alumina: Processing, Properties, and Applications*, Springer-Verlag, New York (1984).

[2] R. L. Coble, *Transparent alumina and method of preparation* U.S. Patent 3026210 (1962).

[3] J. E. Burke, "Lucalox Alumina: The Ceramic that Revolutionized Outdoor Lighting," *MRS Bull*., [June] 61-68 (1996).

[4] D. C. Harris, "A Peek Into the History of Sapphire Crystal Growth," pp. 1-11 in *Window and Dome Technologies VIII*, Vol. 5087. Edited by R. W. Tustison. SPIE: International Society for Optics and Photonics, Orlando, FL, 2003.

[5] R. Apetz and M. P. B. van Bruggen, "Transparent Alumina: A Light-Scattering Model," *J. Am. Ceram. Soc.*, **86** [3] 480-86 (2003).

[6] A. Krell, P. Blank, H. Ma, T. Hutzler, M. P. B. v. Bruggen and R. Apetz, "Transparent Sintered Corundum with High Hardness and Strength," *J. Am. Ceram. Soc*., **86** [1] 12–8 (2003).

[7] A. Krell, P. Blank, H. Ma, T. Hutzler and M. Nebelung, "Processing of High-Density Submicrometer Al_2O_3 for New Applications," *J. Am. Ceram. Soc*., **86** [4] 546-553 (2003).

[8] A. Krell and J. Klimke, "Effects of the Homogeneity of Particle Coordination on Solid-Sate Sintering of Transparent Alumina" *J. Am. Ceram. Soc*., **89** [6] 1985-1992 (2006).

[9] A. Krell, J. Klimke and T. Hutzler, "Advanced Spinel and Sub-μm Al_2O_3 for Transparent Armour Applications," *J. Eur. Ceram. Soc.*, **29** 275-81 (2009).

[10] G. Bernard-Granger and C. Guizard, "Influence of MgO or TiO_2 doping on the Sintering Path and on the Optical Properties of a Submicronic Alumina Material," *Scr. Mater*. **56** 983-986 (2007).

[11] G. Bernard-Granger, C. Guizard and A. Addad, "Infuence of Co-Doping on Sintering Path and on the Optical Properties of a Submicronic Alumina Material," *J. Am. Ceram. Soc*., **91** [5] 1703-1706 (2008).

[12] M. R. Pascucci and M. V. Parish, "Preparation and Properties of Nanograin Polycrystalline Alumina," pp. 55-66. in *Ceramic Nanomaterials and Nanotechnology III*, Vol. 55. Proceeding of the 106th Annual Meeting of The American Ceramic Society, Indianapolis, IN, 2005.

[13] M. V. Parish, M. R. Pascucci and W. H. Rhodes, “Aerodynamic IR Domes of Polycrystalline Alumina,” pp. 195-205 in *Window and Dome Technologies and Materials IX,* Vol. 5786. Window and Dome Technologies and Materials. Edited by R. W. Tustison. SPIE: International Society for Optics and Photonics, Orlando, FL, 2005.

[14] T. C. Wen and D. Shetty, “Colloidal Processing and Optical Transmittance of Submicron Polycrystalline Alumina,” pp. 80160C-1 – 80160C-7. in *Window and Dome Technologies and Materials XI,* Vol. 8016. Window and Dome Technologies and Materials. Edited by R. W. Tustison. SPIE: International Society for Optics and Photonics, Orlando, FL, 2011.

[15] W. H. Harrison, “Optical Model”; pp. 209-19 Section 3.0 in *Advanced Optical Ceramics*, Phase II, Annual Report, General Electric Company, ONR Contract N00014-78-C-0466, August 31, 1980.

[16] H. C. van de Hulst, *Light Scattering by Small Particles*. Dover Publications, Inc., New York, 1981.

[17] P. Debye and A. M. Bueche, “Scattering by an Inhomogeneous Solid,” *J. App. Phys.*, **20**, 518-525 (1949).

[18] C. V. Raman and K. S. Viswanathan, "The Theory of the Propagation of Light in Polycrystalline Media," *Proc. Indian Acad. Sci*. A, **41** 37-43 (1955).

[19] H. M. Kahan, D. P. Stubbs and R. V. Jones, "The Potentialities of Fine Grained Ceramics for Optical and Acoustical Applications," pp. 185-204. in *Optical and Acoustical Micro-Electronics*, Edited by J. Fox. Polytechnic Press, Brooklyn, NY, 19745.

[20] J. Schroeder and J. H. Rosolowski, "Light Scattering in Polycrystalline Materials," pp. 156-68. in *Emerging Optical Materials,* Vol. 297. Edited by S. Musikant. SPIE: International Society for Optics and Photonics, 1982.

[21] T. C. Wen and D. K. Shetty, “On the Effect of Birefringence on Light Transmission in Polycrystalline Magnesium Fluoride,” *J. Am. Ceram. Soc.*, **98** [3] 829-837 (2014).

[22] T. C. Wen and D. K. Shetty, “An Assessment of the Applicability of Particle Light Scattering Theories to Birefringent Polycrystalline Ceramics” *J. Am. Ceram. Soc.*, **99** [2] 551-556 (2016).

[23] D. C. Harris, *Materials for Infrared Windows and Domes: Properties and Performance*, SPIE Optical Enginneering Press, Bellingham, WA, 1999.

[24] A. Tsetsekou, C. Agrafiotis and A. Milias, “Optimization of the Rheological Properties of Alumina Slurries for Ceramic Processing Applications Part I: Slip-

casting," *J. Eur. Ceram. Soc.*, **21** 363-73 (2001).

[25] J. Cesarano III and I. A. Aksay, "Processing of Highly Concentrated Aqueous α-Suspensions Stabilized with Polyelectrolytes," *J. Am. Ceram. Soc*., **71** [12] 1062-67 (1988).

[26] ASTM C373-14a,"Standard Test Method for Water Absorption, Bulk Density, Apparent Porosity, and Apparent Specific Gravity of Fired Whiteware Products, Ceramic Tiles and Glass Tiles." ASTM International, 100 Bar Harbor Dr., PO Box C700, West Conshohocken, PA 19428-2959.

[27] F. J. Humphreys, "Review: Grain and Subgrain Characterization by Electron Backscatter Diffraction," *J. Mater. Sci.,* **36** 3833-54 (2001).

[28] B. L. Adams, S. I. Wright and K. Kunze, "Orientation Imaging: The Emergence of a New Microscopy," *Metall. Trans. A,* **24A** [4] 819-31 (1993).

[29] ASTM E1392, "Standard Patrice for Angle Resolved Optical Scatter Measurements on Specular or Diffuse Surfaces." ASTM International, 100 Bar Harbor Dr., PO Box C700, West Conshohocken, PA 19428-2959.

[30] J. C. Stover, *Optical Scattering: Measurement and Analysis.* McGraw-Hill, Inc., New York, 1990.

[31] M. I. Mendelson, "Average Grain Size in Polycrystalline Ceramics," *J. Am. Ceram. Soc.,* **52** [8] 443-46 (1969).

[32] B. Michel, MieCalc-Freely Configurable program for Light Scattering Calculations (Mie Theory), http://www.lightscattering.de/MieCalc/eindex.html, (accessed 13 May 2014).

[33] Y. Wang, T. Lu, L. Gong, J. Qi, J. Wen, J. Yu, L. Pan, Y. Yu and N. Wei, "Light Extinction by Pores in ALON Ceramic: The Transmission Properties," *J. Phys. D: Appl. Phys*. **43** 1-5 (2010).

CHAPTER 5

SUMMARY

This chapter summarizes light transmittance theories in birefringent polycrystalline ceramics, which have been discussed in Chapters 2 to 4.

5.1 The Light Transmittance Theories of Birefringent Polycrystalline Ceramics

In this study, two theoretical approaches were obtained to describe light transmittance through polycrystalline ceramics. The first approach proposed by Apetz and van Bruggen [1], treated birefringent polycrystalline ceramic material as a two-phase composite of isotropic spherical particles of diameter, d_p, and refractive index, n_p, dispersed in a homogenous matrix of refractive index, n_m. They employed an approximate form of the Raleigh-Gans-Debye (RGD) theory [2] of light scattering by spherical particles to formulate the scattering coefficient of a polycrystalline material. The second approach, characterized here as wave propagation in random media, was proposed by Debye and Bueche [3], and subsequently employed by Raman and Viswanathan [4] and Kahan *et al.* [5, 6]. Raman and Viswanathan [4] showed that grain orientation distribution and path length have the cumulative effect of causing light retardation in polycrystalline ceramics. Kahan *et al.* [5, 6] derived the scattering coefficient and Rayleigh ratio in terms of a two-point correlation function, one corresponding to pore scattering and the other to grain-boundary scattering.

Chapter 2 compared the measured transmittance of polycrystalline MgF_2 with the theoretical formulations of the scattering coefficient, Υ, based on the RGD theory and the wave propagation theory. The observed trends of the scattering coefficient with grain size and wavelength of light were consistent with both the RGD theory of particle light scattering and the Raman and Viswanathan theory of light retardation. The scattering coefficient of polycrystalline MgF_2 scales linearly with grain size and inversely with the square of the wavelength of light. However, the theoretical predictions of transmittance in birefringent ceramics are altered due to the uncertain values of material parameters in both theories. Specifically, transmittance predicted by the particle scattering model is strongly affected by grain-size distribution in addition to the average grain-size effect.

Chapter 3 designed a model of a two-phase system, involving silica microshperes dispersed in a glycerol and water solution. The model system was designed to simulate the birefringence of isotropic MgF_2. It was found that RGD theory showed the systematic deviation for higher particle volume fraction ($\phi > 0.2$) and larger particle size ($d_p > 1$ μm). This result suggested that light scattering models based on single particle scattering are unlikely to provide viable physical explanation for the effect of grain size on light transmittance in birefringent polycrystalline ceramics due to the high volume fraction in dense polycrystalline ceramics. In addition, Chapter 3 suggests that $\overline{d_\phi}$ is the pertinent particle size parameter when applying particle scattering theories to polydisperse systems rather than $\overline{d_N}$. This is relevant to polycrystalline optical ceramics, such as MgF_2 and Al_2O_3, because $\overline{d_\phi} = \beta \overline{d_N}$, where β is about 2.3 ± 0.33 for MgF_2 [1] and 2.4 ± 0.46 for Al_2O_3. The light transmittance of polycrystalline ceramics is often plotted as a function of

$\overline{d_N}$ instead of $\overline{d_\phi}$. This tends to bring the data closer to the predictions of the particle scattering models. The conclusion of Chapter 3 suggests that improved models based on wave propagation in random media, which take into account a distribution of grain sizes and orientations, are desirable for treating effects of birefringence on light attenuation in polycrystalline ceramics.

Chapter 4 investigated the applicability of the wave propagation theories of Raman and Viswanathan [9] and Kahan *et al.* [5, 6] to light transmittance in polycrystalline Al_2O_3. It showed that both Raman and Viswanathan [4] and Kahan *et al.* [5, 6] models could not represent the truly isotropic and random orientation of polycrystalline ceramics due to the restrictions of grain orientation on two or three optical axes. Chapter 4 indicated that the wave retardation theories of Raman and Viswanathan [4] and Kahan *et al.* [5, 6] provide the limit of upper and lower bounds for theoretical predictions of light transmittance as a function of mean intercept length.

Overall, it is appropriate to apply a model based on the theory of wave propagation in a random medium where the fluctuations of refractive index and their spatial variations are more representative of polycrystalline materials. There are two main barriers to light attenuation as a particle scattering theory. First, the volume fraction of the particles is too high for the single particle scattering theories in fully-dense ceramic. Second, the uncertainty of adopting either the number average diameter or volume weight average diameter in the polydisperse system could alter the theoretical predictions.

5.2 References

[1] R. Apetz and M. P. B. v. Bruggen, "Transparent Alumina: A Light-Scattering Model," *J. Am. Ceram. Soc*., **86** [3] 480-86 (2003).

[2] H. C. van de Hulst, *Light Scattering by Small Particles*. Dover Publications, Inc., New York, NY, 1981.

[3] P. Debye and A. M. Bueche, "Scattering by an Inhomogeneous Solid," *J. App. Phys*., 20, 518-525 (1949).

[4] C. V. Raman and K. S. Viswanathan, "The Theory of the Propagation of Light in Polycrystalline Media," *Proc. Indian Acad. Sci*. A, 41 37-43 (1955).

[5] H. M. Kahan, D. P. Stubbs and R. V. Jones, "The Potentialities of Fine Grained Ceramics for Optical and Acoustical Applications," pp. 185-203. in *Optical and Acoustical Micro-Electronics*, New York, NY, 1974.

[6] J. Schroeder and J. H. Rosolowski, "Light Scattering in Polycrystalline Materials," pp. 156-68. in *Emerging Optical Materials*, Vol. 297. Edited by S. Musikant. SPIE: International Society for Optics and Photonics, 1982.

CHAPTER 6

CONCLUSIONS

6.1 Conclusions

- Scattering coefficients for light attenuation in birefringent polycrystalline ceramics scale linearly with mean grain size and inversely with the square of the wavelength of light. These results are qualitatively consistent with two different theories: (a) an analytical approximation of Raleigh-Gans-Debye theory of light scattering by spherical particles, and (b) wave propagation in random media.
- The theoretical predictions of the transmittance in birefringent polycrystalline ceramics are subject to considerable uncertainty due to the uncertain values of the material parameters that appear in the theoretical equations.
- Transmittance predicted by particle-scattering models, in particular, is strongly affected by grain-size distribution in addition to the average grain-size effect.
- Measurements of light transmittance and calculations of scattering coefficients in a model silica-glycerol/water system, designed to simulate polycrystalline MgF_2, show systematic deviation from RGD theory for particle volume fraction, $\phi > 0.2$, and large particle size ($d_p > 1$ μm). This makes the application of particle scattering theories to light attenuation in birefringent polycrystalline ceramics tenuous.

- Improved models based on wave propagation in random media, which take into account a distribution of grain sizes and orientations, are desirable in treating effects of birefringence on light attenuation in polycrystalline ceramics.
- $\overline{d_{\phi}}$ is the pertinent particle size parameter when applying particle scattering theories to polydisperse systems rather than $\overline{d_{N}}$.
- The sintered and hot isostatic pressed polycrystalline alumina shows the isotropic random orientation with an average grain orientation angle of 57.1°. No texture was detected as the temperature of sintering increased from 1200 to 1500°C.
- By obtaining the $\overline{\Delta n^2}$ measured from EBSD, the wave propagation theories of the Raman and Viswanathan model gave the upper bound of the theoretical prediction and the Kahan *et al.* model gave the lower bound of the theoretical prediction.
- The forward scatter shows the scatter intensity increased as the grain size increased.

APPENDIX A

TOTAL TRANSMITTANCE ACCOUNTING FOR MULTIPLE SURFACE REFLECTIONS AND SCATTERING COEFFICIENT FOR A THICK CERAMIC WINDOW

In Figure A.1, t is the specimen thickness, n is the refractive index of the polycrystalline ceramics, I_0 is the intensity of the incident light and the refractive index of the air is 1. I_1, I_2 and I_3 are defined as following:

$$I_1 = I_0\chi = I_0\frac{4n}{(1+n)^2} \tag{A.1}$$

$$I_2 = I_1 e^{-\gamma t} = I_0\frac{4n}{(1+n)^2}e^{-\gamma t} \tag{A.2}$$

$$I_3 = I_2\chi = I_0\frac{(4n)^2}{(1+n)^4}e^{-\gamma t} \tag{A.3}$$

In Eq. (A.1),

$$\chi = 1 - R = \frac{4n}{(1+n)^2} \tag{A.4}$$

$$R = (\frac{1+n}{1-n})^2 \tag{A.5}$$

where R is the single surface reflectance. By taking into account multiple scattering, the total transmittance is defined as

$$T = \frac{I_T}{I_0} \tag{A.6}$$

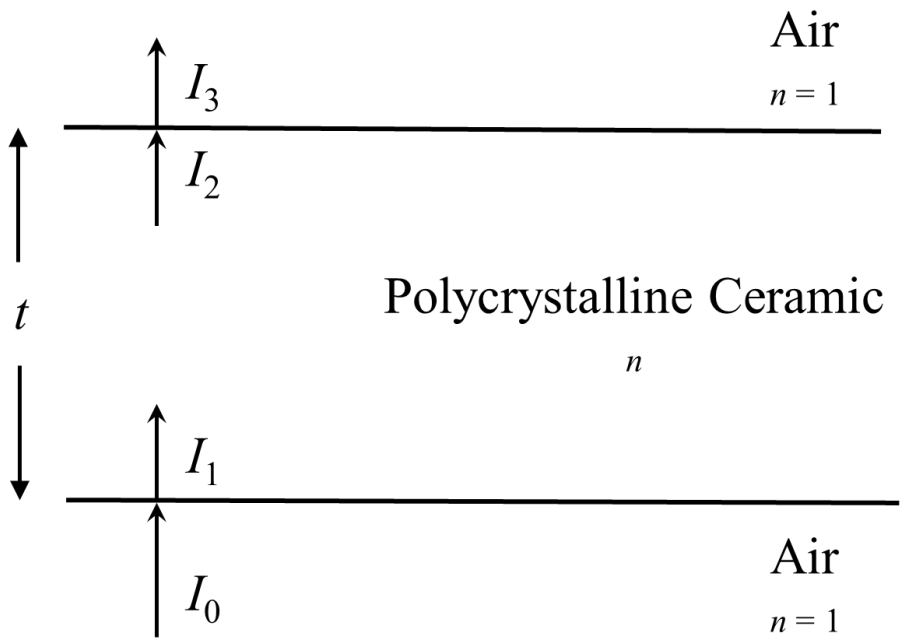

Figure A.1 Light transmitted through a thick polycrystalline ceramic window.

$$T = \frac{I_3}{I_0} + \frac{I_2}{I_0} R^2 e^{-2\gamma t} \chi + \frac{I_2}{I_0} R^2 e^{-2\gamma t} R^2 e^{-2\gamma t} \chi + \cdots \tag{A.7}$$

Substitute Eqs. (A.2) to (A.5) in Eq (A.7):

$$\begin{aligned} T = \frac{(4n)^2}{(1+n)^4} e^{-\gamma t} + \frac{(4n)^2}{(1+n)^4} \left(\frac{1+n}{1-n}\right)^4 e^{-3\gamma t} \\ + \frac{(4n)^2}{(1+n)^4} \left(\frac{1+n}{1-n}\right)^8 e^{-5\gamma t} + \cdots \end{aligned} \tag{A.8}$$

$$\begin{aligned} T = \frac{(4n)^2}{(1+n)^4} e^{-\gamma t} \left[1 + \left(\frac{1+n}{1-n}\right)^4 e^{-2\gamma t} + \left(\frac{1+n}{1-n}\right)^8 e^{-4\gamma t}\right] \\ + \cdots \end{aligned} \tag{A.9}$$

Let

$$\begin{aligned} \left[1 + \left(\frac{1+n}{1-n}\right)^4 e^{-2\gamma t} + \left(\frac{1+n}{1-n}\right)^8 e^{-4\gamma t} + \cdots\right] \\ = 1 + x + x^2 + \cdots \end{aligned} \tag{A.10}$$

where

$$x = \left(\frac{1+n}{1-n}\right)^4 e^{-2\gamma t} \ll 1 \tag{A.11}$$

$$1 + x + x^2 + \cdots = \frac{1}{1-x} = \frac{1}{1 - \left(\frac{1+n}{1-n}\right)^4 e^{-2\gamma t}} \tag{A.12}$$

Therefore,

$$T = \frac{\frac{(4n)^2}{(1+n)^4} e^{-\gamma t}}{1 - \left(\frac{1+n}{1-n}\right)^4 e^{-2\gamma t}} = \frac{(1-R)^2 e^{-\gamma t}}{1 - R^2 e^{-2\gamma t}} \tag{A.13}$$

Let $y = e^{-\gamma t}$, and Eq. (A.13) become

$$T = \frac{(1-R)^2 y}{1 - R^2 y^2} \tag{A.14}$$

$$T - TR^2y^2 = (1-R)^2y \tag{A.15}$$

$$TR^2y^2 + (1-R)^2y - T = 0 \tag{A.16}$$

$$y = \frac{-(1-R)^2 \pm \sqrt{(1-R)^4 + 4T^2R^2}}{2TR^2} \tag{A.17}$$

The correct root is one with a positive sign for the second term:

$$y = exp[-\gamma t] = \left[-\frac{(1-R)^2}{2TR^2} + \sqrt{\frac{(1-R)^4}{4T^2R^4} + \frac{1}{R^2}}\right] \tag{A.18}$$

Therefore,

$$\gamma = -\frac{1}{t} ln \left[-\frac{(1-R)^2}{2TR^2} + \sqrt{\frac{(1-R)^4}{4T^2R^4} + \frac{1}{R^2}}\right]$$

$$= -\frac{1}{t} ln \left[\frac{1}{R^2}\left(-\frac{(1-R)^2}{2T} + \sqrt{\frac{(1-R)^4}{4T^2} + R^2}\right)\right]$$

$$= \frac{1}{t} ln \left[\frac{R^2}{\left(-\frac{(1-R)^2}{2T} + \sqrt{\frac{(1-R)^4}{4T^2} + R^2}\right)}\right] \tag{A.19}$$

$$= \frac{1}{t} ln \left[\frac{R^2\left(\frac{(1-R)^2}{2T} + \sqrt{\frac{(1-R)^4}{4T^2} + R^2}\right)}{-\frac{(1-R)^4}{4T^2} + \frac{(1-R)^4}{4T^2} + R^2}\right]$$

$$= \frac{1}{t} ln \left[\frac{(1-R)^2}{2T} + \sqrt{\frac{(1-R)^4}{4T^2} + R^2}\right]$$

APPENDIX B

MEAN REFRACTIVE INDEX OF POLYCRYSTALLINE CERAMICS

Several parameters were measured and obtained in the theoretical calculation using the electron backscatter diffraction (EBSD), including the mean grain size ($\bar{G}$), grain size distribution, mean orientation angle ($\bar{\theta}$), and mean square deviations of refractive index ($\overline{\Delta n^2}$). This section compares the theoretical predictions and the measured values of the mean refractive index of polycrystalline MgF_2 and Al_2O_3.

Table B.1 shows theoretical and experimental predictions of the average refractive index in polycrystalline MgF_2 and Al_2O_3 at the wavelengths of 0.633, 1.064 and 3.39 μm [1, 2]. In Table B.1, $\overline{n_{EBSD}}$ is the mean refractive index calculated from the equation of index ellipsoid as following:

$$\overline{n_{EBSD}} = n(\bar{\theta}) = \frac{n_o n_e}{\sqrt{(n_e^2 cos^2\bar{\theta} + n_o^2 sin^2\bar{\theta})}} \quad \text{(B.1)}$$

where $\bar{\theta}$ is the mean orientation angles measured from the EBSD. The $\bar{\theta}$ values were 55.07° for the hot-pressed MgF_2 specimens, and 57.07° for the sintered and HIPed Al_2O_3 specimens. $\bar{n}$ is the mean refractive index for a polycrystalline material with isotropic randomly oriented grains, and it is an equation of index ellipsoid $n(\theta)$ times the density distribution of the orientation $f(\theta)$. For isotropic randomly oriented grains, $f(\theta)$ is the surface area of the strip in the hemisphere. In Figure B1, r is the radius of the hemisphere, θ is the orientation angle relative to y-axis, and the surface area of the strip is

Table B.1 Mean refractive index of the polycrystalline MgF_2 and Al_2O_3 at the wavelengths of 0.633, 1.064 and 3.39 μm.

Materials	$\lambda_0\ (\mu m)$	$\overline{n_{EBSD}}$	$\bar{n}$	n_{poly}
MgF_2	0.633	1.3849	1.3848	1.3809
	1.064	1.3813	1.3809	1.3771
	3.390	1.3633	1.3629	1.3595
Al_2O_3	0.633	1.7603	1.7605	1.7631
	1.064	1.7489	1.7492	1.7519
	3.390	1.6941	1.6943	1.6968

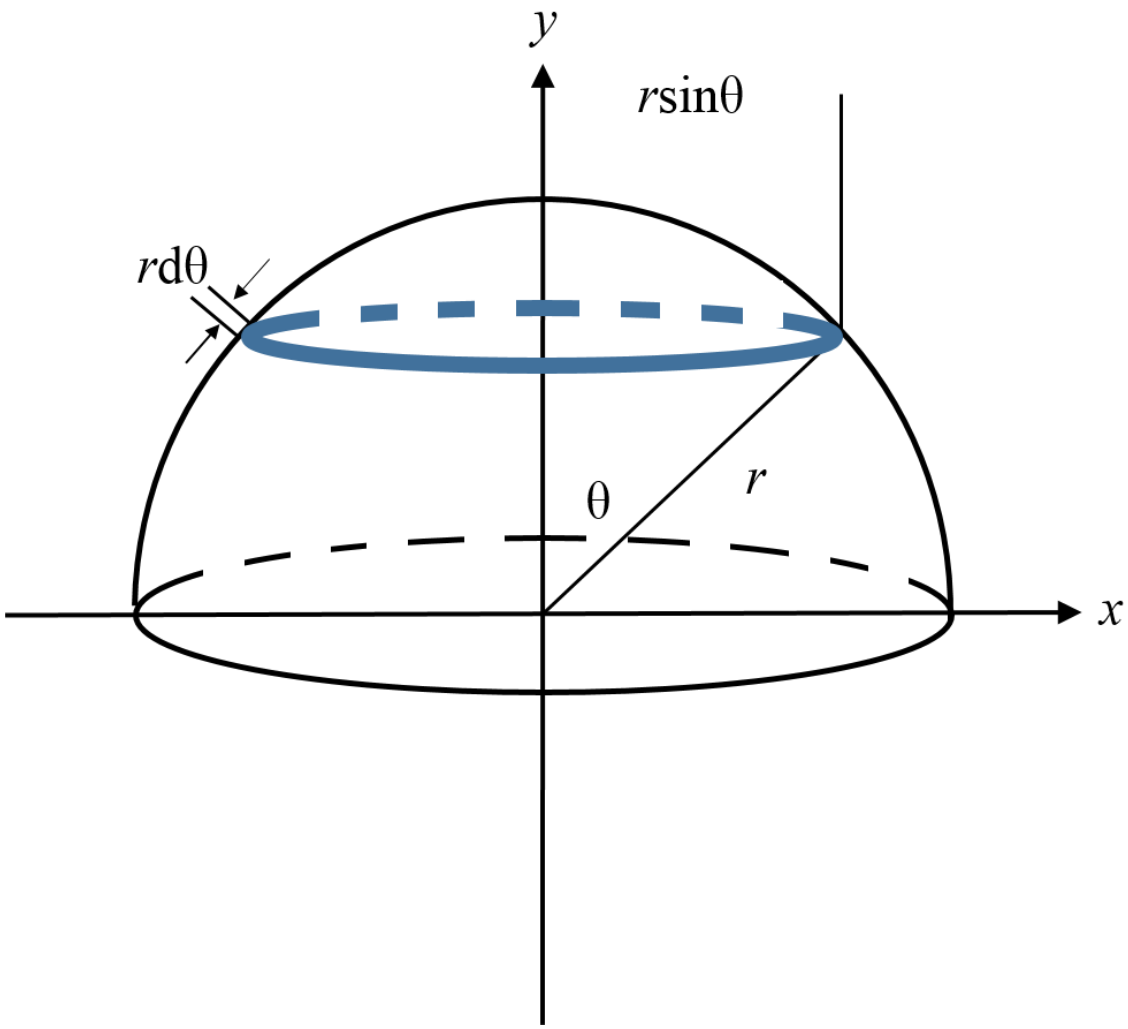

Figure B.1. Surface area of the strip in the hemisphere.

$2\pi r sin\theta \mathrm{r} d\theta$. Thus, $\bar{n}$ is expressed as:

$$\bar{n} = \frac{1}{2\pi r^2}\int_0^{\pi/2} n(\theta)\, 2\pi r^2 sin\theta d\theta = \int_0^{\pi/2} n(\theta) sin\theta d\theta \tag{B.2}$$

n_{poly} is the average refractive index of the polycrystalline ceramics, which is assumed the crystallographic axes in the single crystal grains composing the polycrystalline material [3]:

$$n_{poly} = \sqrt{\frac{2}{3}n_o^2 + \frac{1}{3}n_e^2} \tag{B.3}$$

Values of n_o and n_e were measured on single crystal MgF_2 and Al_2O_3 discussed in Section 1.2. It is clear that in Eq. (B.3), consideration of the probabilities of the principle optical axis are not good enough to represent the truly isotropic polycrystalline ceramics. Instead, Eq. (B.2) provides the better fit to the experimental data ($\overline{n_{EBSD}}$).

The conflict of the probability of the principle optical axis between Equation (B.3) and Section 2.5 is due to the different terminology and convention. In Equation (B.3), Thomas *et al.* [3] took the assumption of two n_o and one n_e within the uniaxial crystal. This research used the terminology from D. C. Harris's book, *Materials for Infrared Windows and Domes: Properties and Performance* [4]. Harris [4] defines the *c*-axis of sapphire crystal as the optical axis or the ordinary direction. The axis perpendicular to the *c*-axis is called the extraordinary direction. The corresponding refractive indices are designated n_o and n_e, respectively. When employing this convention for MgF_2 and Al_2O_3, there should be one component of n_o and two components of n_e.

Overall, EBSD provides an appreciable and pertinent method to measure the mean refractive index of the refractive index of polycrystalline ceramics. Especially, the measured $\overline{n_{EBSD}}$ shows good agreement with the calculated $\bar{n}$ in Table B.1.

B.1 References

[1] T. C. Wen and D. K. Shetty, "On the Effect of Birefringence on Light Transmission in Polycrystalline Magnesium Fluoride," *J. Am. Ceram. Soc*., **98** [3] 829-837 (2014).

[2] T. C. Wen and D. K. Shetty, "The Application of Wave Propagation in Random Media Theories in Polycrystalline Alumina" (to be submitted).

[3] M. E. Thomas, S. K. Anderson, T. M. Cotter and K. T. Constantikes, "Infrared Properties of Polycrystalline Magnesium Fluoride", *Infrared Phys. Techn*., **39** 213-222 (1998).

[4] D. C. Harris, *Materials for Infrared Windows and Domes: Properties and Performance.* SPIE Optical engineering press, Bellingham, WA, 1999.

APPENDIX C

THE RGD THEORY AND ITS LARGE PARTICLE SIZE APPROXIMATION

The intensity of light transmitted through a window of thickness, t, that partially scatters light in bulk and reflects at the two surfaces is given by the following equation [1]:

$$I(t) = I_0 \left[\frac{(1-R)^2 e^{-\gamma t}}{1 - R^2 e^{-2\gamma t}} \right] \tag{C.1}$$

where I_0 is the intensity of the incident light, R is the single surface reflectance, and γ is the scattering coefficient. For a window with surface and negligible absorption, the single surface reflectance is given by the following equation [1]:

$$R = \left(\frac{1-n}{1+n} \right)^2 \tag{C.2}$$

In Eq. (C.2), n is the refractive index of the window. The formulation of the scattering coefficient depends on the theoretical approaches used. For spherical particle with radius r, the scattering coefficient is

$$\gamma = N \pi r^2 K \tag{C.3}$$

In Eq. (C.3), K is the scattering efficiency and N is related to the volume fraction (ϕ), which is defined as

$$N = \phi / \frac{4}{3} \pi r^3 = \frac{6\phi}{\pi d_p^3} \tag{C.4}$$

In Eq. (C.4), d_p is the diameter of the spherical particle. By integrating the transmitted intensity over a large sphere and dividing the result by πr^2, H. C. van de Hulst

derived the efficiency *K* as [2]:

$$K = |m-1|^2 \Psi(x) \tag{C.5}$$

In Eq. (C.5), *m* is the relative refractive index, $= n_p/n_m$. n_p is the refractive index of the particle and n_m is the refractive index of the medium. *x* is the normalized particle size,

$$x = \frac{\pi d_p n_m}{\lambda_0} \tag{C.6}$$

The function $\Psi(x)$ was found by Rayleigh as [2]:

$$\begin{aligned}\Psi(x) = \frac{5}{2} + 2x^2 - \frac{\sin 4x}{4x} - \frac{7}{16x^2}(1-\cos 4x) \\ + \left(\frac{1}{2x^2} - 2\right)\{\zeta + log4x - Ci(4x)\}\end{aligned} \tag{C.7}$$

where ζ = Euler's constant (0.577) and *Ci* is the cosine integral defined as [2]

$$Ci(x) = -\int_x^\infty \frac{\cos u}{u} du \tag{C.8}$$

Table C.1 shows the calculations of the $Ci(4x)$ and $\Psi(x)$. From Eq. (C.2) to (C.6), the scattering coefficient of RGD theory is expressed as

$$\gamma = -\frac{3}{2}\phi \frac{\Delta n^2}{n_m^2}\frac{\Psi(x)}{d_p} \tag{C.9}$$

or in terms of the normalized particle size:

$$\gamma = -\frac{3\pi}{2}\phi \frac{\Delta n^2}{n_m}\frac{\Psi(x)}{x\lambda_0} \tag{C.10}$$

The RGD theory describes light scattering by spherical particle under the following conditions: (1) the refractive index of the particle is close to that of the medium, i.e., |m – 1| << 1. (2) the 'phase shift' is small, i.e., 2x|m – 1| << 1. And as a consequence of the above conditions, (3) the scattering efficiency is small, i.e., K << 1. In the regime defined

Table C.1 Table of normalized particle size (x), $Ci(4x)$ and $\Psi(x)$

x	$Ci(4x)$	$\Psi(x)$
0.3	0.420459	0.008495603
0.4	0.471733	0.028228512
0.6	0.317292	0.133421917
0.8	0.0552574	0.378756257
1	-0.140982	0.809316998
1.2	-0.197604	1.437476933
1.4	-0.128672	2.24525173
1.6	-0.00418141	3.201735895
1.8	0.0959571	4.285512989
2	0.122434	5.499777012
2.5	-0.0454564	9.309587438
3	-0.04978	14.48662216
3.5	0.0693964	20.7335248
4	-0.0142002	27.84200477
4.5	-0.0434751	36.09937654
5	0.0444198	45.45793548
5.5	0.00164069	55.69927543
6	-0.038333	66.99664687
6.5	0.0282952	79.3984629
7	0.0108695	92.71591043
7.5	-0.0330324	107.0395522
8	0.0163888	122.4603963
8.5	0.0162649	138.8273381
9	-0.0277409	156.1707908
9.5	0.00712976	174.6003802
10	0.01902	194.0015947
15	-0.00481324	443.1593597

by these conditions, a large particle size approximation of the scattering efficiency in the RGD theory is given by the following equation [2]:

$$K = 2(m-1)^2 x^2 \tag{C.11}$$

Therefore, the scattering coefficient for the RGD theory is expressed as

$$\gamma = \frac{3\pi^2 \phi d_p \Delta n^2}{\lambda_0^2} \tag{C.12}$$

or in terms of the normalized particle size:

$$\gamma = \frac{3\pi\phi\Delta n^2 x}{\lambda_0 n_m} \tag{C.13}$$

Figure C.1 compares the scattering coefficient of polycrystalline MgF_2 using Eq. (C.5) and Eq. (C.11) at the wavelength of 0.633 μm and the relative refractive index, m = 1.00362.

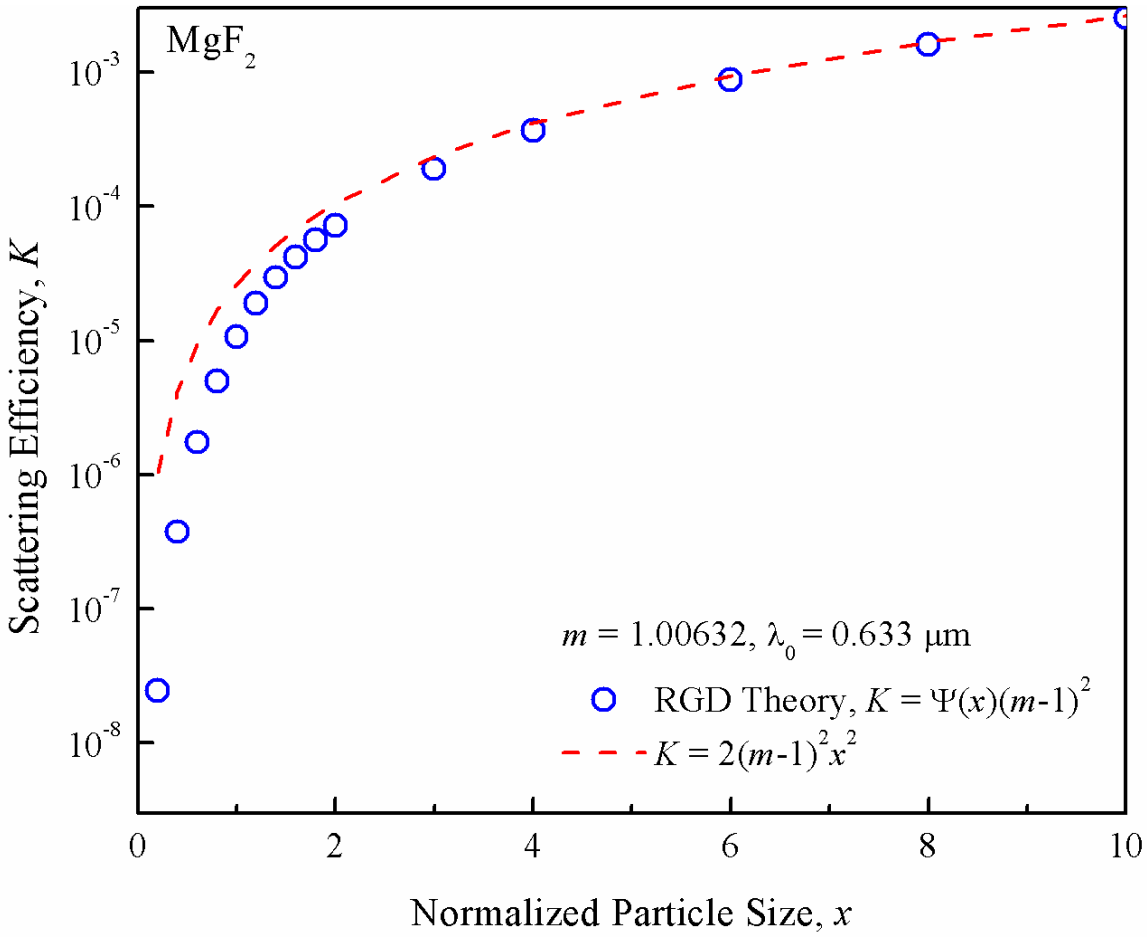

Figure C.1 Scattering coefficient of polycrystalline MgF_2 as function of normalized particle size.

C.1 References

[1] D. C. Harris, *Materials for Infrared Windows and Domes: Properties and Performance*. SPIE Optical engineering press, Bellingham, WA, 1999.

[2] H. C. van de Hulst, *Light Scattering by Small Particles*. Dover Publications, Inc., New York, NY, 1981.

APPENDIX D

LIGHT PROPAGATION IN RANDOM MEDIA: MODEL OF RAMAN AND VISWANATHAN

The optical wave before entry into a polycrystalline plate is represented by:

$$y = exp\left[\frac{2\pi i}{\lambda_0}(c\tau - Z)\right] \tag{D.1}$$

In Eq. (D.1), λ_0 is the wavelength of light in vacuum, c is the velocity, τ is the time and Z is the reference position. There are n grains or crystals through the thickness of plate in the direction of propagation of the light. We shall first consider a typical case in which the wave has pass through k_1 grains of refractive index μ_1, k_2 grains of refractive index μ_2 and k_3 grains of refractive index μ_3 before emerging from the plate. The numbers k_1, k_2 and k_3 can all vary from zero to n subject to the relation

$$k_1 + k_2 + k_3 = n \tag{D.2}$$

The optical path retardation of the emergent wave would be equal to $(k_1\mu_1 + k_2\mu_2 + k_3\mu_3)\Delta$, where Δ is the edge length of the cubic-shaped grain.

Now the number of ways in which k_1, k_2 and k_3 grain can be oriented along a row of n grains so as to have refractive indices μ_1, μ_2 and μ_3 is obviously $\frac{n!}{k_1!k_2!k_3!}$, and the probability of occurrence of each one of these cases is $p_1^{k_1}p_2^{k_2}p_3^{k_3}$. Hence the proportion of the total area of the area surface of the plate from which a wave represented by

$$e^{\frac{2\pi i}{\lambda_0}(c\tau - Z - [\overline{k_1\mu_1 + k_2\mu_2 + k_3\mu_3}]\Delta)} \tag{D.3}$$

The total probabilities are equal to the following:

$$\frac{n!}{k_1!\,k_2!\,k_3!} p_1^{k_1} p_2^{k_2} p_3^{k_3} \tag{D.4}$$

The emergent wave train can now be obtained by summation of waves of the Eq. (D.3) with their appropriate amplitudes and phases for all possible integral values of k_1, k_2 and k_3 satisfying the Eq. (D.2). The emergent wave is expressed as

$$y = P \sum_{k_1+k_2+k_3=n} \frac{n!}{k_1!\,k_2!\,k_3!} p_1^{k_1} p_2^{k_2} p_3^{k_3} e^{\frac{2\pi i}{\lambda_0}(c\tau - Z - [\overline{k_1\mu_1 + k_2\mu_2 + k_3\mu_3}]\Delta)} \tag{D.5}$$

where *P* is a factor which is introduced to take into account the loss in intensity of the light due to reflections at the intercrystallines boundaries. Equation (D.5) can be rewritten in the following way:

$$y = P e^{\frac{2\pi i}{\lambda_0}(c\tau - Z)} \sum_{k_1+k_2+k_3=n} \frac{n!}{k_1!\,k_2!\,k_3!} p_1^{k_1} p_2^{k_2} p_3^{k_3} \left(p_1^{k_1} e \frac{-2\pi i \Delta k_1 \mu_1}{\lambda_0}\right) \left(p_2^{k_2} e \frac{-2\pi i \Delta k_2 \mu_2}{\lambda_0}\right) \left(p_3^{k_3} e \frac{-2\pi i \Delta k_3 \mu_3}{\lambda_0}\right) \tag{D.6}$$

$$y = P e^{\frac{2\pi i}{\lambda_0}(c\tau - Z)} \sum_{k_1+k_2+k_3=n} \frac{n!}{k_1!\,k_2!\,k_3!} p_1^{k_1} p_2^{k_2} p_3^{k_3} \left(p_1^{k_1} e \frac{-2\pi i \Delta \mu_1}{\lambda_0}\right)^{k_1} \left(p_2^{k_2} e \frac{-2\pi i \Delta \mu_2}{\lambda_0}\right)^{k_2} \left(p_3^{k_3} e \frac{-2\pi i \Delta \mu_3}{\lambda_0}\right)^{k_3} \tag{D.7}$$

Now, a general multinomial series can be rewritten as

$$(a_1 + a_2 + \cdots + a_k)^n = \sum_{\substack{n_1, n_2 \cdots n_k \geq 0 \\ n_1 + n_2 + \cdots + n_k = n}} \frac{n!}{n_1!\, n_2! \cdots n_k!} a_1^{n_1} a_2^{n_2} \cdots a_k^{n_k} \tag{D.8}$$

Therefore, Eq. (D.7) can be written as

$$y = Pe^{\frac{2\pi i}{\lambda_0}(c\tau - Z)} \left(p_1 e^{\frac{-2\pi i \mu_1 \Delta}{\lambda_0}} + p_2 e^{\frac{-2\pi i \mu_2 \Delta}{\lambda_0}} + p_3 e^{\frac{-2\pi i \mu_3 \Delta}{\lambda_0}} \right)^n \tag{D.9}$$

The average refractive index of the medium is

$$\mu = (p_1 \mu_1 + p_2 \mu_2 + p_3 \mu_3) \tag{D.10}$$

If we set $\upsilon_1 = (\mu_2 - \mu_3)$, $\upsilon_2 = (\mu_3 - \mu_1)$ and $\upsilon_3 = (\mu_1 - \mu_2)$. We can express μ_1, μ_2 and μ_3 in terms of μ, p_1, p_2, p_3, υ_1, υ_2 and υ_3. From Eq. (D.10),we have

$$\begin{gathered} \mu = (1 - p_2 - p_3)\mu_1 + p_2 \mu_2 + p_3 \mu_3 \\ \therefore\ (1 - p_2 - p_3)\mu_1 = \mu - p_2 \mu_2 - p_3 \mu_3 \\ \therefore\ \mu_1 - p_2 \mu_1 - p_3 \mu_1 = \mu - p_2 \mu_2 - p_3 \mu_3 \\ \therefore\ \mu_1 = \mu + (p_2 \upsilon_3 - p_3 \upsilon_2) \end{gathered} \tag{D.11}$$

Similarly, we can write

$$\mu_2 = \mu + (p_3 \upsilon_1 - p_1 \upsilon_3) \tag{D.12}$$

$$\mu_3 = \mu + (p_1 \upsilon_2 - p_2 \upsilon_1) \tag{D.13}$$

The thickness of the plate is given by $t = n\Delta$. Hence substituting the Eqs. (D.11) to (D.13) in Eq. (D.9), we get

$$\begin{aligned} y = Pe^{\frac{2\pi i}{\lambda_0}(c\tau - Z)} \Bigg(& p_1 e^{\frac{-2\pi i \Delta (\mu + p_2 \upsilon_3 - p_3 \upsilon_2)}{\lambda_0}} + p_2 e^{\frac{-2\pi i \Delta (\mu + p_3 \upsilon_1 - p_1 \upsilon_3)}{\lambda_0}} \\ & + p_3 e^{\frac{-2\pi i \Delta (\mu + p_1 \upsilon_2 - p_2 \upsilon_1)}{\lambda_0}} \Bigg)^n \end{aligned} \tag{D.14}$$

$$y = Pe^{\frac{2\pi i}{\lambda_0}(c\tau - Z)}\left[p_1\left(e^{\frac{-2\pi i\Delta\mu}{\lambda_0}} \cdot e^{\frac{-2\pi i\Delta(p_2v_3 - p_3v_2)}{\lambda_0}}\right)\right.$$
$$+ p_2\left(e^{\frac{-2\pi i\Delta\mu}{\lambda_0}} \cdot e^{\frac{-2\pi i\Delta(p_3v_1 - p_1v_3)}{\lambda_0}}\right)$$
$$\left.+ p_3\left(e^{\frac{-2\pi i\Delta\mu}{\lambda_0}} \cdot e^{\frac{-2\pi i\Delta(p_1v_2 - p_2v_1)}{\lambda_0}}\right)\right]^n$$

The above equations can be simplified along the following lines.

$$y = Pe^{\frac{2\pi i}{\lambda_0}(c\tau - Z)}\left[\left(e^{\frac{-2\pi i\Delta\mu}{\lambda_0}}\right)^n\right.$$
$$\cdot\left(p_1 \cdot e^{\frac{-2\pi i\Delta(p_2v_3 - p_3v_2)}{\lambda_0}} + p_2 \cdot e^{\frac{-2\pi i\Delta(p_3v_1 - p_1v_3)}{\lambda_0}} + p_3\right.$$
$$\left.\left.\cdot e^{\frac{-2\pi i\Delta(p_1v_2 - p_2v_1)}{\lambda_0}}\right)^n\right]$$
$$= Pe^{\frac{2\pi i}{\lambda_0}(c\tau - Z - \mu t)}\left\{p_1\left[1 - \frac{2\pi i\Delta(p_2v_3 - p_3v_2)}{\lambda_0}\right.\right.$$
$$\left.+ \frac{1}{2!}\left(\frac{-2\pi i\Delta(p_2v_3 - p_3v_2)}{\lambda_0}\right)^2\right] \qquad \text{(D.15)}$$
$$+ p_2\left[1 - \frac{2\pi i\Delta(p_3v_1 - p_1v_3)}{\lambda_0}\right.$$
$$\left.+ \frac{1}{2!}\left(\frac{-2\pi i\Delta(p_3v_1 - p_1v_3)}{\lambda_0}\right)^2\right]$$
$$+ p_3\left[1 - \frac{2\pi i\Delta(p_1v_2 - p_2v_1)}{\lambda_0}\right.$$
$$\left.\left.+ \frac{1}{2!}\left(\frac{-2\pi i\Delta(p_1v_2 - p_2v_1)}{\lambda_0}\right)^2\right]\right\}^n$$

$$= Pe^{\frac{2\pi i}{\lambda_0}(c\tau - Z - \mu t)} \left\{ 1 \right.$$

$$- \frac{2\pi i \Delta (p_1 p_2 v_3 - p_1 p_3 v_2 + p_2 p_3 v_1 - p_2 p_1 v_3 + p_3 p_1 v_2 - p_3 p_2 v_1)}{\lambda_0}$$

$$\left. - \frac{2\pi^2 \Delta^2}{\lambda_0^2} \sum p_1 (p_2 v_3 - p_3 v_2)^2 \right\}^n$$

$$= Pe^{\frac{2\pi i}{\lambda_0}(ct - Z - \mu t)} \left\{ 1 - \frac{2\pi^2 \Delta^2}{\lambda_0^2} \sum p_1 (p_2 v_3 - p_3 v_2)^2 \right\}^n$$

Now,

$$\begin{aligned}
&\sum p_1 (p_2 v_3 - p_3 v_2)^2 \\
&\qquad = p_1 (p_2 v_3 - p_3 v_2)^2 \\
&\qquad + p_2 (p_3 v_1 - p_1 v_3)^2 + p_3 (p_1 v_2 - p_2 v_1)^2 \\
&= p_1 p_2^2 v_3^2 + p_1 p_3^2 v_2^2 + p_2 p_3^2 v_1^2 + p_2 p_1^2 v_3^2 + p_3 p_1^2 v_2^2 + p_3 p_2^2 v_1^2 \\
&\qquad - 2 p_1 p_2 v_3 p_3 v_2 - 2 p_2 p_3 v_1 p_1 v_3 - 2 p_3 p_1 v_2 p_2 v_1 \\
&= p_1 p_2 v_3^2 (p_2 + p_1) + p_1 p_3 v_2^2 (p_3 + p_1) + p_2 p_3 v_1^2 (p_3 + p_2) \\
&\qquad - 2 p_1 p_2 p_3 (v_3 v_2 + v_1 v_3 + v_2 v_1) \\
&= p_1 p_2 v_3^2 - p_1 p_2 p_3 v_3^2 + p_1 p_3 v_2^2 - p_1 p_2 p_3 v_2^2 + p_2 p_3 v_1^2 - p_1 p_2 p_3 v_1^2 \\
&\qquad - 2 p_1 p_2 p_3 (v_3 v_2 + v_1 v_3 + v_2 v_1) \\
&= p_1 p_2 v_3^2 + p_1 p_3 v_2^2 + p_2 p_3 v_1^2 \\
&\qquad - p_1 p_2 p_3 [(v_1^2 + v_2^2 + v_3^2) + 2(v_3 v_2 + v_1 v_3 + v_2 v_1)] \\
&= p_1 p_2 v_3^2 + p_1 p_3 v_2^2 + p_2 p_3 v_1^2 - p_1 p_2 p_3 [v_1 + v_2 + v_3]^2 \\
&\qquad = \sum p_1 p_2 v_3^2
\end{aligned} \tag{D.16}$$

Since,

$$\left(1-\frac{1}{n}F\right)^n \approx \left(1-\frac{1}{n}F\cdot n\right) = (1-F) \quad if\ F<1\ and\ n\ is\ large \tag{D.17}$$

$$1-y \approx e^{y} \qquad if\ y \ll 1 \tag{D.18}$$

$$[\exp(x)]^2 = \exp(2x) \tag{D.19}$$

∴

$$\begin{aligned} y &= e^{\frac{2\pi i}{\lambda_0}(c\tau - Z - \mu t)}\left\{1-\frac{2\pi^2\Delta^2}{\lambda_0^2}\sum p_1(p_2v_3-p_3v_2)^2\right\}^n \\ &= e^{\frac{2\pi i}{\lambda_0}(c\tau - Z - \mu t)}\left\{1-\frac{1}{n}\frac{2\pi^2\Delta t}{\lambda_0^2}\sum p_1p_2v_3^2\right\}^n \\ &= Pe^{\frac{2\pi i}{\lambda_0}(c\tau - Z - \mu t)}\left\{1-\frac{1}{n}\frac{2\pi^2\Delta t}{\lambda_0^2}\sum p_1p_2v_3^2\cdot n\right\} \\ &= Pe^{\frac{2\pi i}{\lambda_0}(c\tau - Z - \mu t)}\left\{1-\frac{2\pi^2\Delta t}{\lambda_0^2}\sum p_1p_2v_3^2\right\} \\ &= Pe^{\frac{2\pi i}{\lambda_0}(c\tau - Z - \mu t)}e^{\frac{-2\pi^2\Delta t}{\lambda_0^2}\sum p_1p_2v_3^2} \end{aligned} \tag{D.20}$$

The ratio of the intensity of the transmitted light and incident light is

$$\frac{I}{I_0} = P^2e^{\frac{-4\pi^2\Delta t}{\lambda_0^2}\sum p_1p_2(\mu_1-\mu_2)^2} \tag{D.21}$$

APPENDIX E

LIGHT PROPAGATION IN RANDOM MEDIA: MODEL OF KAHAN *et al.*

Kahan *et al.* [1, 2] assumed the grain to be oriented in only two orientations corresponding to the highest and the lowest refractive index of the crystal. They solved the scalar Helmohltz equation with two-point correlation function and derived the scattering coefficient for combined grain-boundary and pore scattering. The scattering coefficient for the Kahan *et al.* [1, 2] model is given by the following equation:

$$\Upsilon = \frac{k_o(\Delta n)^2(1-P_L)}{\langle n\rangle}\left\{\left(P_L G(2\langle n\rangle q P_L)\right) + b^2 G(2\langle n\rangle q)\right\} \tag{E.1}$$

where k_o is the propagation factor, Δn is the refractive index difference between the matrix and the voids, P_L is the linear porosity, $\langle n\rangle$ is the average refractive index of the matrix, q is a factor related to the intercept length, b is a factor related to the refractive index ratio, and each factor is expressed as follows:

$$k_o = \frac{\omega}{c} = \frac{2\pi f}{f\lambda_0} = \frac{2\pi}{\lambda_0} \tag{E.2}$$

$$\Delta n = p_1 n_1 + p_2 n_2 - 1 \tag{E.3}$$

$$\delta n = (p_1 p_2)^{1/2}(n_2 - n_1) \tag{E.4}$$

$$b = \frac{\delta n}{\Delta n} \tag{E.5}$$

$$G(x) = \frac{x^3}{1+x^2} \tag{E.6}$$

$$q = k_o(w_{12})^{-1} = \frac{2\pi}{\lambda_0(w_{12})} = \frac{2\pi\bar{G}}{(1.558)\lambda_0} \tag{E.7}$$

In Eq. (E.2), ω is the angular frequency, c is speed of light, f is frequency, λ_0 is wavelength of light. In Eq. (E.4), δn is the refractive index difference between the particles, p_1 and p_2 is the probability of the refractive index of n_1 and n_2, respectively. It is noticed that $G(x) = x$ when $x \gg 1$. In Eq (E.7), $(w_{12})^{-1}$ is the intercept length, $\bar{G}$ is the mean grain size. Combining the equations form (E.1) thorough (E.7) and with the assumption of the zero porosity ($P_L = 0$), scattering coefficient for grain-boundary scattering is shown as:

$$\gamma = \frac{k_o(\Delta n)^2}{\langle n \rangle}\{b^2 G(2\langle n \rangle q)\}$$

$$= \frac{2\pi(\Delta n)^2}{\lambda_0\langle n \rangle}\left\{\frac{(\delta n)^2}{(\Delta n)^2}2\langle n \rangle\left(\frac{2\pi\bar{G}}{(1.558)\lambda_0}\right)\right\} \tag{E.8}$$

$$= \frac{8\pi^2\bar{G}(p_1p_2)(n_1-n_2)^2}{\lambda_0^2(1.558)}$$

E.1 References

[1] H. M. Kahan, D. P. Stubbs and R. V. Jones, "The Potentialities of Fine Grained Ceramics for Optical and Acoustical Applications," pp. 185-203. in *Optical and Acoustical Micro-Electronics*, New York, NY, 1974.

[2] J. Schroeder and J. H. Rosolowski, "Light Scattering in Polycrystalline Materials," pp. 156-68. in *Emerging Optical Materials*, Vol. 297. Edited by S. Musikant. SPIE: International Society for Optics and Photonics, 1982.

.

APPENDIX F

CUMULATIVE DISTRIBUTION OF GRAIN ORIENTATIONS FOR RANDOMLY ORIENTED GRAINS

The angle θ is defined as the angle subtended by the *c*-axis of a grain with respect to a reference axis as shown in Figure F.1. For randomly oriented grains, the cumulative fraction of grains, $F(\theta)$, with orientation, θ, is defined by the ratio of the area of the spherical cap, $2\pi rh$, and the area of the hemisphere:

$$F(\theta) = \frac{2\pi rh}{2\pi r^2} = \frac{h}{r} \tag{F.1}$$

From the geometry of the spherical cap,

$$h = r - r\cos\theta \tag{F.2}$$

From Eq. (F.1) and (F.2), the cumulative fraction of grain is given as:

$$F(\theta) = 1 - \cos\theta \tag{F.3}$$

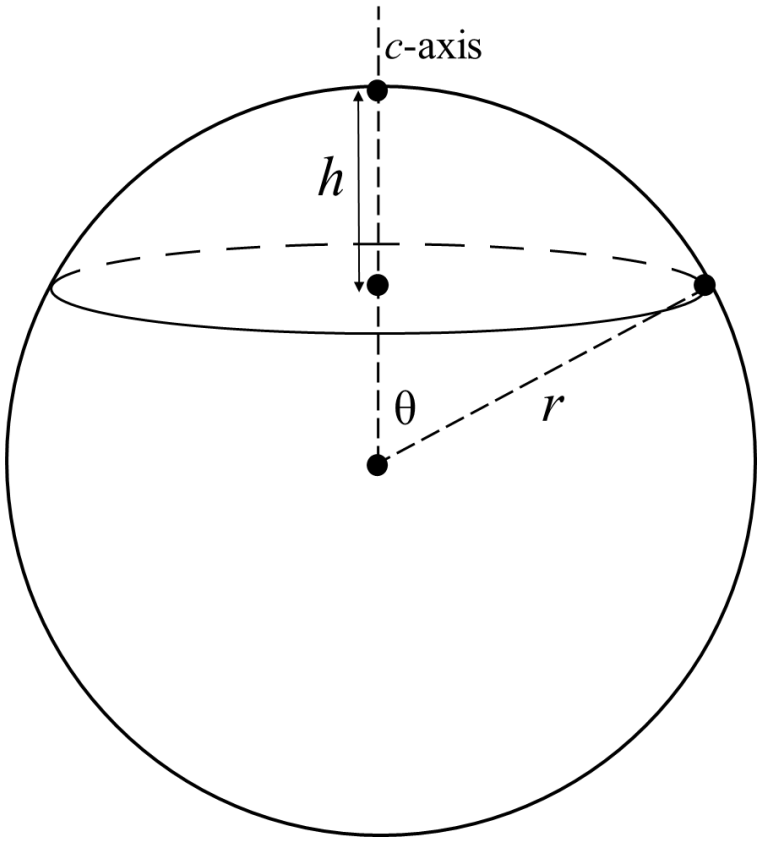

Figure F.1 The schematic of grain orientation with the orientation angle θ.

LIST OF PUBLICATIONS AND PRESENTATIONS

JOURNAL:

- N. Dasgupta, B. Butler, E. Sorge, **T. C. Wen**, D. K. Shetty, L. R. Cambrea, D. C. Harris, "Synthesis and Characterization of $Al_{2-x}Sc_x(WO4)_3$ Ceramics for Low-Expansion Infrared-Transparent Windows," *J. Mater. Sci*., **47**, 6286-6296 (2012).
- J. Koh, E. Sorge, **T. C. Wen** and D. K. Shetty, "Thermal Expansion Behaviors of Yttrium Tungstates in the WO_3-Y_2O_3 System," *Ceram. INT.*, **39** [7] 8421-8427 (2013).
- **T. C. Wen** and D. K. Shetty, "On the Effect of Birefringence on Light Transmission in Polycrystalline Magnesium Fluoride," *J. Am. Ceram. Soc*., **98** [3] 829-837 (2015).
- **T. C. Wen** and D. K. Shetty, "An Assessment of the Applicability of Particle Light Scattering Theories to Birefringent Polycrystalline Ceramics," *J. Am. Ceram. Soc*., **99** [2] 551-556 (2016)
- **T. C. Wen** and D. K. Shetty, "Light Transmission in Polycrystalline Alumina: Effects of Birefringence and Grain Size," (to be submitted).

PROCEEDING PAPER:

- **T. C. Wen** and D. K. Shetty, "Birefringence and Grain-Size Effects on Optical Transmittance of Polycrystalline Magnesium Fluoride," in Window and Dome Technologies and Materials XI, edited by Randal W. Tustison, Proc. of SPIE, Vol. 7302, pp. 73020Z-1-73020Z-6 (2009). Published, 2009.

- **T. C. Wen** and D. K. Shetty, "Colloidal Processing and Optical Transmittance of Submicron Polycrystalline Alumina," in Window and Dome Technologies and Materials XII, edited by Randall W. Tustison, Proceedings of SPIE, Vol. 8016, 80160C-1 – 80160C-6 (SPIE, Bellingham, WA, 2011).
- N. Dasgupta, B. Butler, E. Sorge, **T. C. Wen**, D. K. Shetty, "Synthesis, Characterization and Densification of $Al_{2-x}Sc_x(WO_4)_3$ Ceramics for Low-Expansion Infrared-Transparent Windows," in Window and Dome Technologies and Materials XII, edited by Randall W. Tustison, Proceedings of SPIE, Vol. 8016, 80160D-1 – 80160D-11 (SPIE, Bellingham, WA, 2011).

PRESENTATIONS:

- Birefringence and Grain-Size Effects on Optical Transmittance of Polycrystalline Magnesium Fluoride, Presented at the 11th SPIE Conference on Window and Dome Technologies and Materials Conference, Orlando, FL, April 16, 2009.
- Colloidal Processing and Optical Transmittance of Submicron Polycrystalline Alumina, Presented at the 12th SPIE Conference on Window and Dome Technologies and Materials Conference, Orlando, FL, April 27, 2011.